Shelf edge upwelling off northern Mozambique

Bernardino Sérgio Malauene

Mini-dissertation Presented for the Degree of

MASTER OF SCIENCE

(By coursework and dissertation)

in Applied Marine Science

Faculty of Science, Departments of Zoology and Oceanography

University of Cape Town

South Africa

April, 2010

Shelf edge upwelling off northern Mozambique

by

Bernardino Sérgio Malauene

MSc. mini-dissertation by coursework and dissertation

Supervisors:

Prof. Frank Shillington

Oceanography Department−University of Cape Town (UCT)

Ass. Prof. Coleen Moloney

Zoology Department and Marine Research Institute−UCT

Dr. Mike Roberts

Bayworld Centre for Research and Education Partnership

Marine and Coastal Management (MCM)

UNIVERSITY OF CAPE TOWN
IYUNIVESITHI YASEKAPA • UNIVERSITEIT VAN KAAPSTAD

Zoology Department

Cape Town, 14 April 2010

Declaration

1. I know that plagiarism is wrong. Plagiarism is using another's work and pretending that it ones own.

2. I have used the Harvard convention for citation and referencing. Each significant contribution to, and quotation in, this dissertation from the work (s), of other people has been attributed, and has cited and referenced.

3. This dissertation is my own work.

4. I have not allowed, and will not allow, anyone to copy my work with the intention of passing it off as his or her own work.

Bernardino Sérgio Malauene

Acknowledgments

A number of individuals and institutions have directly or indirectly supported me complete this Master, I kindly thank all. I thank all my friend and family, specially my parents for their love.

I am deeply grateful to my supervisors Prof. Frank Shillington, Prof. Coleen Moloney and Dr. Mike Roberts for their orientation in organizing the manuscript, grammar, proof reading and discussion of the results and also for sharing their knowledge and time during this dissertation.

I kindly thank Mr. Bjorn Backeberg for his excellent contributions and assistance in *matlab*. I also thank Mr. Edward Hill for helping with GIS. Many thanks for Mr. Christo Whittle for supplying remote sensed data. I thank ASCLME project and all the participants of the cruise survey in the Mozambique Channel in 2008 and in 2009 for the shipboard data. I also thank the NANSEN project for providing the research vessel Dr. Fridtjof Nansen.

I thank Dr. Isabelle Ansorge and Dr. Alberto Mavume for introducing me to the UCT and to the AMS MSc. Course. I also thank Dr. Almeida Guissamulo for supporting my application for this Master. Thanks are addressed to UCT, Marine Research Institute, Departments of Zoology and Oceanography and all the lecturers for providing this excellent MSc. Course and giving me opportunity to attend. Special thanks for Ms. Pavs Pillay for the collaboration during this Master. Many thanks for all my classmates for their collaboration during this Master.

Thanks go to the Director Domingos Gove and all staff at the National Institute of Fisheries Research and the Ministry of Fisheries, Mozambique, for allowing me to attend this Master.

Financial support was provided by the South African Research Chairs Initiative of the Department of Science and Technology and the National Research Foundation (NRF), the Applied Center for Climate and Earth Systems Science (ACCESS), and the African Coelacanth Ecosystem Programme (ACEP). I thank Prof. Astrid Jarre Dr. and Coleen Moloney, and Dr. Mike Robert for the nomination to these organizations that sponsored this Master and giving me the possibility to attend to the end. I also thank Tamaryn Morris and Gilly Smith for collaboration during this dissertation.

Abstract

A combination of satellite and *in situ* data were used to infer the occurrence and temporal-spatial variability of upwelling near Angoche. The data were derived from MODIS SST and Chl-*a* between 2003 and 2007, *in situ* moored underwater temperature recorder at a depth of 18 m for the period 2003−2007 and two shipboard surveys providing CTD and XBT data in December 2008 and in August 2009 in the northern Mozambique region. The results confirm that shelf edge upwelling occurs along the northern coast of Mozambique near Angoche between 15 and 18^{o}S, covering an area of approximately 68 000 km^2. The upwelling signature was not strong at the surface. Two upwelling core regions were identified: (1) the shelf core region and (2) the slope core region. At the shelf core region upwelling was more persistent than at the slope core upwelling. The upwelling displayed seasonal variation between persistent downwelling (warm water) between April−July and intermittent upwelling (cool water) events between August−March. Generally the upwelling lasted for a period of about two months but, shorter periods between 8 and 30 days were also observed. The driving mechanism for the shelf edge upwelling off northern Mozambique was determined from satellite observations (NOAA/NCDC) of blended sea surface wind data, and by multi-satellite (AVISO) altimeter sea surface anomaly data between 2003 and 2007 and also during the two cruise surveys in December 2008 and August 2009. These data showed upwelling is in part wind-driven in response to the north−easterly (NE) monsoon weak-wind velocities between August−March in the austral spring-summer. The intermittent nature of the upwelling season is also partly due to fluctuations in wind direction during the NE monsoon winds. Eddies appear to play a limited role in driving the upwelling.

Contents

Chapter 1

Introduction

The flow in the Mozambique Channel is dominated by eddies, the majority being anti-cyclonic in nature (Sætre and da Silva 1982, 1984; Biastoch and Krauss 1999; de Ruijter et al. 2002; Lutjeharms 2006). Eddies in the channel have spatial scales of approximately 300 to 350 km and about five to six anticyclones are found per year (Backeberg et al. 2008). They propagate southwards at approximately 3 to 6 km day^{-1} with currents reaching up to 2 m s^{-1} at their edges (Schouten et al. 2002, 2003). The average southward water volume transported by passage of eddies at 17^{o}S has been estimated at 14Sv (Ridderinkhof and de Ruijter 2003).

The continental shelf in the Mozambique Channel is generally narrow on its western side, but in certain areas, such as south of Angoche, it is somewhat wider (Figure 2.1). Together with the orientation of the coast, this allows for the formation of coastal cyclonic lee eddies off Angoche at about 16^{o}S. This feature was first described by Nehring et al. (1987), who suggested that its formation was driven by a continuous southward flowing "Mozambique Current". However, it has subsequently been shown that there is no continuous current in the Mozambique Channel. Rather it is believed that the Angoche lee edge eddy forms during the southward passage of strong anti-cyclonic eddies (Ridderinkhof and de Ruijter 2003; Lutjeharms 2006).

During the passage of an anti-cyclonic eddy in the region, strong poleward currents form along the coast south of Pemba. As the coast retracts westward near Angoche (Figure 2.1), the current overshoots (southward) forming a cyclonic lee eddy to the south of Angoche, in accordance with

the theory put forward by Gill and Schumann (1979).

It has been shown that the lee edge eddy can have a diameter of about 100 km and that deep water is upwelled in its core (Schemainda and Hagen 1983; Nehring et al. 1987). This feature is associated with enhanced chlorophyll-a concentrations (Nehring et al. 1987), which could be important for productivity and hence have implications for the fishing industry.

Angoche is an important area because it is located at the northern limit of the Sofala Bank, which is an important fishing ground of shallow water shrimps (family PENAEIDAE). The Sofala Bank is the principal source of shrimps for the Mozambican fisheries export market. The nearest fishing ground to Angoche, between Moma and Nicoadala, contributes more than 50% to the total catch each year (approximately 4034 tons amounting to 40 million USD in 2007) (de Sousa et al. 2008). This area seems to be the most productive on the bank which could be related to the production associated with the upwelling cell near Angoche.

Shelf edge upwelling off northern Mozambique has not been studied in any detail. It is not known whether the Angoche coastal lee eddy and its associated upwelling are persistent, nor what the driving mechanisms are. The objectives of this study are to understand the extent, frequency and the driving mechanisms of shelf edge upwelling off the northern Mozambique coast.

This dissertation has five chapters. Chapter 2 presents a description of the Mozambique Channel, the world's upwelling systems and mechanisms for coastal upwelling in particular. Regions with similar processes to those in the study area are also presented. In Chapter 3 the occurrence and spatial−temporal variability of the upwelling is investigated. The driving mechanisms of the upwelling and, in particular, the roles of winds and meandering currents are investigated in Chapter 4. An overall summary and conclusions of Chapter 3 and 4 is presented in Chapter 5.

This study addresses seven key questions:

1. Where does the shelf edge upwelling cell off northern Mozambique occurs? Where is its core?
2. What is the spatial extent of the shelf edge upwelling off northern Mozambique?
3. When do upwelling events occur off northern Mozambique? Is there a seasonal cycle?
4. How persistent is the shelf edge upwelling off northern Mozambique?
5. What are favourable wind conditions for upwelling in northern Mozambique? Are these related to the monsoon seasons?
6. Is the periodicity of upwelling events related to the passage of eddies?
7. Is upwelling in northern Mozambique always associated with a cyclonic eddy or can it occur independently?

Chapter 2

Literature review

2.1 General description of the Mozambique Channel

The Mozambique Channel is located between Madagascar and the African continent and between 11−27^{o}S. The coastline of Mozambique extends 2700 km in length and is oriented from north to south. The coast retracts westward near Angoche. The continental shelf in the northern region of Mozambique is shallow and narrow, and extends only a few kilometers offshore, hence the 200 m depth contour is found close to the coast (Figure 2.1). In contrast, the area south of Angoche along the central region of the Mozambican coast is characterized by a wide continental shelf (Johnesen et al. 2008) with the 200 m depth contour found much further offshore.

The climate of Mozambique is characterized by two main seasons−summer and winter. Summer is warm, humid and rainy between November and April, whereas winter is relatively cold and dry between May and October.

Only a few minor rivers exist off Angoche, contributing small amounts of freshwater runoff into the ocean. As shown by Sætre and da Silva (1982), the freshwater runoff is seasonal and most of the rivers contribute 60 to 90% of their annual runoff from January to April. Peak runoff occurs during February and March with the minimum in October. The closest major river to the Angoche region is the Zambezi river, which is located to the south. The freshwater plume

of the Zambezi river propagates northward towards Angoche (Nehama 2008). It is not known whether the Zambezi plume reaches the region off Angoche.

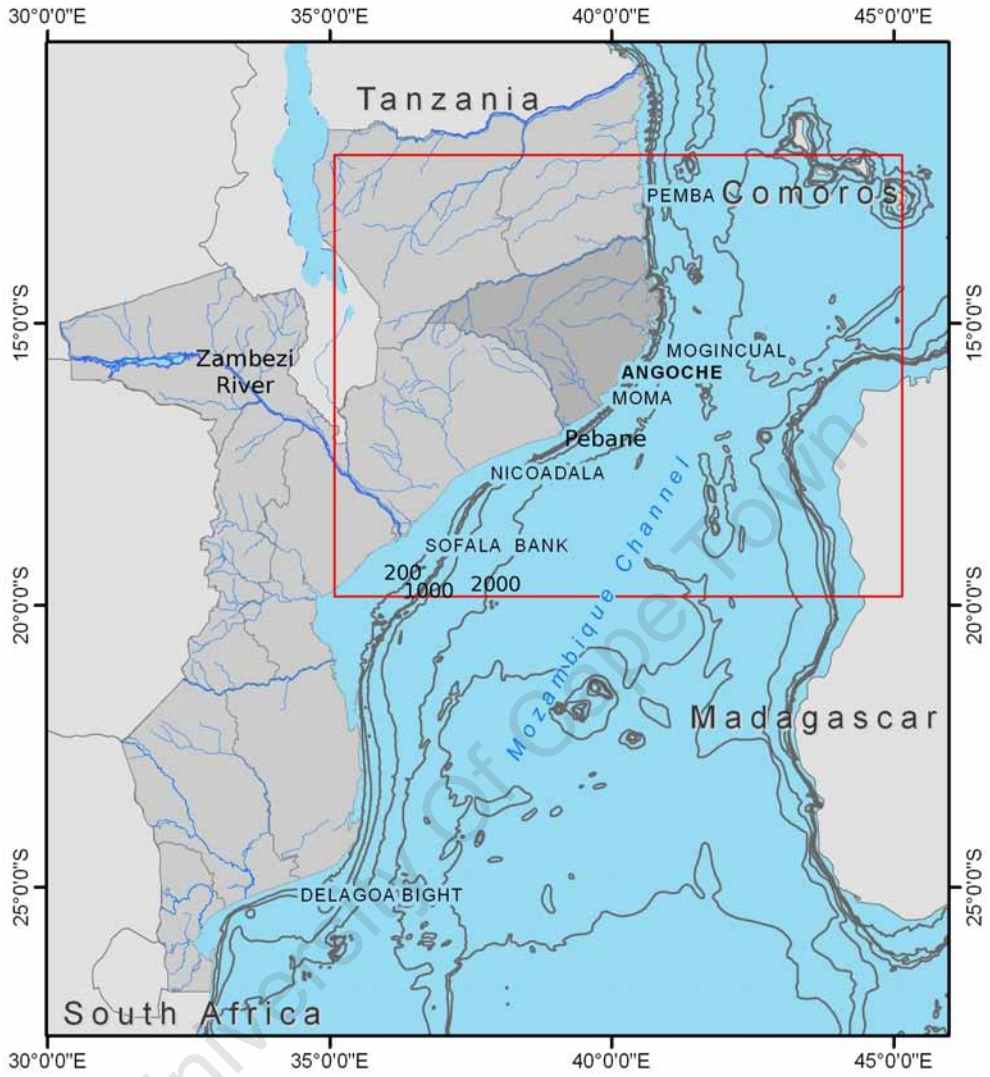

Figure 2.1: The Mozambique channel with the study area outlined by the red box. The continental shelf is narrow compared to the Sofala Bank.

The waters off Mozambique are characterized by two surface water masses (Sætre and da Silva 1982; Johnesen et al. 2008): Tropical (equatorial) and Sub-tropical Surface Water masses. North of 20^{o}S, off Angoche, the surface layer (the upper 100 m) is Tropical Surface Water, which consists of relatively homogenous and warm (27^{o}C) waters of equatorial origin. A sub-surface layer of Sub-tropical Water origin is evident by a strong thermocline and a salinity maximum between 100 and 200 m. Central Indian Ocean Water is found between 400 and 500 m. A layer of Intermediate Antartic Water is found at about 600 m. Red Sea Water containing low oxygen levels and high salinity is found between 800 to 1000 m.

Distribution of chlorophyll-*a*

Chlorophyll data are important because they give a first indication of biological production in the ocean. In the case of the Mozambique Channel surface chlorophyll-*a* (Chl-*a*) concentrations are relatively low, with an annual average of 0.3 mg m^{-3} (Omta et al. 2009). Chl-*a* concentration is usually higher on the shelf compared to offshore. The continental shelf in the southern region has more Chl-*a* than the northern region. Highest Chl-*a* levels in the Mozambican Channel are observed in the Pebane area, close to Angoche (Nehring et al. 1987). There is a seasonal cycle in the surface Chl-*a* concentration of the Mozambique Channel (Tew-Kai and Marsac 2009; Omta et al. 2009). The maximum Chl-*a* concentrations are observed in the austral winter and the minimum in the austral spring, with an amplitude of 0.1 mg m^{-3} (Omta et al. 2009). The seasonal cycle of Chl-*a* is strong in the northern (between 10−16^{o}S) and southern (24−30^{o}S) regions, and weak in the central (16−24^{o}S) region (Tew-Kai and Marsac 2009).

It is difficult to relate the results of Tew-Kai and Marsac (2009) and Omta et al. (2009) to the coastal area of Angoche for three reasons. First, Omta et al. (2009) calculated the area averaged Chl-*a* for the entire Mozambique Channel and analyzed the time series, not taking into account different variability in the vast area. Second, Tew-Kai and Marsac (2009) were interested in the deeper regions of the channel and masked the coastal areas where depths were less than 200 m. This excludes the coastal area off northern Mozambique. Finally the continental shelf area off Angoche lies between two of the large regions of Tew-Kai and Marsac (2009), the northern and central regions, separated at 16^{o}S. They observed that these two regions had different characteristics.

Wind regimes and monsoons

The Mozambican coast is influenced by two wind regimes: the south-east (SE) trade winds and the East Africa monsoon. The SE trade winds dominate at the coast of the southern and central regions of Mozambique with prevailing easterly winds all year round. The northern region of the Mozambique Channel is directly influenced by the southern extension of the East African monsoon. Sætre and da Silva (1982) observed that the monsoon wind along the

northern Mozambique coast does not extend south of 15^{o}S. They also showed that the monsoon exhibits seasonal variability with two distinct regimes: (1) the south-west monsoon is associated with strong winds during the austral winter from April to September, and (2) the north-east monsoon is characterized by a prevailing north-easterly wind regime during the austral summer from October to February. These observations were made during the period 1978, 1979 and 1980.

The diurnal variation in wind direction, in particular offshore winds (also known as land breezes) during the night and onshore (sea breezes) during the day time, are not important in the region influenced by the monsoon−winds (Sætre and da Silva 1982).

Currents in the Mozambique Channel

Sætre and da Silva (1982, 1984) suggested, and de Ruijter et al. (2002) subsequently confirmed, that flow in the Mozambique Channel is dominated by a train of intermittent eddies, the majority of which are anti-cyclonic, and propagate southwards. This challenged the traditional concept that a steady western boundary current exists in the Mozambique Channel.

Based on several hydrographic and bathythermograph surveys between 1977 and 1980, Sætre and da Silva (1982) showed that the circulation pattern along the whole Mozambican coast is characterized by three large anti-cyclonic cells and some smaller cyclonic features (Figure 2.2) which apparently changed their positions along the coast. During the austral summer, an anti-cyclonic feature (I) was found to exist in the northern part of the channel with another (II) located in the central region. Both were separated by a small cyclonic eddy (a) around 16−18^{o}S. During winter, these two features (I and II) were observed to combine and the cyclonic eddy vanished (Sætre and da Silva 1982). Sætre and da Silva (1984) and de Ruijter et al. (2002) also noted that eddies in the Mozambique Channel were deep, reaching the bottom of the channel.

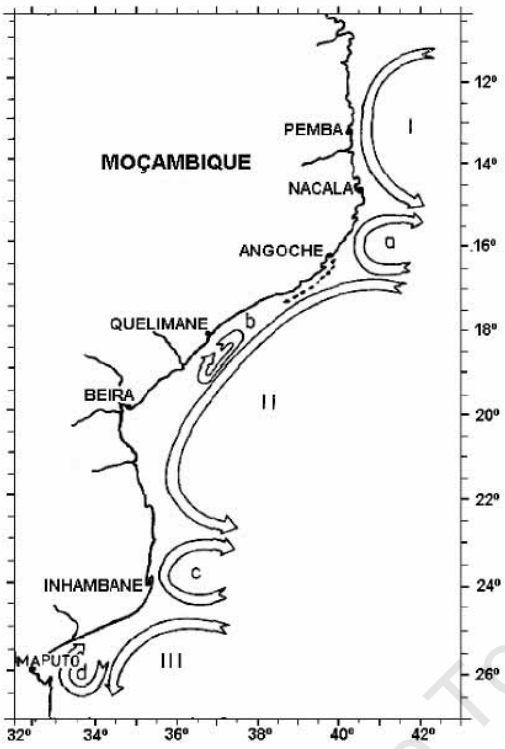

Figure 2.2: Dynamic features off the Mozambican coast during the austral summer showing anti-cyclonic eddies I, II and III and cyclonic eddies a, b, c and d (Sætre and da Silva 1982).

Based on 19 months (2000−2002) of current meter mooring data across the narrowest section ($\sim 16^o$S) of the Mozambique Channel, more recently Ridderinkhof and de Ruijter (2003) found that the current field is characterized by two distinct current regimes, one with a long period associated with strong current events, the other with shorter duration and weak currents. They found that anti-cyclonic eddies are formed regularly when the southward flow is associated with a strong current regime. No seasonal cycle was found. They also found a jet stream current associated with the passage of the strong anti-cyclonic eddies. They suggested that the retraction of the coastline around Angoche causes the southward jet current to become separated from the coast and induces a cyclonic lee eddy on the shelf of Angoche. Importantly Nehring et al. (1987) observed a cyclonic lee eddy in the same place ($\sim 16^o$S) during a survey in 1980.

de Ruijter et al. (2002), using hydrographic survey data, found a frequency of four anti-cyclonic eddies per year. Schouten et al. (2003), using satellite altimetry data, also found an average of four eddies per year. Ridderinkhof and de Ruijter (2003), analyzing long-term current meter

observations, found four to five strong current events per year. Quartly and Srokosz (2004), using satellite ocean colour (SeaWiFS) data, found a frequency of five to six eddies per year. Backeberg et al. (2008), using the Hybrid Coordinate Ocean Model (HYCOM) and altimeter data, suggested that eddies with spatial scales of approximately 300 to 350 km propagate southwards along the Mozambique Channel with a frequency of five to six times per year.

The volume transport through the Mozambique Channel has been shown to fluctuate over time. Ridderinkhof and de Ruijter (2003), based on an array of current meter moorings across the narrowest section of the Mozambique Channel at around 16^{o}S (Angoche area) during 2001 and 2002, observed volume transport values ranging between 20 Sv (1Sv =106 m^{3}s^{-1}) northwards and 40 Sv southwards (Figure 10 on Ridderinkhof and de Ruijter 2003). The average southward volume transport was estimated to be 14 Sv (Ridderinkhof and de Ruijter 2003). This result is similar to the average value of 15 Sv southward volume transport observed from a hydrographic survey by de Ruijter et al. (2002).

2.2 Upwelling systems in the world ocean

Upwelling regions in the world oceans can be divided into coastal (mainly eastern boundary currents) and open ocean systems, both characterized by divergence of the Ekman surface layer transport (McCreary et al. 1987; Anderson and Lucas 2008). Upwelling injects cold, deep water, rich in inorganic nutrients, into the surface layers of the ocean (Gill 1982; Duxbury and Duxbury 1997). In well-lit surface layers this results in some of the most productive marine ecosystems in the world, with elevated primary production supporting productive fisheries (Anderson and Lucas 2008).

Coastal upwelling zones have been estimated to be only 0.1% of the world ocean's surface area but they contribute about 50% of the fisheries yield (Cushing 1969 cited by Udarbe-Walker and Villanoy 2001). The major commercial fisheries associated with coastal upwelling systems include those for sardines, anchovies, and mackerel, all of which depend on abundant phytoplankton and zooplankton food resources (Anderson and Lucas 2008). The community structure in upwelling ecosystems is sensitive to environmental change, resulting in fluctuations

of fish numbers, which impact on both the higher and lower trophic levels (Anderson and Lucas 2008). For example, off the west coast of India, the maximum fish catches are obtained during or immediately after the upwelling season (Habeebrehman et al. 2008).

The major global coastal upwelling systems are located on the eastern boundaries of the ocean basins and include the California upwelling system off the west coast of North America, the Canary upwelling system off the west coast of North Africa, the Humboldt upwelling system off the west coast of South America and the Benguela upwelling system off the west coast of southern Africa (Patti et al. 2008). It is well known that these upwelling systems are driven by offshore surface Ekman transport induced by prevailing equatorward winds parallel to the coast. Upwelling manifests as a field of low sea surface temperature anomalies (Berger and Wefer 2002), coupled with high surface chlorophyll-a concentrations (Patti et al. 2008),

Differences exist in the upwelling intensity and spatial area among these four regions. Patti et al. (2008), in a recent study based on Chl-a concentrations derived from satellite observations, found that the upwelling intensity is dependent on the width of the continental shelf. Their study showed that the narrow shelf and poor water column stability of the California and Canary systems were the cause of reduced upwelling intensity. They also showed that the higher Chl-a concentrations found in the Benguela system relative to the Humboldt system are caused by the wider continental shelf off western South Africa. These upwelling systems all exhibit temporal fluctuations due to seasonal variations in wind stress. For example, coastal upwelling off the central, western coast of Portugal (extension of the Canary upwelling system) is only observed during the intensification phase of the persistent equatorward winds in summer (Oliveira et al. 2009).

General principles of upwelling

In order to understand coastal ocean dynamics such as upwelling, it is necessary to review the concepts of wind-driven circulation and Ekman transport. It is well known that wind blowing over the surface of the ocean causes the surface layer to move—known as the wind-driven circulation (Gill 1982; Pickard and Emery 1990; Duxbury and Duxbury 1997). The theory of

Ekman transport states that the wind-driven current in the upper layer (Ekman layer) tends to move perpendicular to the mean wind stress−to the left of the wind direction in the southern hemisphere (Gill 1982; Pickard and Emery 1990; Tomczak and Godfrey 1994; Duxbury and Duxbury 1997). This in turn sets up a pressure gradient in the upper water column. This gives rise to surface confined geostrophic currents in the direction of the wind.

Ekman divergence in open ocean areas occurs when two surface currents move in opposite directions, for example, one to the east and the other to the west. The Coriolis force causes them to diverge and as a consequence, deep nutrient rich water rises to replace the diverging waters (Gill 1982; Pickard and Emery 1990). This process is known as oceanic upwelling. In coastal areas, upwelling occurs when the wind blows parallel to the coast (for example, alongshore equatorward wind on an eastern boundaries of the ocean) and Ekman transport moves the surface water farther offshore (Gill 1982; Pickard and Emery 1990). In this situation, cold nutrient rich water is supplied to the upper layers and from deeper layer this is known as coastal upwelling.

Monsoon driven coastal upwelling

A number of studies have been undertaken where monsoon winds have been shown to cause coastal upwelling. Habeebrehman et al. (2008) have reported that regular seasonal monsoon cycles drive coastal upwelling along the southwest coast of India (eastern boundary of the Arabian Sea) during the summer monsoon wind season. They identified three phases of upwelling associated with different stages of summer monsoon wind: (1) a new upwelling phase, observed along the inshore waters between $8-10^{o}$N during the beginning of the summer monsoon and along the coast north of 13^{o}N during the peak and late monsoon; (2) a productive phase, observed along the inshore areas between $8-11.5^{o}$N during the peak monsoon, and (3) an aged upwelling, observed near 8^{o}N during the late summer monsoon.

A recent study in the Taiwan Strait (Hong et al. 2009) found a positive correlation (r=0.6) between sea surface temperature anomalies and alongshore wind stress, supporting the hypothesis that the southwest monsoon wind, which prevails during summer, is a favourable wind for upwelling on the west coast of the Taiwan Strait. Moreover this study showed that El Niño events

are largely responsible for inter-annual variability of coastal upwelling in the Taiwan Strait. Such inter-annual variability is important because it has implications for primary productivity and fisheries.

Udarbe-Walker and Villanoy (2001), investigated the structure of two potential upwelling areas (northwest Luzon and east Mindanao) in the western Philippines sea using historical *in situ* data. They found that upwelling in both areas is driven by the northeast monsoon winds resulting in offshore Ekman transport. But compared to other conventional upwelling systems in the world, the cold water does not reach the surface and is therefore not detectable by satellite sensors. Instead, a strong, deep thermocline is established. Another monsoon-driven upwelling area is observed in the South China Sea, northwest of Luzon and north of the Sunda shelf during the winter monsoon and off the east coast of Vietnam during the summer monsoon (Liu et al. 2002).

Finally Sarhan et al. (2000), investigated the driving mechanisms of upwelling in the north-western Alboran Sea and found that a combination of two mechanisms were involved: (1) wind stress, and (2) southward drift of the Atlantic Ocean Jet. They found that these two upwelling mechanisms operate in different places. The wind-driven upwelling prevails inshore and the upwelling driven by the drift of the Atlantic Ocean Jet occurs offshore.

Currents and topographically driven coastal upwelling

Currents and topography have been shown to play a important role in driving coastal upwelling. Song and Chao (2004), used a three-dimensional coastal ocean model to investigate the effect of topographic variation on coastal upwelling. They identified some characteristics which affect upwelling: (1) topographic variations cause uneven upwelling distributions and meandering currents; (2) the cyclonic eddy can enhance upwelling and create an upwelling core on the inshore side of the current and (3) alongshore topography transports inshore waters farther offshore, thus increasing cross-shelf exchange of water masses.

Roughan and Middleton (2002), investigated the causes of upwelling off the east coast (western boundary) of Australia and identified four mechanisms: (1) wind stress, (2) encroachment of

the East Australia Current onto the continental shelf, (3) acceleration of the current resulting from the narrowing of the continental shelf at Smoky Cape, and (4) the separation of the East Australia Current from the coast. Their study showed that both the strength of the current and its proximity to the coast determined the nature of the upwelling response. The encroachment of the East Australia Current onto the shelf contributed to the intensity of the upwelling, whereas the separation of the current from the coast, contributed to the prevalence of upwelling.

Other similar cases of current-driven upwelling are found in the North Sea–Baltic Sea transition, the south-east coast of Madagascar and the south coast of Brazil. Lund-Hansen and Vang (2003) found that, in the North-Baltic system, upwelling is induced by the interaction of high velocity currents and bottom topography. Here the high velocity northward flow forces bottom, cold, nutrient rich water to rise up the slope to the surface. Easterly winds in the area only have an indirect influence on upwelling (Lund-Hansen and Vang 2003).

In the case of the south-east Madagascar Current, divergence from the coast at the southern tip of the land mass induces upwelling along the south coast of Madagascar (Lutjeharms and Machu 2000; Ho et al. 2004). In the case of the South Brazil Bight Campos et al. (2000) suggested that upwelling is driven by cyclonic meanders of the Brazil Current and winds play a minor role. More recently Palma and Matano (2009) suggested that it is driven by the interaction of poleward flow in the Brazilian Current and bottom topography associated with changes in the coastline orientation.

Upwelling near Angoche

Two potential upwelling sites have been identified off the Mozambican coast. One is the Delagoa Bight cyclonic lee eddy in the southern region around 25^{o}S (Lutjeharms and da Silva 1988; Quartly and Srokosz 2004), and the other is near Angoche (Figure 2.3) in the northern region around 16^{o}S (Nehring et al. 1987). These areas are separated by a distance of about 2000 km.

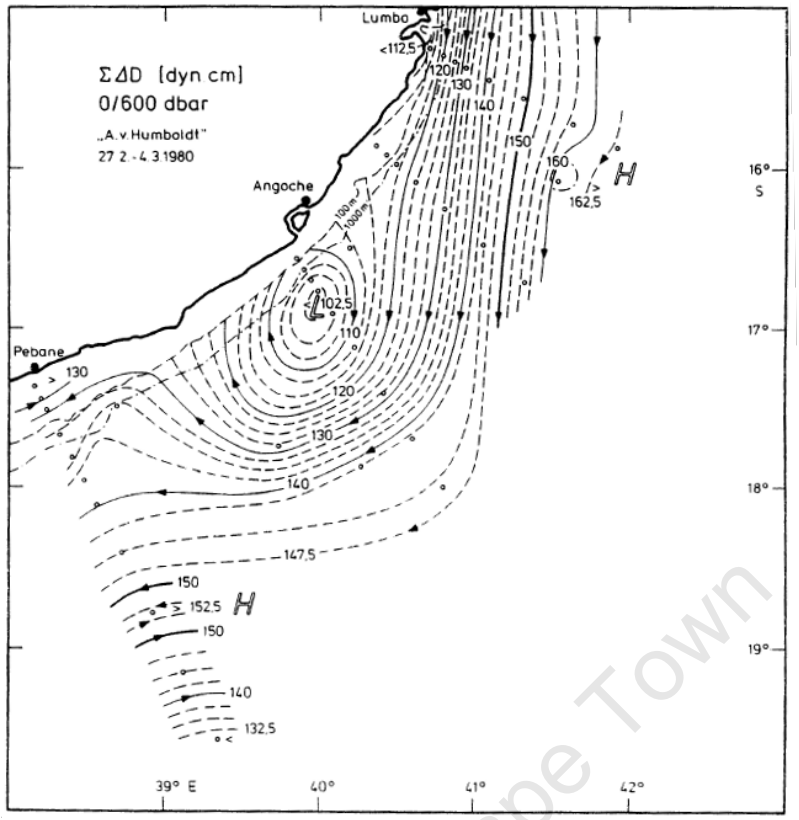

Figure 2.3: Dynamical topography of the sea surface relative to the 600 dbar level with geostrophic currents represented with arrows and the core of low pressure (L) indicating the Angoche lee eddy (Nehring et al. 1987).

Nehring et al. (1987) investigated the general structure, dynamics, and productivity of the waters off the Mozambique coast during an oceanographic cruise in February-March 1980. They found a coastal cyclonic lee eddy off Angoche, and attributed the origin of this cyclonic eddy to the continuous passage of the Mozambique Current. Since then, Sætre and da Silva (1982, 1984) and de Ruijter et al. (2002) have revealed that a continuous, persistent Mozambique Current does not exist. Ridderinkhof and de Ruijter (2003) and Lutjeharms (2006) suggested that the Angoche lee edge eddy forms during the southward propagation of intense anti-cyclonic eddies. Nehring et al. (1987) showed that the coastal cyclonic lee eddy can have a diameter of about 100 km and that deep cold water is upwelled in the core of the eddy. They also showed that upwelling is associated with enhanced surface Chl-a levels, enhanced nutrients and high productivity (phytoplankton).

Recent studies support the existence of the upwelling cell off Angoche. Ridderinkhof and de Ruijter (2003), observed a cyclonic lee eddy against the Angoche coast for 15 days in a 19

month time series of current meter data between April 2000 and November 2001. Their study did not investigate upwelling but several studies have shown that cyclonic eddies can induce upwelling in their core (Gill 1982; Nehring et al. 1987; Udarbe-Walker and Villanoy 2001; Song and Chao 2004).

The upwelling region near Angoche appears to be unique on the northern coast of Mozambique. Potentially, it can play an important role in the productivity of the region especially in terms of the Sofala Bank fisheries production. However, the upwelling cell has not been investigated in any detail. This study aims to focus only on the Angoche upwelling region to understand its spatial and temporal variability, its persistence and the driving mechanisms.

Chapter 3

Description of the upwelling off northern Mozambique

3.1 Introduction

Nehring et al. (1987) noticed an upwelling feature near Angoche (∼16°S), identified by anomalously high Chl-*a* values at the core of a cyclonic lee eddy. These high Chl-*a* levels were the highest observed in all the Mozambique Channel (Nehring et al. 1987). Ridderinkhof and de Ruijter (2003), also observed a cyclonic eddy at the same place during 15 days in August as part of a 19 month period of observation, but they did not investigate the upwelling. Nehring et al. (1987) survey (February−March) was not long enough to estimate the persistence of upwelling. Their study had not focused on the area of upwelling, thus the extent of the upwelling area is still unknown.

This chapter describes the occurrence and spatial and temporal variability of shelf edge upwelling off northern Mozambique using MODIS satellite, *in situ* (18 m) mooring between 2003−2007 and two cruise survey (in December 2008 and August 2009) data. Statistical analysis such as skewness for MODIS gridded Chl-*a* data and wavelet analyses for the *in situ* time series are performed to address four key questions (questions 1−4 as first raised in chapter 2):

- Where does the shelf edge upwelling cell off northern Mozambique occurs? Where is its core?
- What is the spatial extent of the shelf edge upwelling off northern Mozambique?
- When do upwelling events occur off northern Mozambique? Is there a seasonal cycle?
- How persistent is the shelf edge upwelling off northern Mozambique?

3.2 Data and methods

Study area

Angoche is located on the western side of the northern Mozambique Channel, on the coast of the Nampula province in northern Mozambique, at a latitude of approximately 16°S (Figure 2.1). At this location the coastline retracts westward and the continental shelf is narrow (Chapter 2). This is the northern limit of the Sofala Bank, which is the most important fishing ground for shallow water shrimps (family PENAEIDAE) in Mozambique.

This study was conducted within an area delimited by 12 to 20°S and 35 to 45°E (Figure 3.1). Based on results from satellite MODIS data, shipboard CTD and XBT data and skewness analysis of MODIS Chl-*a*, three small areas (one control point site and two upwelling core regions) were defined (Figure 3.1). There are referred to as: (1) the UTR (underwater temperature recorder) site, the control site where the UTR mooring is placed, (2) the shelf site and (3) the slope site. The last two sites were chosen because they represent consistent areas of upwelling off northern Mozambique.

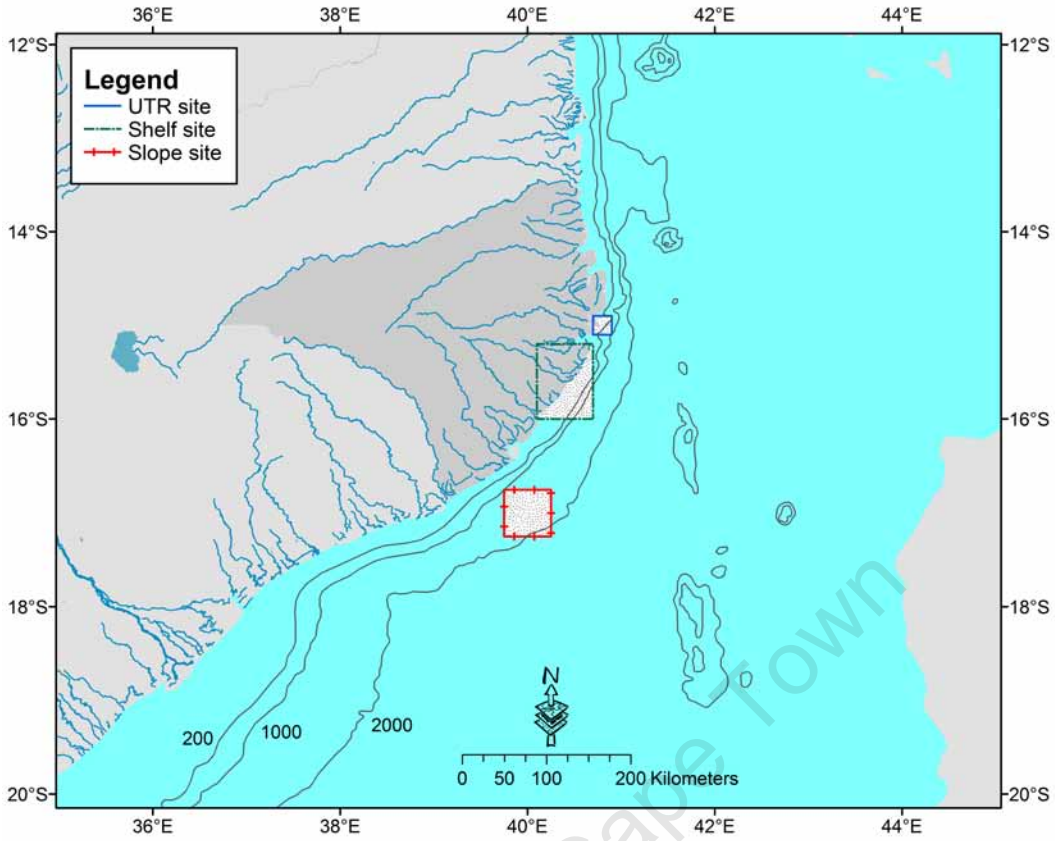

Figure 3.1: Map of the study domain off northern Mozambique (12−20^{o}S and 35−45^{o}E) showing three reference sites: (1) the UTR site (14.90−15.10^{o}S and 40.70−40.90^{o}E, blue box), (2) the shelf site (15.20−16^{o}S and 040.10−40.70^{o}E, green box) and (3) the slope site (16.75−17.25^{o}S and 39.75−40.25^{o}E, red box).

Satellite MODIS SST and Chl-*a* data

Aqua is a NASA Earth Observing System (EOS) satellite designed to collect information on the earth's water cycle. This satellite was launched in a low orbital altitude of 705 km on 4 May 2002. The orbit is circular, near-polar and sun-synchronous, with the ascending node passing from south to north and crossing the equator in the afternoon at 13:30 (local time). *Aqua* covers the surface of the earth in one to two days at a rate of 20.3 rpm (source MODIS web site `http://modis.gsfc.nasa.gov/`, last visited January 2010).

MODIS is the instrument on board the *Aqua* satellite that measures in-water variables. It is a wide swath sensor covering a large area of 2330 km cross track by 10 km along track at its nadir, at an average orbital data rate of 6.1 Mbps. It uses a complex optical system consisting of a double-sided-mirror with a scan angle of about 55 degrees on either side of the nadir and

a simple mechanical system.

MODIS has 12 bits of high radiometric sensitivity (quantization) in 36 spectral bands (groups of wavelength). These multi-spectral bands enable the detection of different components in the water, avoid bottom effects, and avoid the need for an accurate atmospheric correction factor. Five of these bands (in the mid and far infrared) are used for SST, nine (in the visible wavelength) are used for ocean colour including chlorophyll-*a*. The remaining bands are used for clouds, water vapor and atmospheric correction (source MODIS web site `http://modis.gsfc.nasa.gov/`, last visited January 2010). A detailed description of the MODIS instrument and *Aqua* satellite is given in the MODIS website: `http://modis.gsfc.nasa.gov/`.

In this study, two variables were used from the MODIS *Aqua* sensor namely MODIS Sea Surface Temperature (SST) and MODIS Sea Surface Chlorophyll-*a* Pigment Concentration (Chl-*a*). Data were supplied in binary format by the Marine Remote Sensing Unit at the University of Cape Town. Details of these data follow:

MODIS-SST data for the Angoche domain (12−20^{o}S and 35−45^{o}E) were extracted from the MODIS daily global coverage data set for the period January 2003 to December 2007 (five year period). The Level 2 product was used at a spatial resolution of 1 x 1 km (768 latitude x 960 longitude pixels for the entire domain). These data are already atmospherically corrected and geolocated, but not transformed to a map projection (i.e. ungridded). SST (^{o}C) values were generated using the standard MODIS algorithm for SST, which uses the mid and far infrared bands. The infrared radiometer sensor type was chosen for this study because it gives a better spatial resolution for resolving features in coastal areas than a microwave sensor (Tew-Kai and Marsac 2009). Note the data are available only for cloud free areas.

MODIS-Chl-*a* data for the same period as the SST data were extracted from the MODIS daily global 1 km Level 2 Chl-*a* data product. Chl-*a* concentrations (mg m^{-3}) were derived from the standard MODIS algorithm for Chl-*a* Case 1 sea water. Case 1 sea water is where phytoplankton and associated covarying decay products are the only substances affecting the optical properties of the water. This is valid almost everywhere except for some

coastal areas where there is some influence from the land. This applies to the Angoche area because there is no runoff from large rivers into the sea (Chapter 2). The Chl-*a* data were logarithmically transformed. Similar to SST, ocean colour products are affected by cloud cover, which reduces the available pixels.

Satellite data processing and presentation

The daily MODIS SST and Chl-*a* 1 km grid Level 2 products were converted into Level 3 products using *SeaDas* and *MatLab* software. SST and Chl-*a* Level 3 products consist of resampling SST and Chl-*a* Level 2 products in standard gridded map coordinates and averaging over a certain time period. The SST and Chl-*a* Level 3 products were produced daily and weekly at spatial resolutions of 1 x 1 km. The weekly composites consist of 8-day composite images, where valid data pixels were averaged over eight days. This was done to improve missing values in the 1-day data set caused by cloud cover, although some short period (less than eight days) variability may be lost. These 1 km grid Level 3 products were used to generate four time series of 1823 daily SST images, 229 weekly SST composite images, 1823 daily Chl-*a* images and 229 weekly Chl-*a* composite images.

The time series data were extracted from the original daily SST and Chl-*a* 1 km grid Level 2 data sets and from the weekly SST and Chl-*a* Level 3 composite image data sets between 2003 and 2007 at all three selected areas (Figure 3.1). At each of these sites, all pixels were spatially averaged. Because of computer limitations (low memory capacity to deal with large data-sets), the original 1-day Level 2 data set was split into months (i.e. 60 subsets of data) and the 8-day composite Level 3 data set into years (i.e. five subsets), then recombined into a single data set for the entire period.

In situ cruise survey CTD data

Vertical profiles of temperature, salinity and fluorescence were taken during two oceanographic cruise surveys in the northern Mozambique Channel as part of the Agulhas Somali Current

Large Marine Ecosystem (ASCLME) project onboard the research vessel (R/V) Dr. Fridtjof Nansen. Data were supplied by the ASCLME project.

On the ASCLME cruise 2008, between 28 November and 17 December 2008, 96 Conductivity, Temperature and Depth (CTD-model Seabird 911 plus) stations (Figure 3.2) were carried out from the surface down to 10 meters above the sea bottom, or to 1000 m where the bottom depth was greater than 1000 m. Data were sampled at 1 m intervals during the down cast. In addition, 46 Expendable Bathythermographs (XBT−model Lockheed Martin sippican Deep Blue) were deployed down to a depth of 760 m between the CTD stations to improve the spatial resolution of the temperature data (Figure 3.2). One transect (T) containing five CTD stations and five XBTs was defined to investigate the upwelling (Figure 3.2). Both the CTD and XBT data were loaded in real time to the vessel computer in ASCII format.

In addition, during the ASCLME cruise 2009, between 10 and 16 August 2009, 42 CTD (model Seabird 911 plus) casts were taken along six shore-normal transect (Figure 3.2). The survey progressed from north to south (i.e. from transects 6−1), in the same direction as the propagation of anti-cyclonic eddies (Schouten et al. 2002, 2003). Each transect took about one day to complete. For this survey the maximum station depth was 1500 m and data were sampled every 1 m (down cast). Data were loaded in real time into the data base of the research vessel in ASCII format (.cnv) using *Seabird Seasave* software.

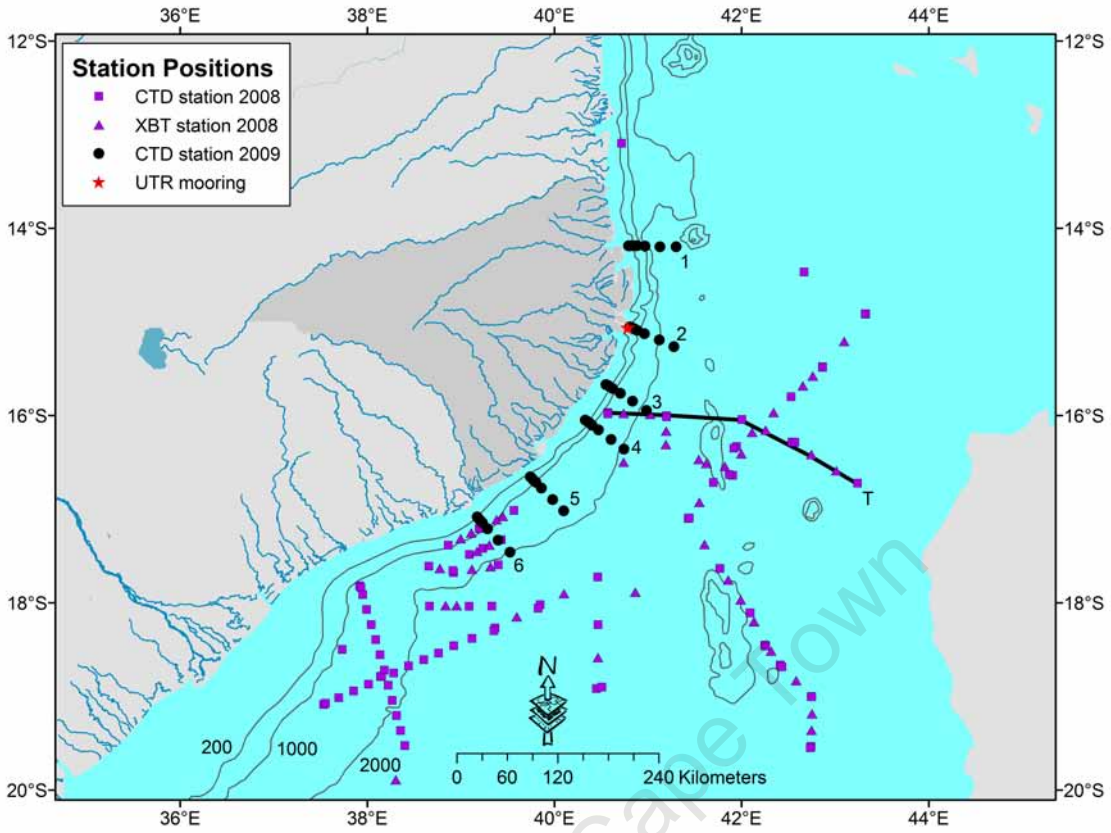

Figure 3.2: Map of the study domain off northern Mozambique showing the stations distribution for the ASCLME cruises 2008 and 2009, and the mooring station. The letter T refers to the transect of 2008 and numbers $1-6$ to the transects of the 2009 cruise.

CTD data processing and presentation

The data were subjected to quality assurance to remove erroneous data. Data were then imported into a standard spreadsheet and vertical profile plots produced for each station. Horizontal and vertical plots for temperature, salinity and fluorescence were produced using *Ocean Data View* (ODV) software. Horizontal maps were produced for four depths i.e. surface (5 m), 20, 50 and 100 m depths. Vertical sections for the six shore-normal transects (1, 2, 3, 4, 5 and 6) were produced (Figure 3.2).

In situ moored UTR data

A temperature time series between October 2002 and September 2007 (five-year period) was obtained from an underwater temperature recorder (UTR, model Seamon mini temperature

record), deployed at a depth of 18 m adjacent to Mozambique Island (15^{o}03.87'S and 040^{o}47.10'E) (Figure 3.2). Temperature measurements were made every hour and stored in the internal memory of the instrument (UTR). The data were then uploaded and converted to ASCII format. More information about this mooring site is available at `http://www.oceanafrica.com`.

UTR data processing and presentation

Data quality was checked using a standard spreadsheet in which the data set was examined and searched for erroneous values (none were found). Data were then imported into *Matlab* and data averaged to daily values, i.e. all 24 hour values of a day from 0 (zero) to 23 hour were averaged into a daily mean value. A five-year time series of daily temperature was produced for the period January 2003 to September 2007.

Skewness (spatial) analysis

The skewness of sea surface Chl-a concentrations was used to summarize the dominant position and persistence of upwelling (i.e. high Chl-a) events in the study area between October 2002 and September 2007. Skewness analysis has been employed as a statistical tool to investigate regions of mesoscale variability in physical oceanography by, for example, Thompson and Demirov (2006) and Backeberg et al. (2009). Skewness is a measure of the asymmetry of the distribution of a variable (Trauth 2006). Positive skewness means that the distribution of data has a long tail that extends to the right of the mean value and the mean is bigger than the mode. The skewness of a symmetrical Gaussian distribution is zero, and the mean is equal to the mode (no skewness). The skewness of Chl-a data at each grid point over time was computed using the Fisher equation:

$$skewness = \sum_{i=1}^{N} \frac{\left(X_i - \bar{X}\right)^3}{S^2} \tag{3.1}$$

where N is the number of Chl-a values X_i at each grid point at each time i, $\bar{X}$ is the sample mean and S^2 is the variance.

Prior to any calculation, the distribution of Chl-a data for the entire domain and period was

checked to see whether the distribution is symmetric or asymmetric (skewness). The original 3D data array containing 1825 days, 768 pixels latitude and 960 pixels longitude was reshaped to one vector of 1,345,536,000 elements by multiplying the 3D array, $1825 \times 960 \times 768$, and then plotting in a frequency distribution. Chl-*a* skewness was calculated for each grid point of the entire domain (960×768 pixels) over time (N=1825 days) using equation 3.1, and plotted in a horizontal map using *Matlab* software.

Thompson and Demirov (2006) demonstrated that skewness depends on the duration of the phenomenon at a location; the greater the skewness value, the shorter the duration. Knowledge of the area is needed to interpret zero skewness and decide whether it represents permanent or no upwelling. Interpretation of the results followed the conventions described in table 3.1.

Table 3.1: The interpretation of the skewness of Chl-*a* data for the upwelling off Angoche.

Attribute	Interpretation
Sign	Positive skewness is an indicator of upwelling events, showing areas of extreme events of high (above the mean) Chl-*a* concentration at the surface. Negative skewness means there are no upwelling events in the area.
Value	A large value of positive skewness means low frequency of upwelling events at that location. A small value of positive skewness implies high frequencies of upwelling events.
Zero	Zero skewness can either mean permanent upwelling or no upwelling at all.

Wavelet (time series) analysis

Wavelet analysis was used to investigate variations in frequency of occurrence and amplitude of cool water events (upwelling). The application of wavelet analysis or the wavelet transformation as a statistical tool for time series analysis in oceanography has been increasing since the 1990s. Wavelet analysis decomposes a time series into time-frequency amplitude and phase space, so that one can detect dominant modes and how these modes change with time (Emery and Thomson 2001; Thompson and Demirov 2006).

The Morlet wavelet was chosen as the "mother" wavelet, because it is simple, commonly used and looks like a wave. It is defined as the product of a complex exponential wave function and

the Gaussian function, which determines the envelope of the wavelet:

$$\psi_0(\eta) = \pi^{-1/4} e^{i\omega_0} e^{-\eta^2/2} \tag{3.2}$$

where $\psi_0(\eta)$ is the wavelet function at nondimensional time η and ω_0 is the wave number, here set to six which is the default parameter for the Morlet wavelet.

For wavelet analysis at different scales (s) for each time series χ_n with equal sampling time δt, a sample size *N*, a time index n ranging from zero to *N-1,* and a frequency index k ranging from zero to *N-1* the discrete Fourier transform ($\hat{\chi}_k$) is defined as:

$$\hat{\chi}_k = \frac{1}{N} \sum_{n=0}^{N-1} \chi_n e^{-2\pi i k n/N} \tag{3.3}$$

To make the wavelets comparable to other wavelet functions, the wavelet function is normalized as:

$$\hat{\psi}(s\omega_k) = \left(\frac{2\pi s}{\delta t}\right)^{1/2} \hat{\psi}_0(s\omega_k) \tag{3.4}$$

The wavelet W_n for each s is computed using the convolution theorem, defined as the inverse Fourier transform of the product between the function $\chi_n$and ψ :

$$W_n(s) = \sum_{k=0}^{N-1} \hat{\chi}_k \hat{\psi} * (s\omega_k)\, e^{i\omega_k n \delta t} \tag{3.5}$$

where the angular frequency (ω_k) is given as:

$$\omega_k = \begin{cases} \frac{2\pi s}{N\delta t} : K \leq \frac{N}{2} \\ -\frac{2\pi s}{N\delta t} : K \geq \frac{N}{2} \end{cases} \tag{3.6}$$

This study uses a Wavelet model (*Matlab* script) developed by Torrence and Compo (1998) available at URL: `http://paos.colorodo.edu/research/wavelet/`. One of the advantages of this model is inclusion of statistical tests. The model requires time series with constant

sampling intervals and without gaps. For this reason it could not be used on the MODIS SST and Chl-*a* data. A complete description and step by step guide to carry out wavelet analysis (using *Matlab*) is provided in Torrence and Compo (1998).

Time series data of daily near-sea surface temperature derived from the UTR for the period October 2002 to September 2007 (N=1825 days) were used as input variables to run the model. The UTR data set was checked for missing data, time errors, and to confirm the start and end times. The seasonal cycle was removed from the original UTR time series to reduce the seasonal influence for the wavelet transformation. The seasonal cycle was removed by calculating the daily averages over the period 2002−2007 (five-year). These were then subtracted from the corresponding daily values of the original data set, and divided by the standard deviation to construct a normalized time series. Input information is summarised in table 3.2.

Table 3.2: Input variables/parameters for the Torrence and Compo (1998) wavelet model

Variables/parameters	Symbol	Units	Value	Comment
Sampling time	δt	days	1	constant for time series
Plotting time	N	days	1852	5-year period from October 2002 to September 2007
Pad	Pad		1	the time series remain power of two ($N = 2^m$, where m is an integer)
Spacing scales	δj		0.25	smaller values take computer time
Smallest scale	s_0	day	2	highest detectable frequency resolvable for any time series is $s_0 = 2 \times \delta t = 2$ x 1day
Significance level	α		0.95	

Pad adds zeroes at the beginning and end of the time series to minimize edge distortion (ringing) due to finite length data.

3.3 Results

Horizontal distribution

Spatial distribution of long-term mean MODIS SST and Chl-*a*

The long term means of the MODIS SST and Chl-*a* data at each single grid point of data for the Angoche domain for the period 2003 to 2007 are shown in Figure 3.3. Mean SST varies from 26 to 29^{o}C (Figure 3.3a), characterized by a positive gradient from west to east. Relatively cooler water (<27^{o}C) is evident along the western edge of the Mozambique Channel. In particular a thin cool water lens at the coast is seen near Angoche (∼16^{o}S), which widers to the south along the Sofala Bank (20^{o}S). Warmest water (29^{o}C) occurs in the eastern edge of the Mozambique Channel off the Madagascar coast. The mean surface Chl-*a* (Figure 3.3 b) is greatest (about 2 log(Chl-*a* in mg m^{-3})) in the coastal region of the Sofala Bank (16−20^{o}S) and along the Madagascar coast. Lowest values (∼0.03 mg m^{-3}) occur in the open sea. Low mean Chl-*a* concentrations are found in the region off Angoche, ranging from 0.03 to 3 mg m^{-3}.

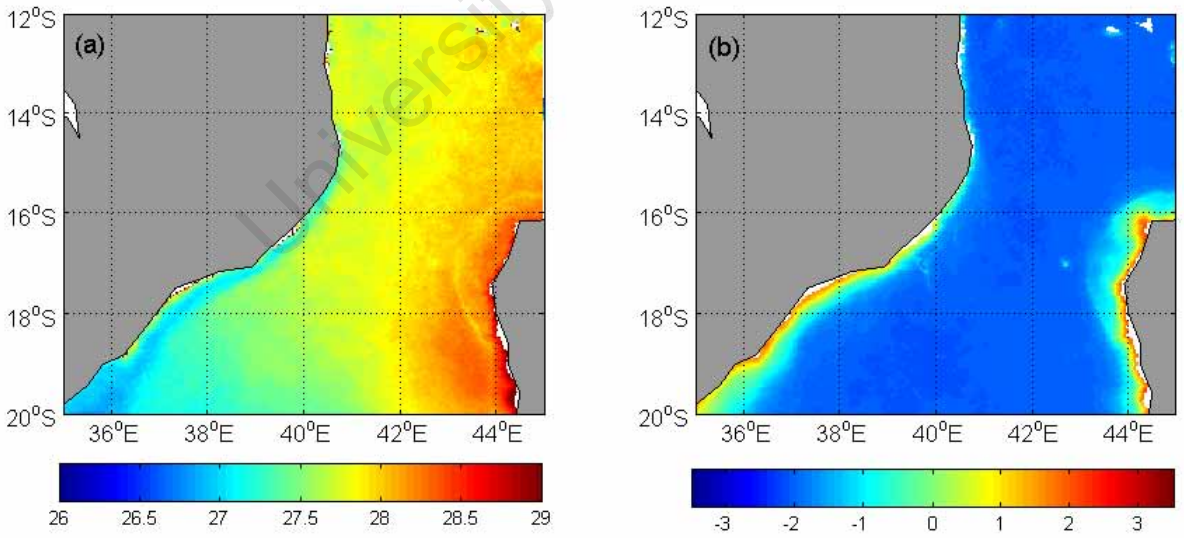

Figure 3.3: Map of long term mean for (a) MODIS SST (^{o}C) and (b) log(MODIS Chl-*a*)(mg m^{-3}) data over the whole Angoche domain for the period 2003 to 2007.

Spatial distribution of MODIS SST and Chl-*a*

Time series of five years of 1 x 1k gridded MODIS SST and Chl-*a* fields between 2003−2007 were produced. To more easily visualize the mesoscale features, the entire time series for SST and Chl-*a* were incorporated into an animation of daily (1825 days) and weekly (229 8-day composite) images. The animations were carefully examined for signatures of upwelling (cool water $\sim 2^o$ in range and enhanced Chl-*a* $\sim$ 1 mg m^{-3}) at the surface near Angoche. The animations were summarized in Tables 3.3 and 3.4. The numbers represent the numbers of days in which cool water and/or slight enhancements of Chl-*a* events (upwelling signatures) were observed. The grey scale represents the number of days with cloud cover more than 30% of the area off Angoche. This was estimated subjectively and includes areas with unavailable pixels of data resulting from missing satellite over passes.

Clearly the region is strongly influenced by cloud cover. Clouds were more persistent from October to February than from April to September. Only in two months (April 2003 and August 2004) was cloud cover found to be less than 10 days. Despite the presence of cloud, the available pixels were sufficient to show upwelling features (Figure 3.4, 3.53.6 and 3.8).

Cool water (Table 3.3) and enhanced Chl-*a* (Table 3.4) was observed in the area of interest most months. July was the only month in which cool water and high Chl-*a* was not observed in the time series. Cool water and enhanced Chl-*a* were only observed in May in 2006. September 2003 had the most observed days with upwelling indicators: 19 days for high Chl-*a* and 16 days for cool water. Cool water and enhanced Chl-*a* were more frequent between August and March and less frequent from March to July.

Table 3.3: Summary of MODIS SST images between 2003 and 2007. Numbers represent days with cool ($\sim 2^{o}$C, decrease) water and grey scale days with more than 30% cloud cover.

Year	Jan	Feb	Mar	Apr	May	Jun	Jul	Aug	Sep	Oct	Nov	Dec	Total
2003	9	1	9	4	0	2	0	8	16	9	10	10	78
2004	1	0	2	1	0	3	0	11	16	7	5	3	49
2005	4	5	3	5	0	1	0	12	4	3	9	6	52
2006	4	4	2	1	6	11	0	3	3	11	5	7	57
2007	1	0	0	1	0	13	0	1	4	N/A	N/A	N/A	20

Legend

<=9 days
10 - 19 days
>=20 days

Table 3.4: Summary of MODIS Chl-a images between 2003 and 2007. Numbers represent days with enhanced Chl-a water (~ 1 mg m^{-3}) and grey scale days with more than 30% cloud cover.

Year	Jan	Feb	Mar	Apr	May	Jun	Jul	Aug	Sep	Oct	Nov	Dec	Total
2003	10	1	11	7	0	3	0	12	19	10	10	11	94
2004	1	0	6	1	0	5	0	14	17	8	6	4	62
2005	5	8	4	8	0	1	0	15	4	3	10	6	64
2006	5	5	3	1	6	12	0	3	4	12	7	8	66
2007	1	0	0	1	0	14	0	3	6	N/A	N/A	N/A	25

Legend

<=9 days
10 - 19 days
>=20 days

Three of the best examples of upwelling were chosen for detailed description. Figure 3.4 and Figure 3.5 illustrate the evolution of an upwelling (enhanced Chl-a and cool SST) event off Angoche. Notice that SST is not as useful as Chl-a for detection of upwelling. The SST and Chl-a patterns (cool water and enhanced Chl-a, respectively) describe different stages of the upwelling event between 15 August and 23 September 2004. Similar protracted events were observed in other parts of the time series, for example, between 12 August and 23 September

2003, and between 6 August to 3 September 2005 (not shown). Shorter period events of about four days were also observed.

The six sequential images of surface Chl-a (Figure 3.4) show that the upwelling area increasing in size and propagated southward along the shelf off Angoche. On 15 August 2004 (Figure 3.4a) there was little Chl-a at the surface off Angoche, but a slight increase in Chl-a on the shelf north of Angoche (between $14-15^{o}$S and $41-43^{o}$E) is evident, representing the earliest phase of the upwelling event. Figure 3.4b on 22 August shows elevated levels of Chl-a (about 2 mg m^{-3}) around 15^{o}S off Angoche. Four days later (Figure 3.4c), the higher Chl-a (triangle) is observed moving southward along the coast ($15-16^{o}45$'S and $40-41^{o}15$'E) and increasing in size, indicating the upwelling to be well developed. On 31 August (Figure 3.4d) the high Chl-a moves to the south. A small component started to move south-eastward and spread over a larger area. After nine days (Figure 3.4e) the high Chl-a appears as a filament which spreads south-eastward in the channel. The last image on 23 September 2004 (Figure 3.4f) shows the high Chl-a to have moved southward of Angoche to the Sofala Bank where its size is reduced.

Figure 3.5 (for SST) highlights a similar sequence of events but not as well designated as in Figure 3.4 (Chl-a). Here the upwelling feature increases in size and moves southward. The early stages of upwelling (15 and 22 August) are not apparent in the SST image (Figures 3.5a and 3.5b) but can be seen on 26 August, 31 August, 9 September and 23 September 2004 (Figures 3.5c, d, e and f, respectively).

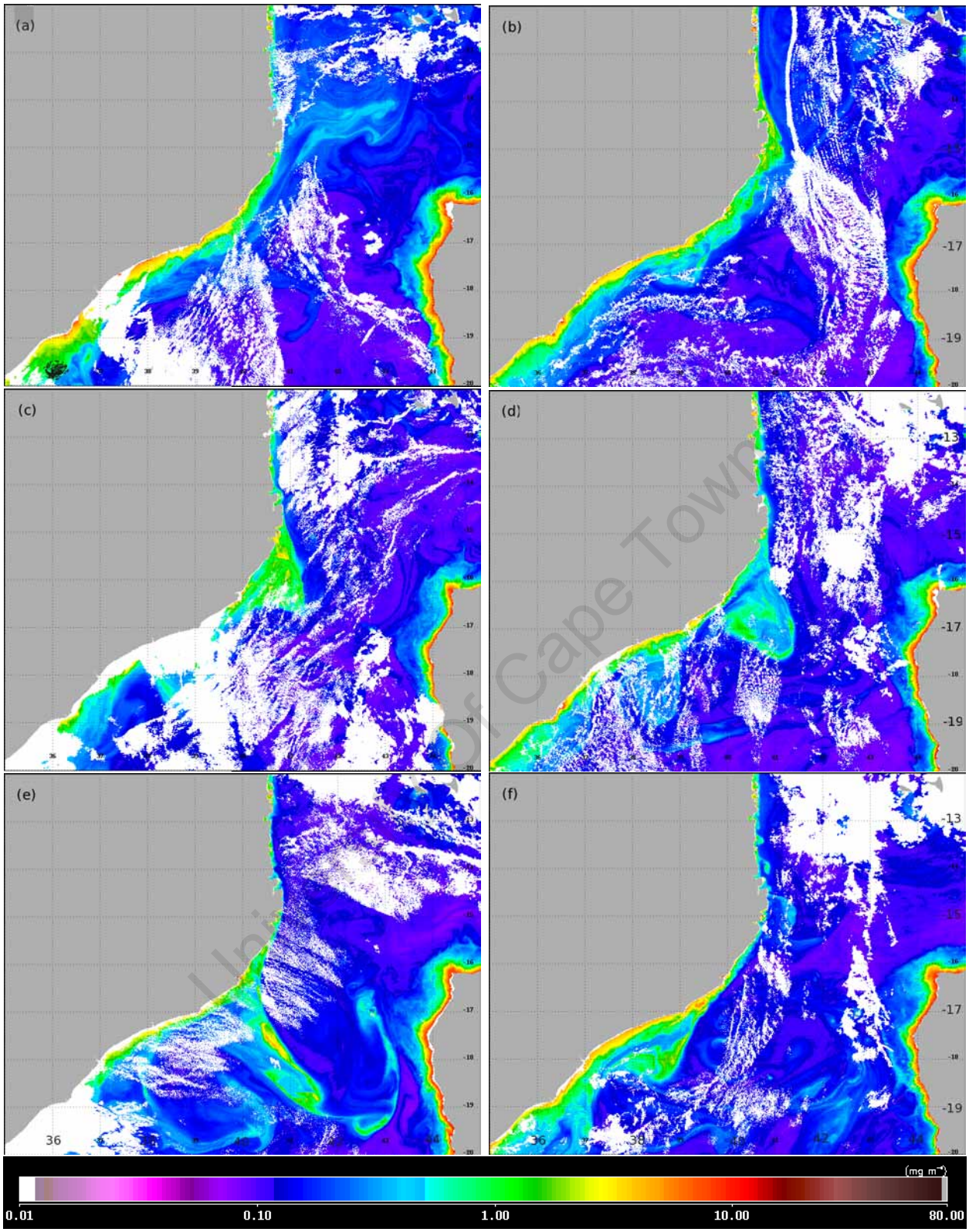

Figure 3.4: Daily 1 km gridded MODIS surface Chl-*a* concentrations (mg m^{-3}) illustrate the evolution of an upwelling event between 15 August and 23 September 2004 (a) 15 August, (b) 22 August, (c) 26 August, (d) 31 August, (e) 9 September and (f) 23 September 2004.

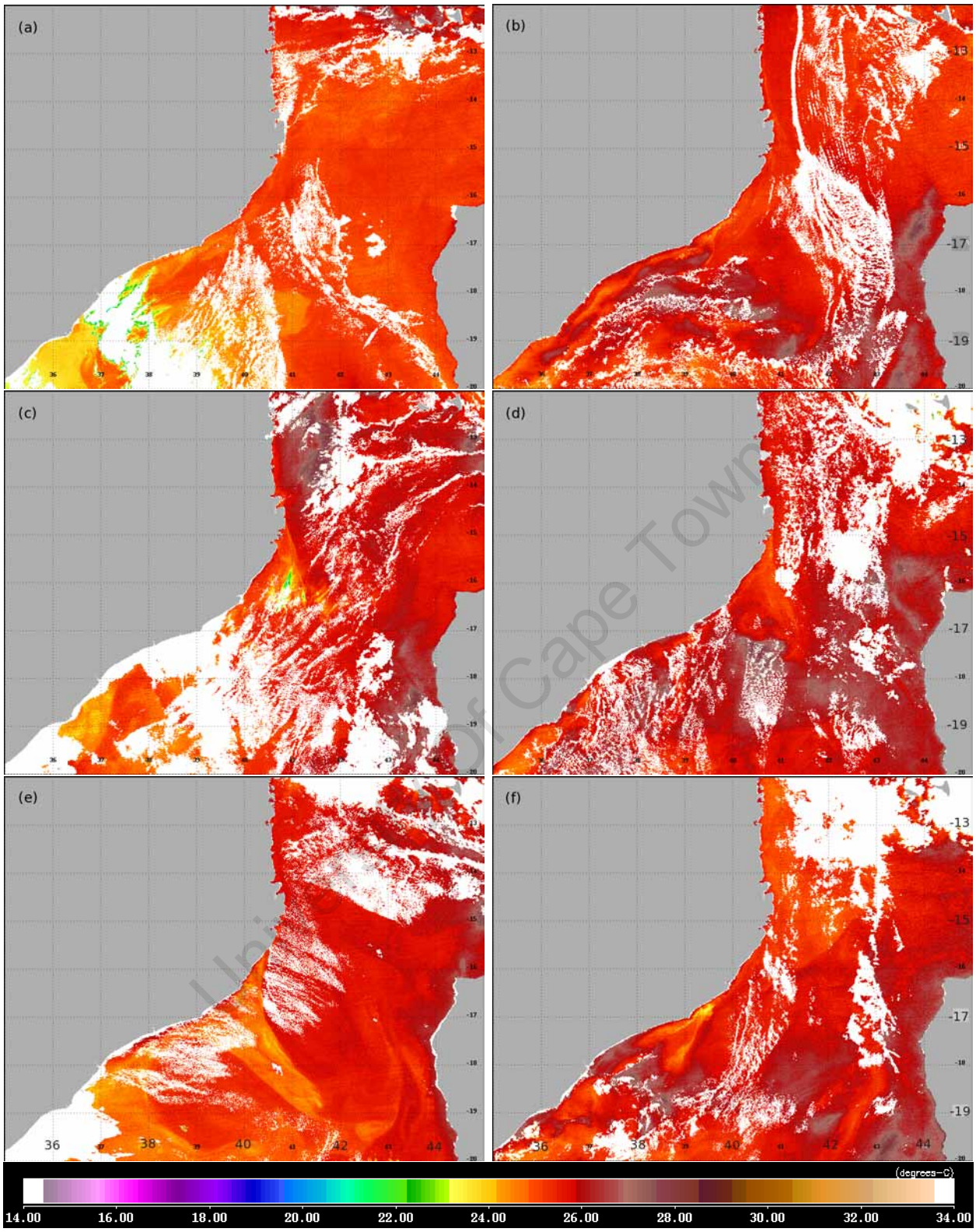

Figure 3.5: Daily 1 km gridded MODIS sea surface temperature (^{o}C) illustrate the evolution of an upwelling event between 15 August and 23 September 2004 (a) 15 August, (b) 22 August, (c) 26 August, (d) 31 August, (e) 9 September and (f) 23 September 2004

Figure 3.6 shows images of daily MODIS SST and Chl-a data for three different days (and years), specifically selected to illustrate the maximum area of upwelling in northern Mozambique. Note that December (Figure 3.6e) is warmer (brown) than August (Figure 3.6a and c). The SST images generally match well with the Chl-a, but again, the upwelling events are more discernable in the Chl-a data than the SST data. On 31 August 2004 (Figure 3.6b), the high Chl-a extended in a southwest direction with the edge at 17^{o}30' and 41^{o}20'E. On 14 August 2005 (Figure 3.6d) the upwelling area is spread more southward with the edge at 18^{o}15'S and 39^{o}20'E. On 9 December 2006 (Figure 3.6f) the high Chl-a spread southward to 17^{o}30'S and 041^{o}20'E. The patterns on 31 August 2004 and 9 December 2006 have similar shapes and upwelling area, a pattern commonly seen through the time series.

These maximum areas of the upwelling (for example those in Figure 3.6) were digitized into Geographical Information System (GIS) solution—displayed in Figure 3.7a. A composite image comprising all these areas was produced (Figure 3.7b). This represented the maximum area of upwelling off northern Mozambique (near Angoche) where cool water or enhanced Chl-a was observed for at least one day during the period in study. This total area was calculated to be 67 887 km^2.

Figure 3.8 shows a sequence of the most extreme upwelling event observed in the time series. The top images for 27 September 2006 show the early appearance of upwelling with cool surface water (not clear in Figure 3.8a) and slight enhancement of Chl-a (Figure 3.8b) between 16^{o}30' and 17^{o}S. On 4 October 2006 the upwelling is more defined with cool SSTs (Figure 3.8c) and very high Chl-a concentrations (Figure 3.8d) centred at 17^{o}S. Two days later (6 October 2006) the cooler SSTs and the high Chl-a are still evident (Figure 3.8e and f, respectively) and spread over a large area along the coast (reaching 15^{o}S). The maximum Chl-a concentrations (about 7 mg m^{-3}) observed on 4 and 6 October 2006 (Figures 3.8d and f) were the highest values observed in the entire time series. By 8 October 2006 (not shown here), the high Chl-a values had disappeared (later stage of upwelling).

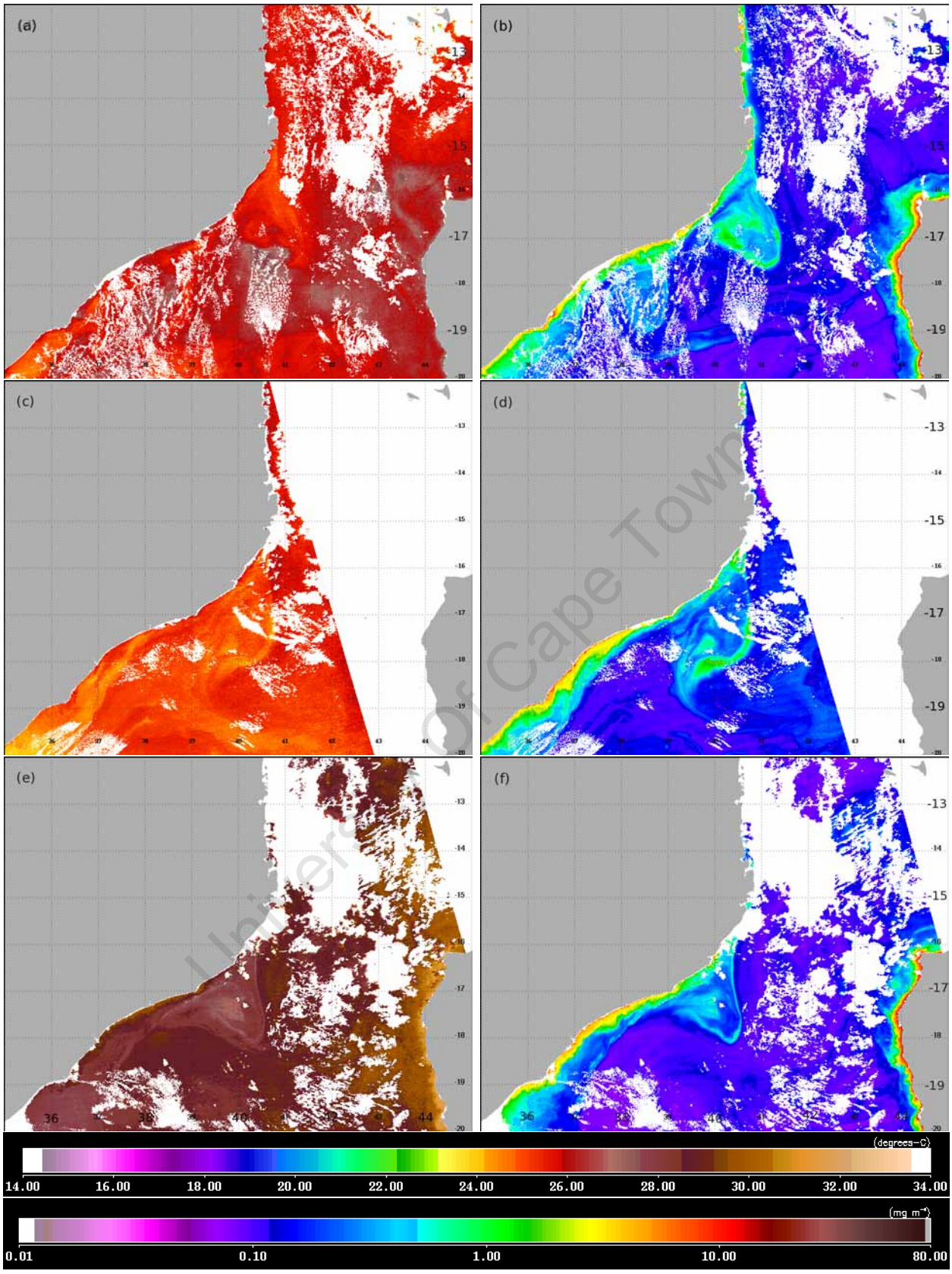

Figure 3.6: Example of the upwelling area on different days, evident from cool SST (^{o}C) (a) 31 August 2004, (c) 14 August 2005 and (e) 09 December 2006 and for high Chl-*a* (mg m^{-3}) (b) 31 August 2004, (d) 14 August 2005 and (f) 09 December 2006.

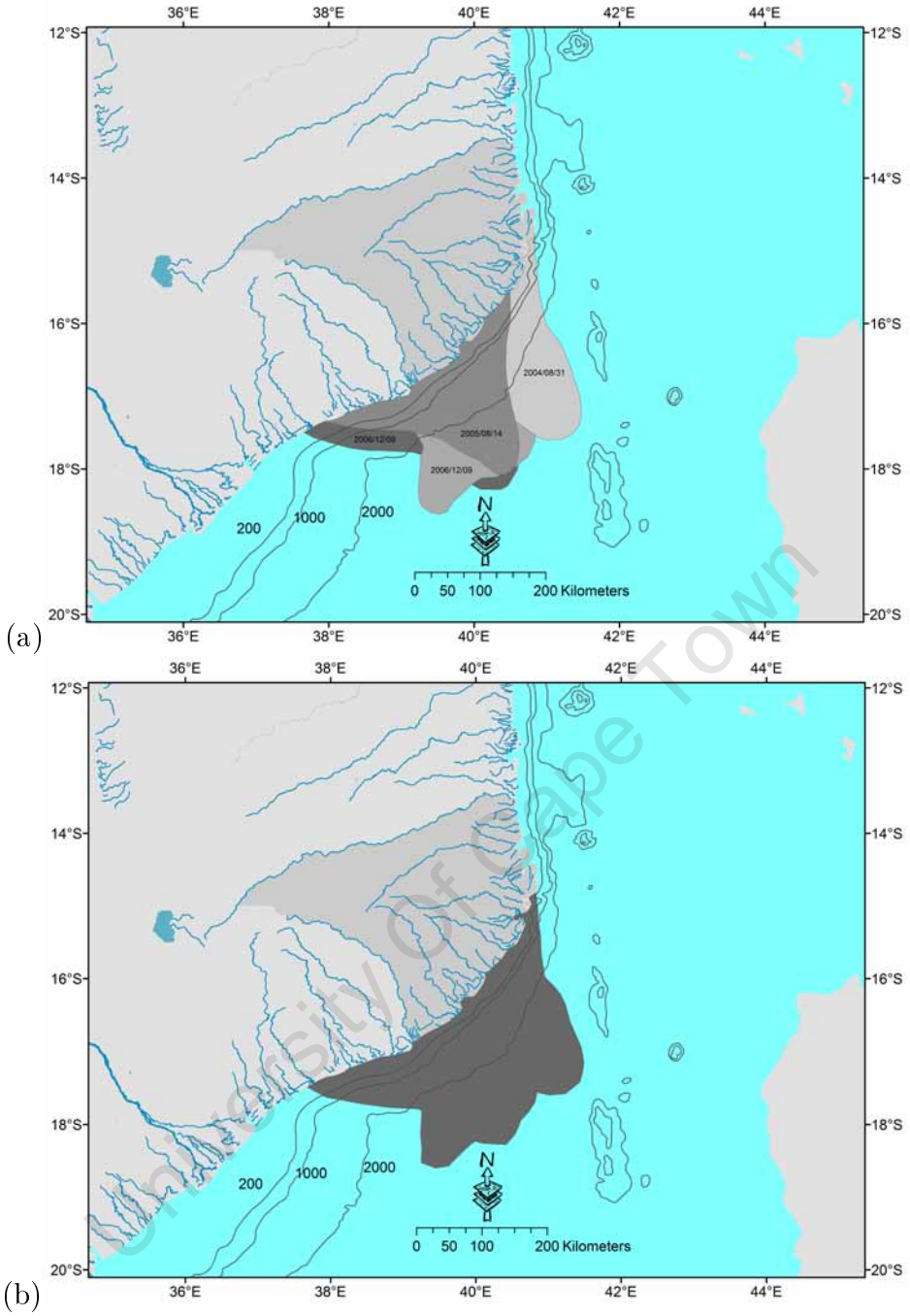

Figure 3.7: (a) Areas in which signatures of upwelling were observed during separate events between 2003−2007 (b) total area shown in (a) influenced by cool water and high Chl-*a*.

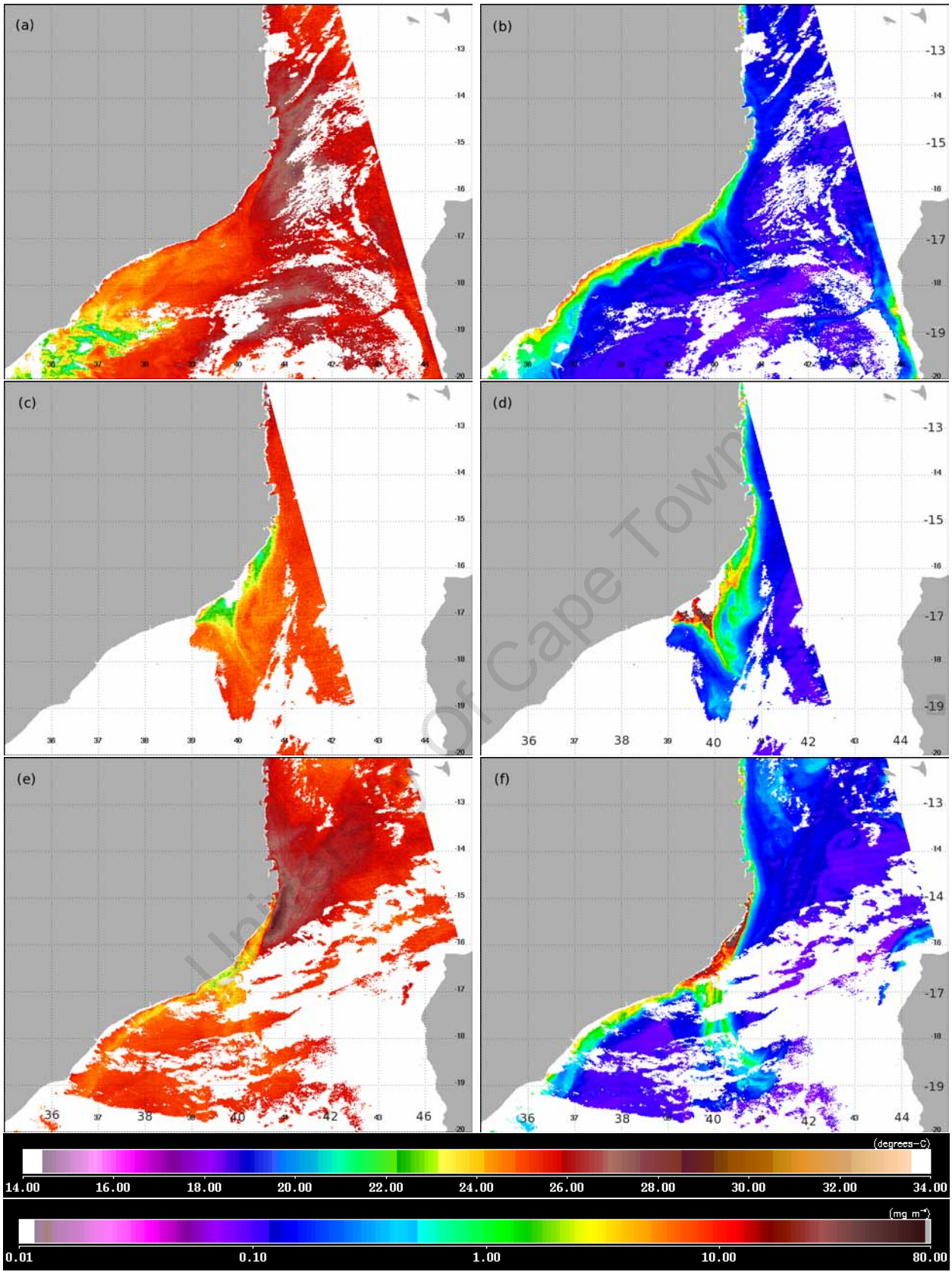

Figure 3.8: Sequence of the most extreme upwelling event observed during the study period showing SST (left) and Chl-*a* (right). (a) and (b) 27 September 2006, (c) and (d) 4 October 2006 and (e) and (f) 6 October 2006

Skewness distribution of MODIS Chl-*a*

The frequency distribution of MODIS sea surface Chl-*a* concentrations (Figure 3.9a) is asymmetrical, showing positive skewness (skewness=7, N=1825), with a long tail to the right, indicating numerous events with Chl-*a* concentrations much greater than the mean. The skewness values in Figure 3.9b are positive in the region off Angoche depicting two core regions: (1) the shelf core region between 15−16^{o}S and (2) the slope core region centred at 17^{o}S and 40^{o}E. The skewness value (1.0) at the shelf core region is smaller than the slope core (1.5). The skewness of the Sofala Bank region is near zero.

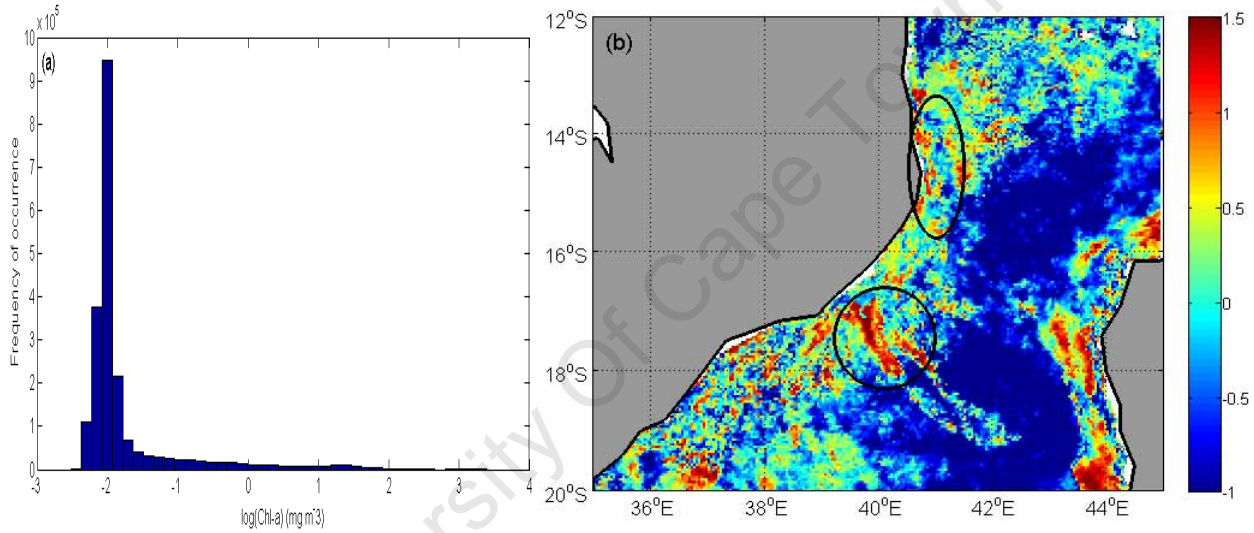

Figure 3.9: (a) Empirical frequency distribution of Chl-a concentrations and (b) spatial distribution of skewness values calculated for 2003 to 2007.

Horizontal distributions of cruise survey CTD data

Horizontal distributions of temperature and fluorescence at four nominal depths (surface (5 m), 20 m, 50 m and 100 m) derived from CTD data collected during the ASCLME cruises in December 2008 and August 2009 in the northern Mozambique are shown in Figures 3.10−3.12. Horizontal distributions of fluorescence data were not available for the 2008 cruise. Cool water signatures are apparent between 15−16^{o}S (shelf core region) and around 17^{o}S and 40^{o}E (slope core region) in each of the images but the signal is more discernable with depth.

In the 2008 data in the 5 m (Figure 3.10a) and 20 m (Figure 3.10b) depth layers, temperature

was warm (∼29 and ∼ 28^{o}C, respectively) and almost homogenous, changing only about 1^{o}C. However, two relatively cool (28^{o}C in 5 m and 27^{o}C in 20 m layer) water regions are notable on the shelf (1) between 15 and 16^{o}S and (2) at 17^{o}30′S (Figure 3.10a and b).

In the 50 and 100 m depth layer a cross-shore temperature gradient with the minimum on the west coast and maximum off shore is observed (Figure 3.10c and d). The field of cool water at 16^{o}S on the shelf was still present and more evident, with temperature of approximately 22^{o}C at 50 m and less than 16^{o}C in the 100 m layer, significantly cooler than the area surrounding. The cool water at 17^{o}30′S is not observed in these two "deep" layers (Figure 3.10c and d).

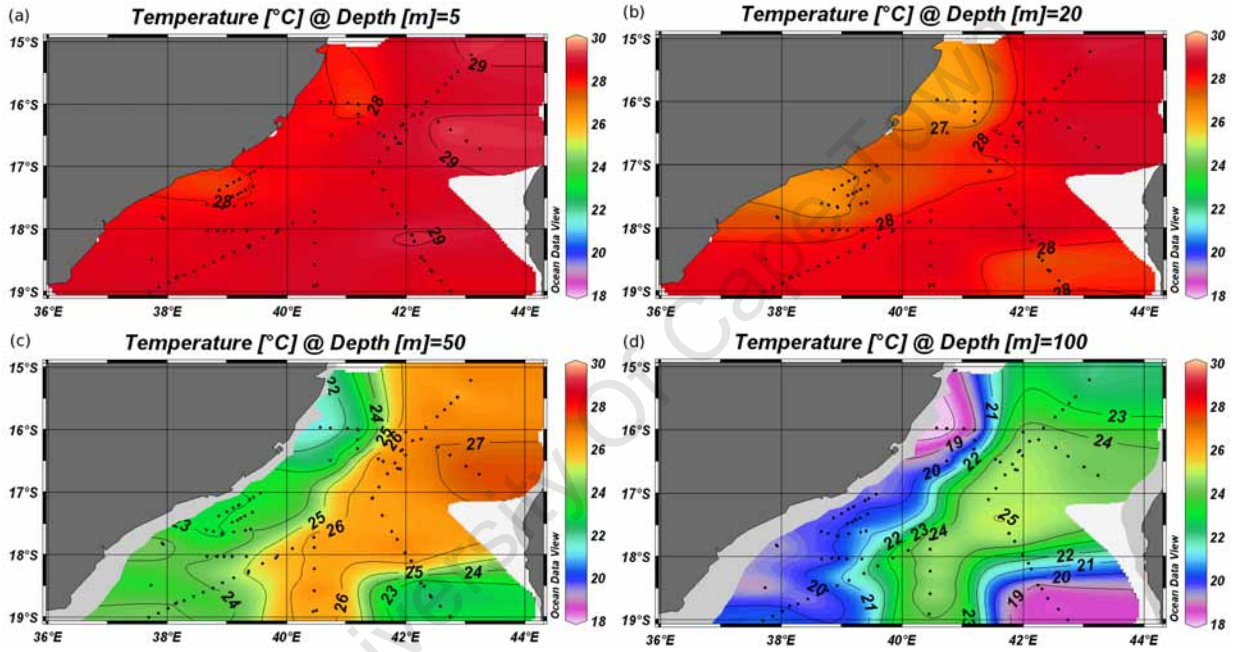

Figure 3.10: ASCLME cruise December 2008: Horizontal distributions of temperature (^{o}C) at different depths: (a) 5 m, (b) 20 m, (c) 50 m and (d) 100m. Dots refer to station locations.

In the 2009 data (Figure 3.11) isotherms exhibited a latitudinal temperature gradient at all depths, particularly in the 100 m layer with maximum temperatures ($>$ 24^{o}C) in the northern region and minimum temperatures (∼20^{o}C) in the southern region (Figure 3.11d). A cross-shore temperature gradient existed between 15−16^{o}S, with cool ($<$ 21^{o}C) water at the coast and warm ($>$ 24^{o}C) water offshore (Figure 3.11d). The observed range of temperatures is from 18 to 25^{o}C. The temperatures for the surface and the 20 m depth layer (Figure 3.11a and b, respectively) shows relatively homogeneous and warm (∼25^{o}C) water with little variability, less than 1^{o}C (in range) for the whole area. In the surface layer the isotherm of 25.4^{o}C is found

close to the coast between 15 and 16^{o}S (Figure 3.11a). At a depth of 20 m the isotherm of 25.4^{o}C moved seaward (Figure 3.11b) and cool water can be seen rising in the coastal region between 15 and 16^{o}S. Relatively cool water is observed centred at about 17^{o}S and 40^{o}E.

Figures 3.11c and d show a cool core region centred at about 17^{o}S and 40^{o}E with temperature of 23.5^{o}C in the 50 m layer and 18^{o}C in the 100 m depth layer. In these layers cool water was still observed rising on the shelf between 15 and 16^{o}S, being approximately 20^{o}C at 100 m depth.

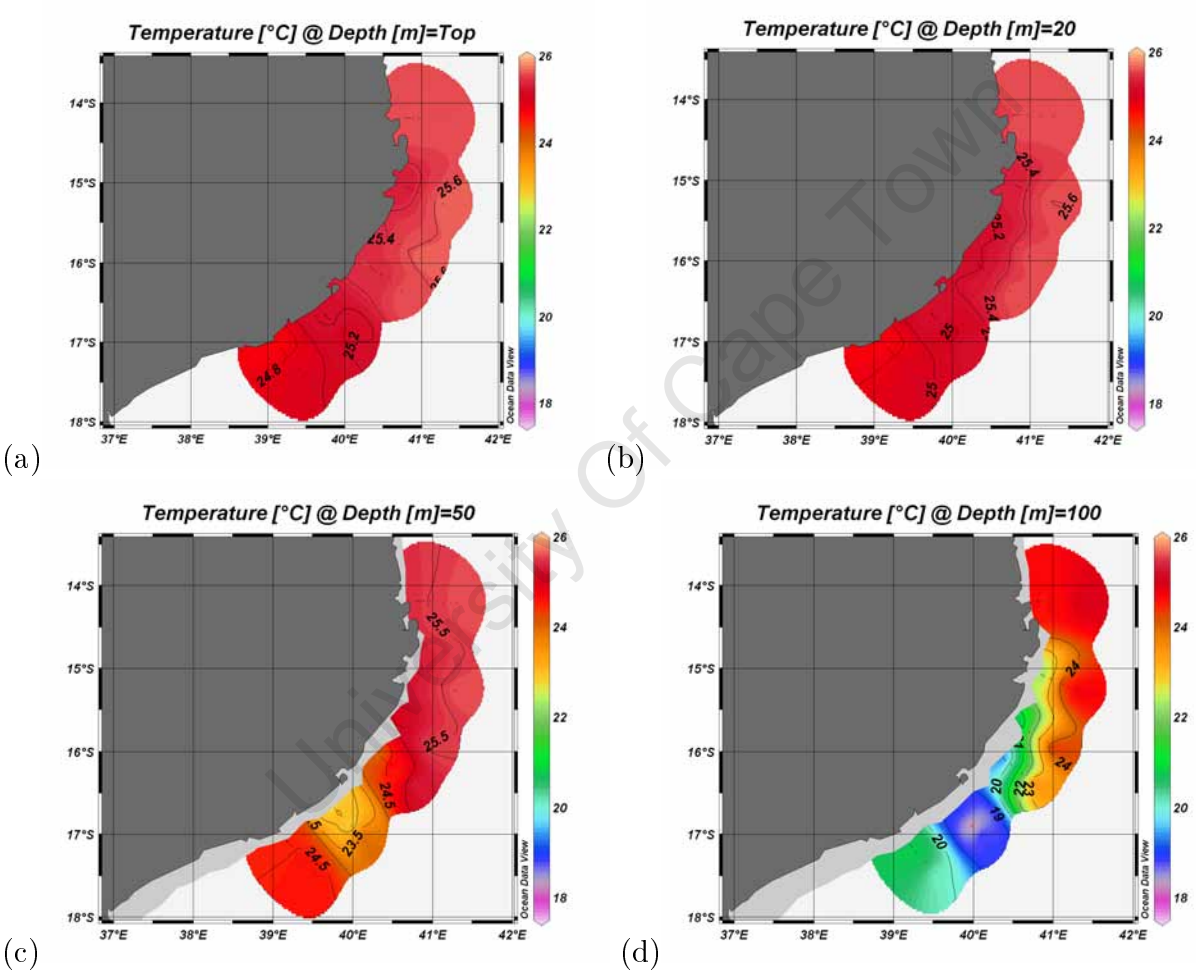

Figure 3.11: ASCLME cruise August 2009: Horizontal distributions of temperature (^{o}C) at different depths: (a) surface, (b) 20 m, (c) 50 m and (d) 100m. Dots refer to station locations.

Figure 3.12 shows the enhancement of fluorescence (Chl-a) is shallow, and does not reach the depth of 100 m. High fluorescence values were found in the depths above 50 m with a maximum of 0.2 μg l^{-1} along the coast between 15^{o}30' and 17^{o}S, and at the slope centred at 17^{o}S and 40^{o}E (Figure 3.12a-c). At the surface (Figure 3.12a) high fluorescence (0.2 μg l^{-1}) was found

in a small area centred at 17^{o}S and 40^{o}E (slope core region). At 20 m depth, the high slope fluorescence remained in the same position (17^{o}S and 40^{o}E), while the other high fluorescence (0.15 μg l^{-1}) region appears along the coast between 15 and 16^{o}S (Figure 3.12b). As the depth increases the fluorescence concentration decreases. At 100 m depth (Figure 3.12d), fluorescence levels drop to only 0.1 μg l^{-1}. In general, the fluorescence variability in this area was very small with a range from 0 to 0.2 μg l^{-1}.

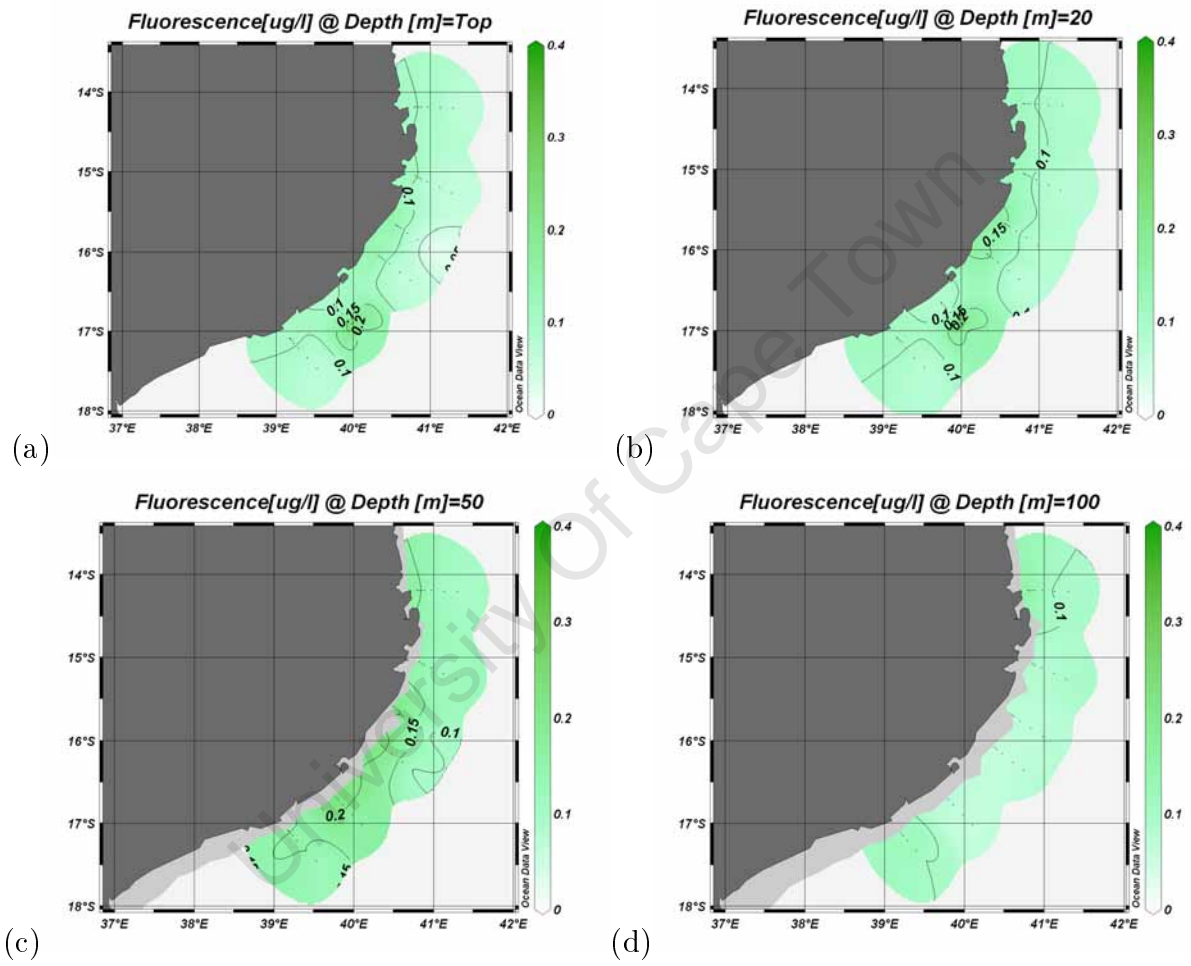

Figure 3.12: ASCLME cruise August 2009: Horizontal distributions of fluorescence (μg l^{-1}) at different depths: (a) surface, (b) 20 m, (c) 50 m and (d) 100m. Dots refer to station locations.

Vertical distributions

Vertical distributions of cruise survey CTD data

Two dimensional plots of temperature, salinity and fluorescence derived from CTD stations carried out during the ASCLME cruises in December 2008 and August 2009 are shown in Figures 3.13-3.16.

Figure 3.13 shows isolines of temperature and salinity to rise on the continental shelf with corresponding high fluorescence (Chl-a) levels near the sea surface in the coastal region off Angoche in December 2008. For example, note that the 18^{o}C isotherm was lifted from a depth of 200 m offshore (150 km distance from the coast) to 100 m at the coast (Figure 3.13a and b). Corresponding high fluorescence concentrations are found from the surface layer down to 75 m depth with maximum around 50 m on the western side of the section.

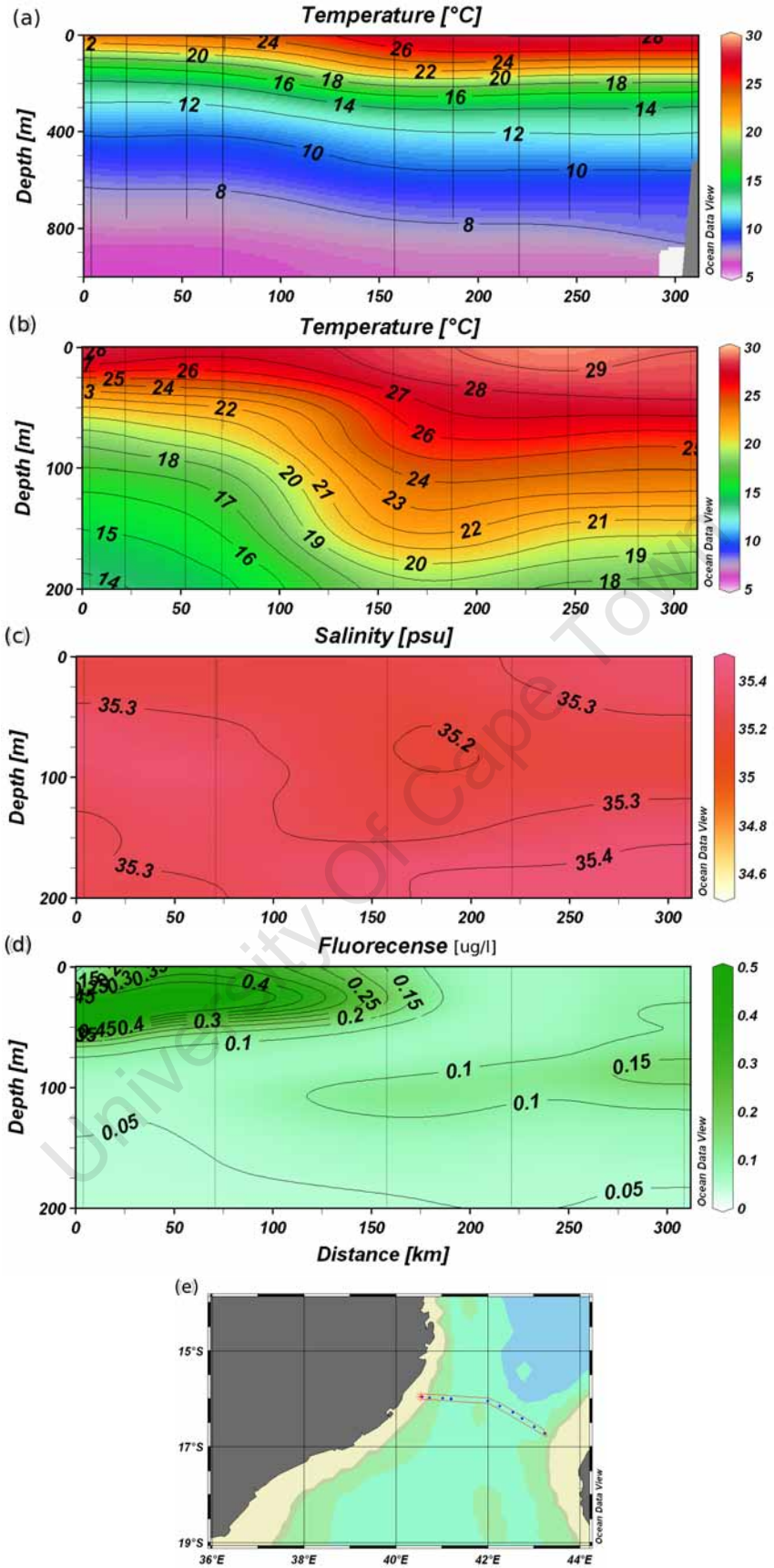

Figure 3.13: ASCLME cruise December 2008: vertical distribution of (a) temperature (^{o}C) to 1000 m, (b) temperature (^{o}C) to 200 m, (c) salinity (psu) and (d) fluorescence (μg l^{-1}) for (e) transect off Angoche. Vertical lines in a-d represent station positions.

In the 2009 data, there is also evidence of coastal upwelling along transect 3 around 16^{o}S (Figure 3.14). The deep temperature profile (Figure 3.14a) shows the thermocline to extend from near-surface to 200 m depth, with a deep, relatively homogenous temperature layer below the thermocline. Temperature ranged from 24^{o}C above the thermocline to 6^{o}C at 1200 m. The shallower temperature plot in Figure 3.14b shows inshore isotherms are observed to slope upward towards the coast. For example, the 18^{o}C isotherm is lifted from 200 m offshore (55 km from the coast) to 110 m at the shelf. Cold water ($<$16^{o}C) appeared below 150 m within 5 km of the coast. The upward-sloping isotherms towards the coast indicate a current flowing southward.

Salinity shown in Figure 3.14c is seen throughout the water column to range between 34 to 35.4 PSU. Isohalines also show a upward-sloping with vertical gradient with a minimum (34.8 PSU) at the surface and a maximum (35.5 PSU) at the bottom. Note that salinity did not show any influence of land runoff in the coastal area, with no horizontal gradient.

High fluorescence was found in the coastal area from the surface to about 75 m depth with a maximum of $\sim$ 0.2 μg l^{-1} centred at 50 m. The fluorescence maximum deepens with distance offshore and the deep chlorophyll maximum (DCM) was located at about 75 m depth offshore. In the surface layers of the channel (above the DCM), and the deep layers (below 100 m), fluorescence was homogenous with very low (almost zero) levels. Transects 4 and 5 (not shown here) exhibited a similar pattern to that shown in transect 3.

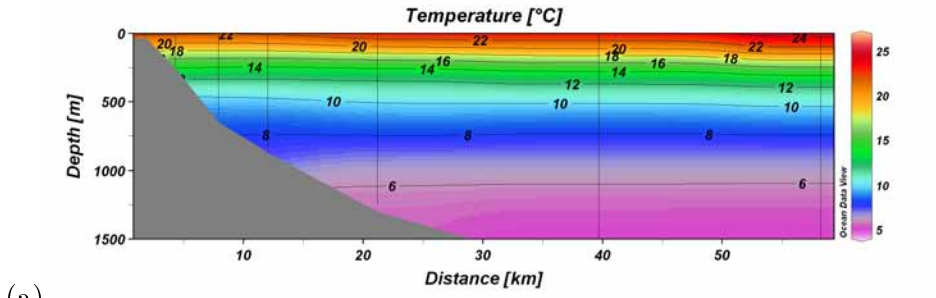

(a)

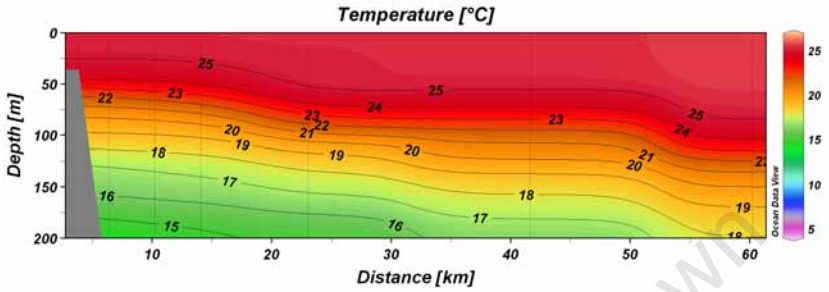

(b)

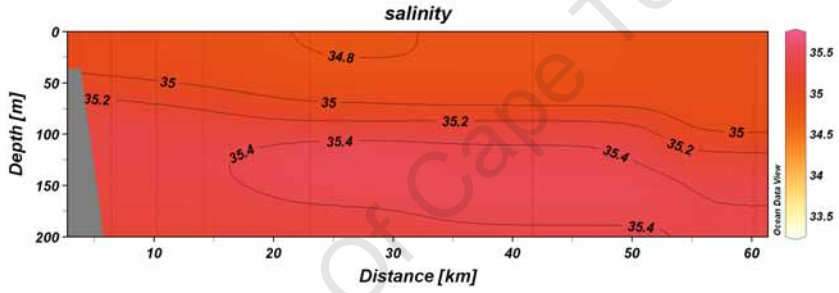

(c)

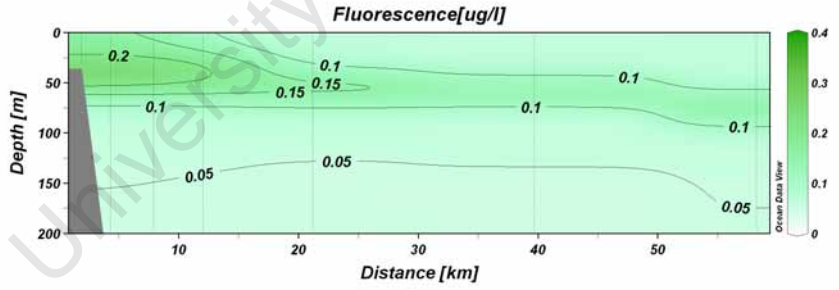

(d)

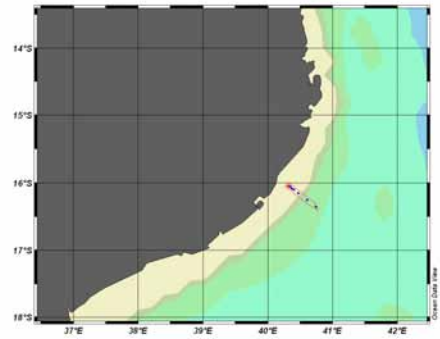

(e)

Figure 3.14: ASCLME cruise August 2009 transect 3 (see map): vertical distribution of (a) temperature (^{o}C) to 1500 m, (b) temperature (^{o}C) to 200 m, (c) salinity (PSU) and (d) fluorescence (μg l^{-1}). Vertical lines in a-d represent station positions.

Figure 3.15, shows the vertical distribution of temperature, salinity and fluorescence along transect 2. The temperature plot in Figure 3.15a shows two layers. (1) The surface layer has a strong vertical temperature gradient, which decreases from 22^{o}C at the surface to 10^{o}C at 500 m. (2) The homogenous (6^{o}C) deep layer is found below 500 m. The deep isotherms (8 and 6^{o}C) show slight downward sloping towards the coast, indicating an absence of coastal upwelling. Isotherms in the surface layer exhibited a doming in the middle of the transect between 25 and 50 km offshore. The observed doming in this transect indicates a cyclonic eddy centred at 35 km from the coast, with deep cold water in the core.

The doming is more prominent in the temperature plot in Figure 3.15b where isotherms are seen to dip at the coast and offshore parts of the transect, and are shallower in the middle between 25 and 50 km offshore. Here the isotherms reach the surface and produce slightly cooler surface water. For example, the 25^{o}C isotherm rose from 10 m depth at the coast and offshore, reaching the surface between 30 and 45 km offshore. In addition, the 16^{o}C isotherm is found deeper (175 m) at both extremes of the transect and shallow (125 m) in the middle of the transect.

High salinity water ($>$ 35 PSU) was observed in Figure 3.15c, with salinity showing little variability i.e. range from 35 to 35.4 PSU.

Fluorescence data (Figure 3.15d) indicate high fluorescence values (0.35 μg l^{-1}) from the surface to 50 m between 25 and 50 km offshore (middle section). This surface high fluorescence lies adjacent to a subsurface maximum (0.2 μg l^{-1}) at 50 m (DCM) between 25 km offshore and the coast. The deep layer is homogenous with low fluorescence. This transect suggests upwelling occurred between 30 and 50 km offshore.

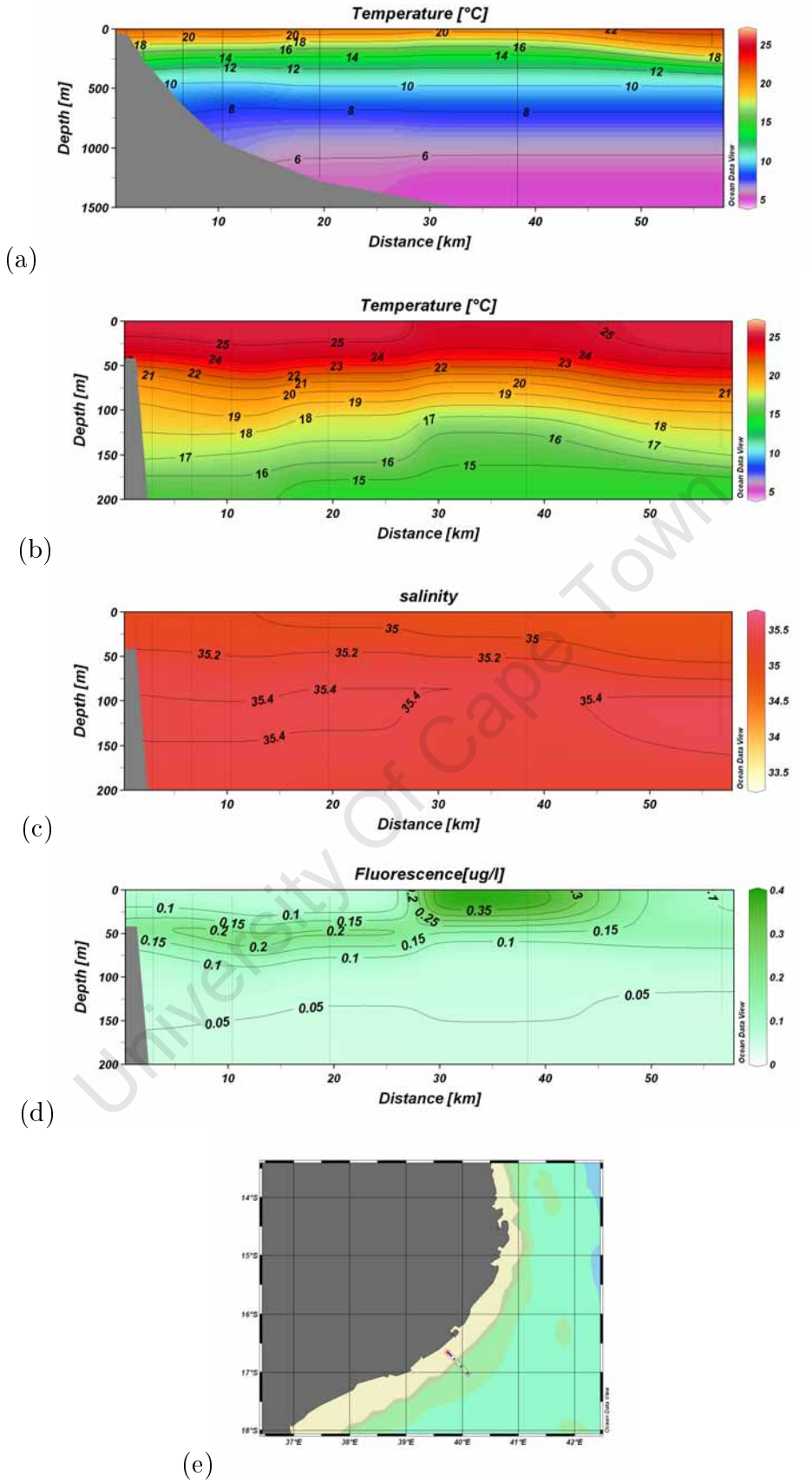

Figure 3.15: ASCLME cruise August 2009 transect 2 (see map): vertical distribution of (a) temperature (^{o}C) to 1500 m, (b) temperature (^{o}C) to 200 m, (c) salinity (PSU) and (d) fluorescence (μg l^{-1}). Vertical lines in a-d represent station positions.

Figure 3.16 shows vertical profiles along transect 1 (Figure 3.2). No upwelling is evident. Temperature data in Figure 3.16a show a surface layer with a strong negative vertical gradient, decreasing from 22^{o}C at the surface to 10^{o}C at 500 m. The isotherms of 8 and 6^{o}C in the deep water layer (below 500 m) show downward slopes towards the continental slope. Figure 3.16b shows that above the thermocline the coastal waters were mixed and slightly cooler than offshore waters (which were $>$ 25^{o}C) and below the upper mixed layer temperature varied uniformly with depth.

The salinity range was small from 35.2 to 35.4 PSU at the surface and 200 m, respectively (Figure 3.16c).

There was a high fluorescence concentration of 0.2 μg l^{-1} (Figure 3.16d) at 75 m depth (DCM) and located between 20 and 50 km offshore. The water column above and below this maximum is homogenous with very low fluorescence.

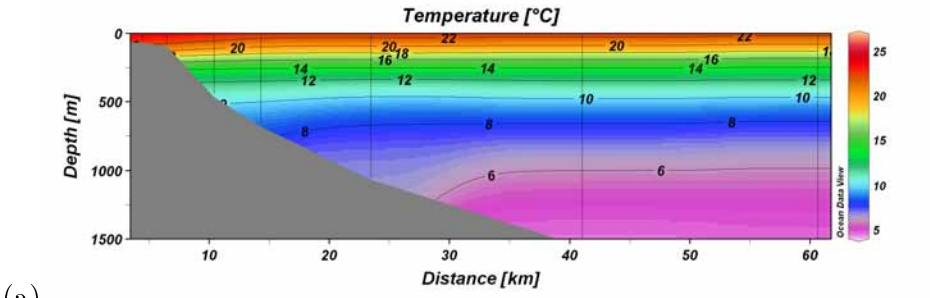

(a)

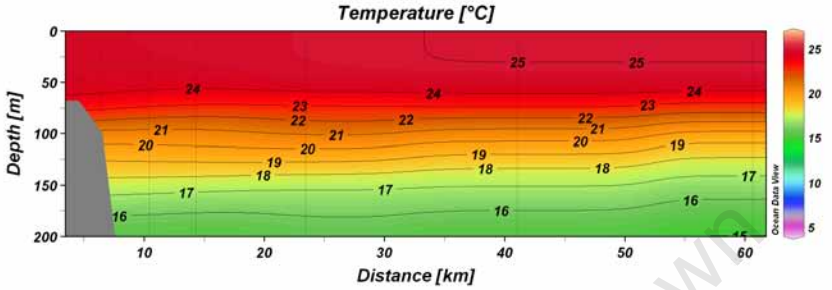

(b)

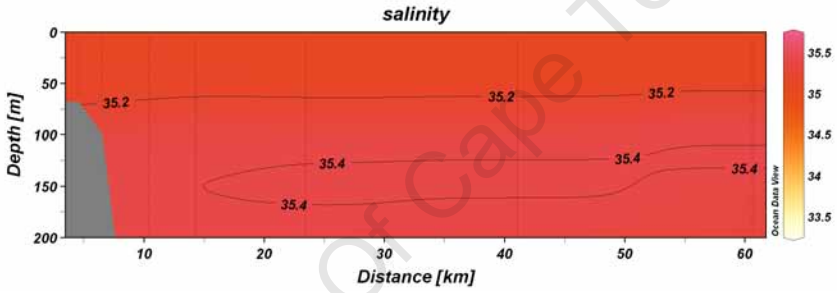

(c)

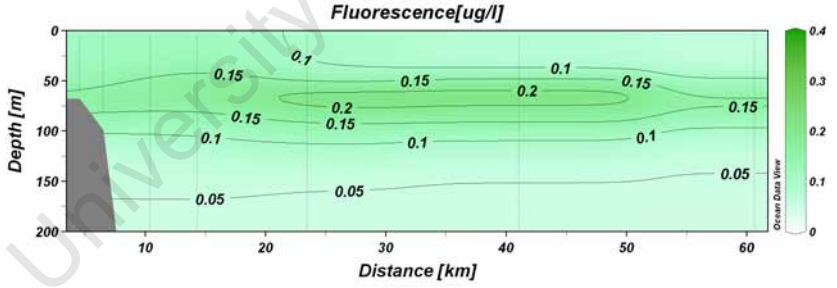

(d)

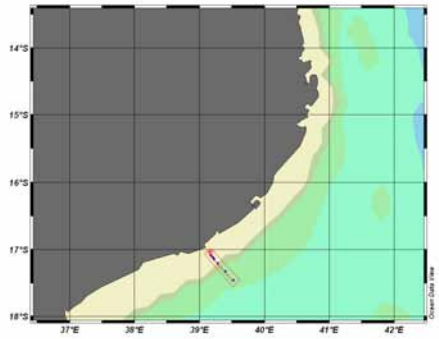

(d)

Figure 3.16: ASCLME cruise August 2009 transect 1 (see map): vertical distribution of (a) temperature (^{o}C) to 1500 m, (b) temperature (^{o}C) to 200 m, (c) salinity (PSU) and (d) fluorescence (μg l^{-1}). Vertical lines in a-d represent station positions

Time series

Time series for MODIS SST and Chl-*a*

The time series for both the daily MODIS SST and Chl-*a* data sets at all three sites (not shown) have many missing values due to cloud cover. As a consequence, the amplitudes of the observed seasonal cycle and intraseasonal variations are imprecise. To overcome this problem, 8-day composite images were used to produce a weekly time series of MODIS SST and Chl-*a* at the UTR site (Figure 3.17), the shelf site (Figure 3.18), and the slope site (Figure 3.19), for the period 1 January 2004 to 31 December 2007. Weekly data for 2003 were not available for MODIS SST.

The time series of weekly MODIS SSTs at the three sites (Figures 3.17a, 3.18a and 3.19a) show strong seasonal oscillations over a range of 6^{o}C, with a maximum of 31^{o}C in March−April and a minimum of 25^{o}C in July−September. Cool water events were observed between August and March (spring−summer months) every year, with average amplitudes of 2^{o}C.

The time series of Chl-*a* at the UTR site (Figures 3.17b) shows a weak seasonal oscillation in Chl-*a* with relatively high Chl-*a* concentrations between October and March (spring−summer months) and low in winter. At the shelf and slope sites, there is no seasonal oscillation in Chl-*a*, but occasional intraseasonal variability is evident (Figure 3.18b and 3.19b). The variability is generally characterized by low amplitude ($\sim$1 mg m^{-3}) events in all three areas. Such an event was observed in the first week of October 2006 (Figure 3.8). High Chl-*a* is evident at the shelf site (7 mg m^{-3} Figure 3.18b) and also at the slope site (4.5 mg m^{-3} Figure 3.19b) but only weakly visible at the UTR site (0.75 mg m^{-3} Figure 3.17b). A similar event but of lower levels ($\sim$ 2 mg m^{-3}) was also observed in September to October 2004 at these three sites.

It appears that some of these enhanced Chl-*a* events coincided with cool water events. For example, October 2004 at all three sites (dashed line in Figures 3.17, 3.18 and 3.19); late December 2004 at the UTR site (Figure 3.17); mid-February 2005 and early October 2006 at the shelf and slope sites (Figures 3.18 and 3.19).

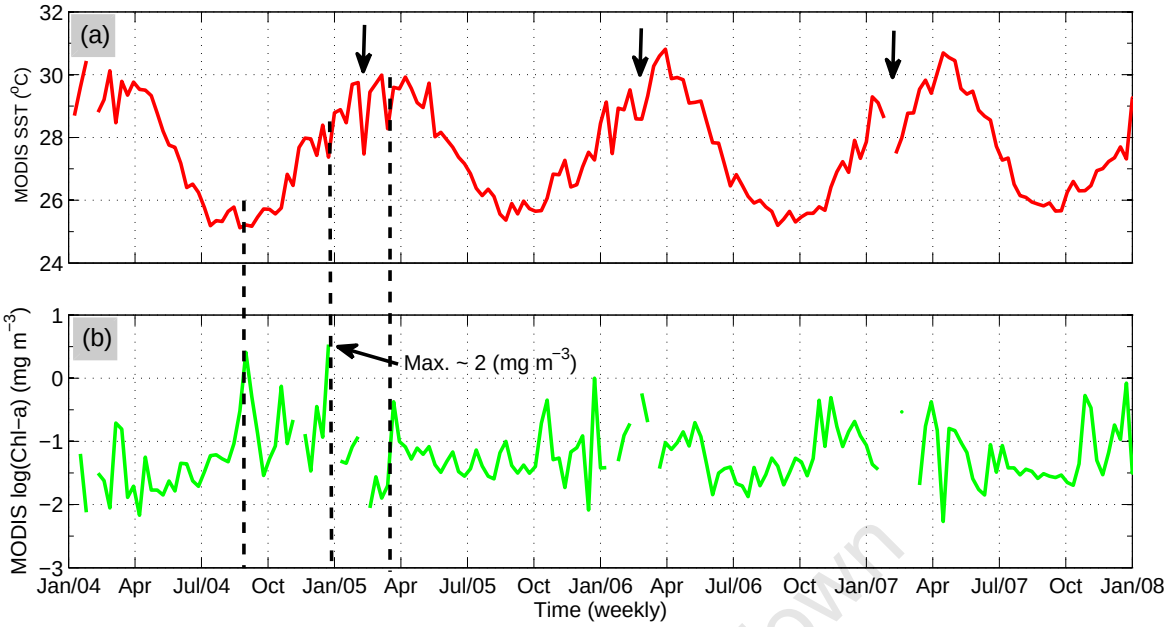

Figure 3.17: Time series of weekly (a) SST and (b) Chl-a derived from MODIS 1 km gridded data at the UTR site for the period January 2004 to December 2007. Arrows highlight cool water events ($> 2^{o}$C). Dashed line shows the relationship between cool water events and enhanced Chl-a.

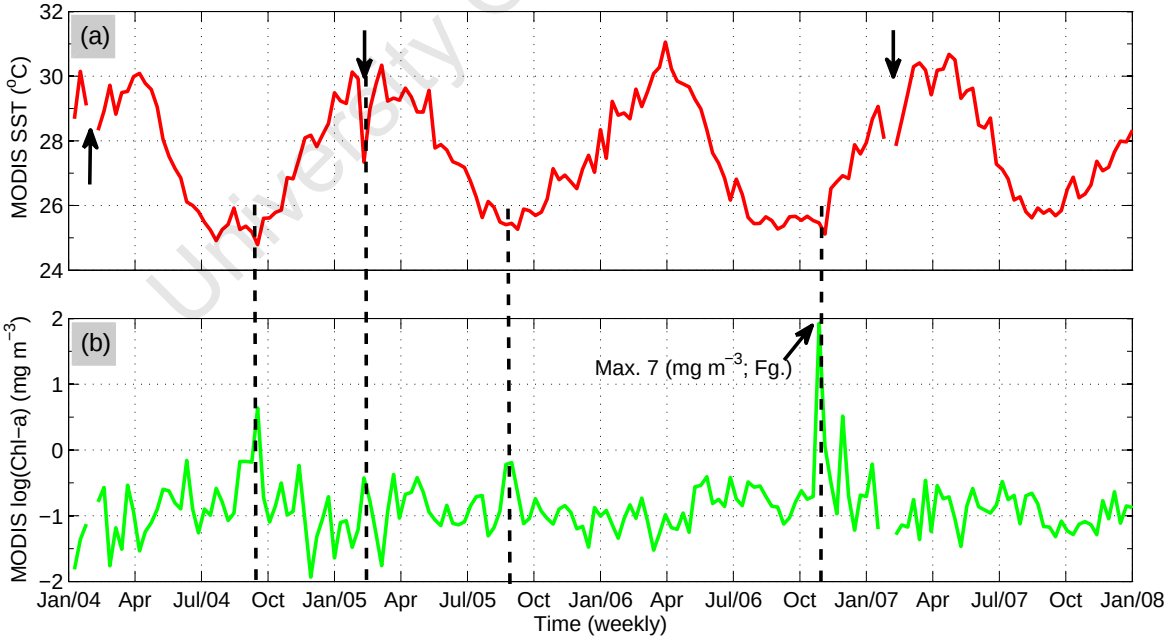

Figure 3.18: Time series of weekly (a) SST and (b) Chl-a derived from MODIS 1 km gridded data at the shelf site for the period January 2004 to December 2007. Arrows highlight cool water events ($> 2^{o}$C). Dashed line shows the relationship between cool water events and enhanced Chl-a.

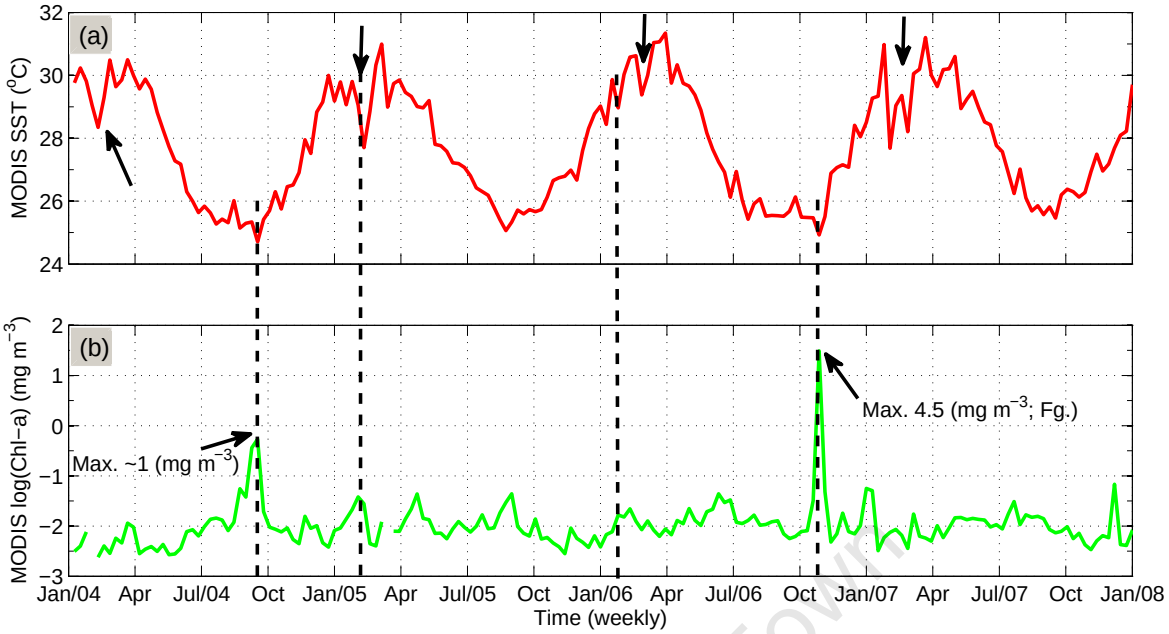

Figure 3.19: Time series of weekly (a) SST and (b) Chl-*a* derived from MODIS 1 km gridded data at the slope site for the period January 2004 to December 2007. Arrows highlight cool water events ($> 2^oC$). Dashed line shows the relationship between cool water events and enhanced Chl-*a*.

Time series for *in situ* UTR

Daily and weekly water temperatures measured at the UTR deployed at a depth of 18 m adjacent to Mozambique island for the period October 2002 to September 2007 are shown in Figure 3.20. The data are complete (i.e. no missing values) for the entire period of five years. A strong seasonal oscillation is evidents with a range of 4^oC between the maximum of 29^oC in March and 25^oC in September (Figure 3.20a).

Numerous (intermittent) cool water events are observed with amplitudes reaching $>4^oC$, almost equal to the amplitude of the seasonal oscillation. These can last as long as 16 days. At times the amplitude of these events can exceed the seasonal cycle. For example, the 7^oC temperature change in October 2003 and February 2006. The events in the summer of 2006/2007 had the lowest amplitudes for the time series and January 2003, October 2003 and February 2006 had the highest.

The large cool ($> 2^oC$) water events are still visible in the weekly time series (Figure 3.20b),

although, with reduced amplitude (Figure 3.20b). However the short period (< 8 days) and low amplitude cool events are no longer visible in the weekly data.

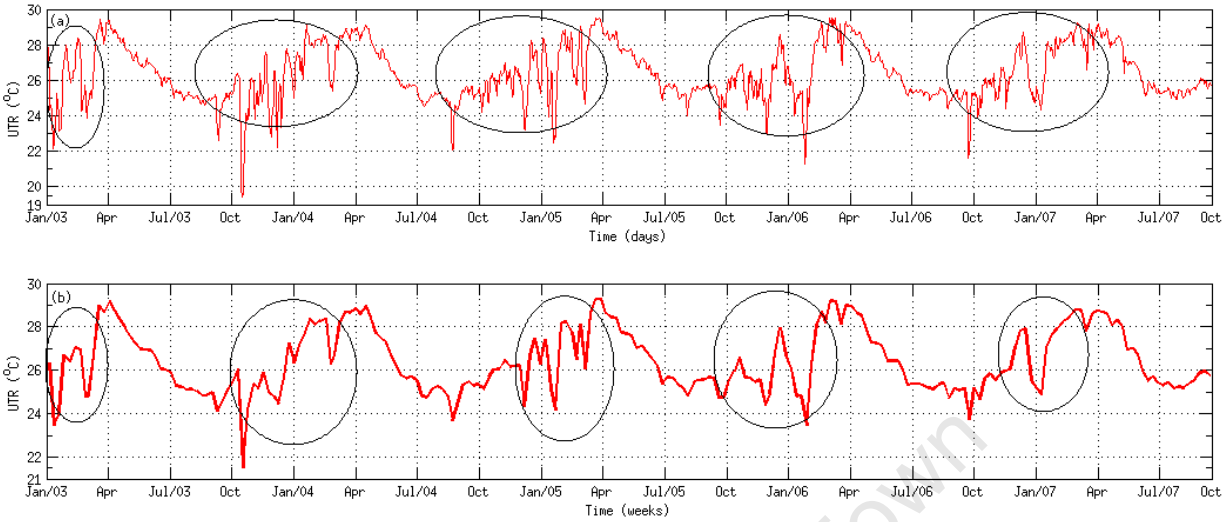

Figure 3.20: Time series of temperature (^{o}C) measured at the UTR (18 m) site adjacent to Mozambique Island for the period October 2003 to September 2007. (a) daily and (b) weekly averages. Circles show the period of cool (> 2^{o}C) water events.

Figure 3.21 shows the comparison between sea surface temperature derived from weekly MODIS 1 km gridded data at the UTR site and *in situ* weekly water temperature measured from the UTR at a depth of 18 m. The two data sets exhibit similar variability. The MODIS SST was warmer than the UTR, particularly in the summer peaks (Figure 3.21). For example in March 2004 the MODIS SST was 30^{o}C whereas the UTR temperature was 28.3^{o}C and in March 2007 the MODIS SST was 30.8^{o}C whereas the UTR temperature was 28.7^{o}C.

It appears that cool events identified in the MODIS SST data coincided with cool events in the UTR data set, For example, on 26 February 2004, 20 August 2004, 27 January 2005, 30 January 2006 and 17 January 2007 (vertical dashed line, Figure 3.21). The cool events in the MODIS SST data showed smaller amplitudes than the UTR data, for example, on 27 January 2005 2.5^{o}C (MODIS SST) versus 3.5^{o}C (UTR), 30 January 2006 1^{o}C (MODIS SST) versus 5^{o}C (UTR) and 17 January 2007 2^{o}C (MODIS SST) versus 3^{o}C (UTR).

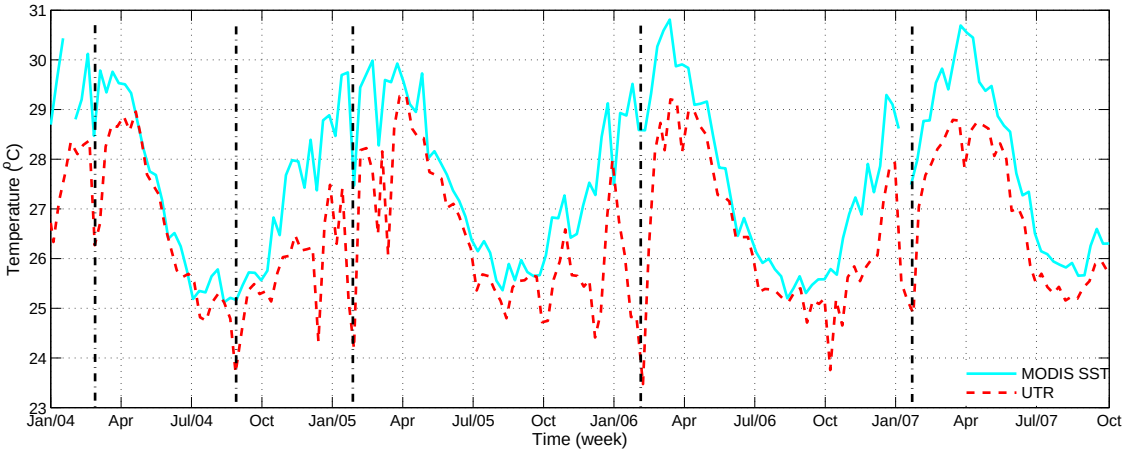

Figure 3.21: Time series of weekly averaged temperature derived from 1 km gridded MODIS (surface) data and measured at the UTR (18 m) site for the period January 2003 to December 2007. Vertical dashed lines show the relationship between cool events (>2^{o}C) for the MODIS SST and UTR data.

Wavelet power spectrum of *in situ* UTR

Figure 3.22b shows the wavelet power spectrum of the normalized temperature data (UTR time series) between October 2002 to September 2007 with the seasonal cycle removed (Figure 3.22a) using the Morlet mother wavelet (equation 3.2). When the seasonal cycle is removed from the original time series of the UTR data (Figure 3.22a), it becomes clear that the intraseasonal variability is dominated by cool water events (∼4) occurring between August and March every year.

The wavelet power spectrum (Figure 3.22a) shows high power (dark red) between October and March (austral spring-summer) every year and low power between March and July (winter months). Many significant cool water events of large amplitude (very red spectrum enclosed by white line) were observed in spring to summer of 2003, 2004 and 2006, with a low amplitude event in the summer of 2007.

The dominant significant period of cool water events was approximately 64 days (Figure 3.22b-c) observed every year except in 2005 which had slightly shorter periods (Figure 3.22b). The shorter significant period of 4−8 days in 2004 and 2006, 8−32 days in 2003, 16 days in 2004 and 2006 and 6−48 days in 2005 are also noticeable. A very long period of more than 60 days

was observed in 2004. There was also a significant very long period in 2003 but because this occurred within the cone of influence it was not considered further. There is some indication of periodicity of more than 128 days in 2006 but this was not significant at the 95% confidence level.

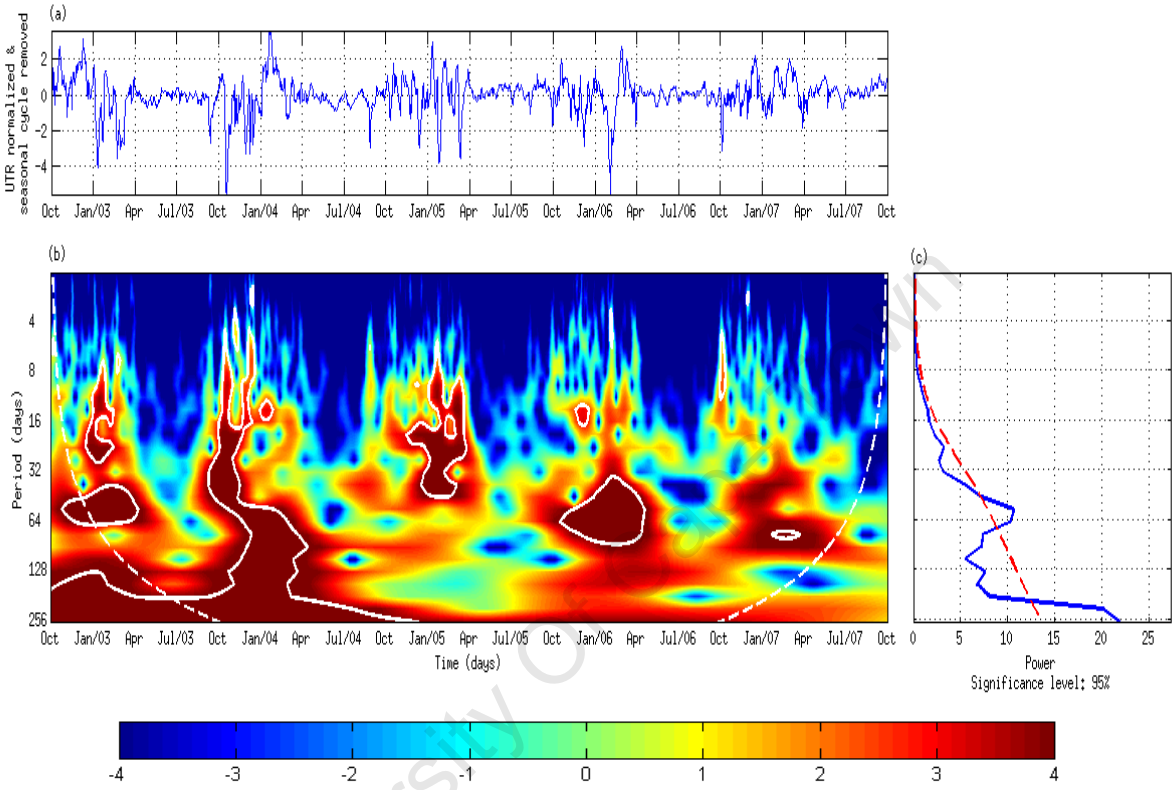

Figure 3.22: (a) time series of normalized daily temperature with the seasonal cycle removed for the period October 2002 to September 2007. (b) Morlet wavelet power spectrum. White solid line encloses the region with greater than 95% confidence level for red noise. White dashed line indicates the region where edge effects become important. (c) The global power spectrum. Red dashed line indicates the 95% significant level .

3.4 Discussion

Spatial variability of upwelling

The northern region of Mozambique is characterized by warm sea surface temperatures ($\sim 28^{o}$C) and very low surface chlorophyll-a concentrations (< 1 mg m^{-3}). Low levels of Chl-a were also noted by Omta et al. (2009) and Tew-Kai and Marsac (2009). In this study, apparent upwelling signatures were observed by enhanced Chl-a levels and lower SSTs along the coast, near Angoche roughly between 15 and 18^{o}S and the coast to 41^{o}E, from a combination of satellite MODIS data, *in situ* cruise survey CTD\XBT data, and *in situ* temperature mooring (UTR) data. This finding is consistent with knowledge of upwelling processes, winds and coastline orientation given in Chapter 2.

Five years (2003$-$2007) of daily MODIS SST and Chl-a 1 km grid data show the occasional appearance of slightly cooler water ($\sim 2^{o}$C in range) and slightly enhanced Chl-a (> 1.5 mg m^{-3}) events which, suggest the occurrence of upwelled water at the surface. Upwelling signatures were also reflected in the two cruise surveys undertaken by the ASCLME in December 2008 and August 2009. The horizontal plots at different depths (Figures 3.10-3.12) and vertical shore-normal transects (isotherms upliftment at the slope and doming, Figures 3.13-3.16) confirm the upwelling, and show clearly that upwelling is more prominent at depth. Cooler water becomes more evident below a depth of 20 m deeper. The maximum fluorescence was observed at a depth of 50 m with corresponding cool water.

The skewness of MODIS Chl-a in each single point within the study domain ($12-20^{o}$S and $35-45^{o}$E) was calculated for the period January 2003$-$August 2007 ($\sim$five-years). Two potential upwelling core regions were depicted in the map of skewness distribution by their anomalous positive skewness values (Figure 3.9b). One is the shelf core region (near the shore) between $15-16^{o}$S and the other is the continental slope core region centred at 17^{o}S and 40^{o}E. The slope core region location is consistent with a previous study describing a cyclonic eddy and associated upwelling in its core by Nehring et al. (1987), and subsequently, a study showing a cyclonic lee edge eddy by Ridderinkhof and de Ruijter (2003). The location of upwelling in the

shelf core region is shown here for the first time.

The two core regions identified in the satellite derived data were consistent with minimum temperatures and maximum fluorescence observed during the ASCLME cruise 2009. The ASCLME cruise 2008 only observed the shelf core region, possibly because this cruise only coincided with the early stage of upwelling. This particular upwelling event in December 2008 could not be tracked by satellite MODIS observations due to persistent cloud cover at this time of the cruise.

The total area for the shelf edge upwelling off the northern Mozambique coast was calculated to be approximately 68 000 km^2, with dimensions from north to south of ∼437 km and from west to east of ∼412 km. Caution needs to be exercised when in interpreting these values because this area was estimated in a GIS based composite image comprising the best daily MODIS SST and Chl-*a* images depicting upwelling. It should be noted that satellite observations, in particularly ocean colour, are not ideal for investigating upwelling in this region for the following reasons: (1) Some parts of the area might have observed upwelling signatures only once in the time series, but are included in the calculation as a standard area; (2) the region is strongly influenced by cloud cover (Tew-Kai and Marsac 2009), particularly during the period of upwelling, which coincides with the rainy season. This limits available data, which is not included in the calculation; (3) the upwelling has a weak manifestation at the surface, as shown by the cruise data and the comparison between the time series for MODIS SST and UTR (18 m) at the UTR site (Figure 3.21). The SST amplitudes of cool events at the surface were smaller than the *in situ* temperature amplitudes at 18 m, suggesting that upwelling is strongly sub-surface and not well defined at the surface making it difficult to distinguish upwelling events with satellites.

Temporal variability of upwelling

The skewness values at the slope core region (∼1.5) were larger than the shelf core region (∼1), implying that upwelling events are rarer at the slope core than in the shelf core region. Thompson and Demirov (2006) demonstrated that the skewness depends on the duration of the phenomenon at a location with a greater skewness value and shorter duration.

The MODIS SST and Chl-a fields show that most of the upwelling events started (new upwelling stage) at the coast between $15-16^oS$ where the shelf core region is located, and propagate (aged upwelling) southward to 17^oS and 40^oE. Sometimes however, the events did not reach this latitude (the slope region). The upwelling signatures were not prominent during the aged upwelling stage (Habeebrehman et al. 2008). These facts support the finding that upwelling is less frequent on the slope than the shelf core region.

All three sites exhibit similar scales of variability in sea surface temperature (Figure 3.17-3.19). At the UTR site the sea surface temperature is comparable with the water temperature at a depth of 18 m (Figure 3.21), but the 18 m measurement data captured the upwelling signature reasonably well. Furthermore, the UTR data are complete, i.e., no missing values. Therefore, the UTR time series is considered to best describe the temporal variability of upwelling near Angoche.

The time series reveal two distinct time periods corresponding to distinct seasons of upwelling every year (Figure 3.20). The downwelling season occurs between the austral winter and mid-autumn and is characterized by an absence of upwelling. The upwelling season between austral spring and summer (August−March) is characterized by intermittent upwelling events (cool water−enhanced Chl-a). Upwelling noticed by Nehring et al. (1987) near Angoche also occurred in this period. Observations by the two cruise surveys (ASCLME December 2008 and August 2009) were also coincident with this period. The occurrence of upwelling events between spring and summer is also visible by cool water events in the wavelet analysis (Figure 3.22). An average of four large cool water (amplitude $> 4^oC$) events were observed per year during the upwelling season in intraseasonal periods. The dominant period for the upwelling was about two months (~ 60 days), although short periods of one to four weeks ($8 - 30$ days) were also observed.

The MODIS SST and Chl-a fields revealed several sustained periods of upwelling. However, these events may not be real because the period between the events was generally short (1-5 days) and cloud lasting more than a week (i.e. between two events) may interpret these as a long single event.

Chapter 4

Driving mechanisms for upwelling off northern Mozambique

4.1 Introduction

The Mozambique Channel is a very complex marine system, encompassing strong mesoscale eddy variability with southward net volume transport (Sætre and da Silva 1982, 1984; de Ruijter et al. 2002; Ridderinkhof and de Ruijter 2003; Schouten et al. 2003; Lutjeharms 2006). Nehring et al. (1987) attributed the Angoche coastal cyclonic lee eddy and associated upwelling to the southward passage of a strong continuous Mozambique Current flow. Today it is well known that continuous flow in the Mozambique Channel does not exist but there is rather an intermittent meandering current. Subsequently, Lutjeharms (2006) suggested that the cyclonic lee eddy was induced by the passage of strong anti-cyclonic eddies.

The northern region of Mozambique is influenced by monsoon seasons with winds that blow from the NE during the austral spring and summer months and from the SW during the winter (Sætre and da Silva 1982). The upwelling noticed by Nehring et al. (1987) and the cyclonic eddy observed by Ridderinkhof and de Ruijter (2003) coincided with northeast monsoon wind season. Whether the monsoon contributes to upwelling in northern Mozambique is not known.

There are no studies about the driving mechanisms for upwelling in northern Mozambique.

Hence, there is a lack of knowledge about this upwelling. In chapter 3, the variability of the shelf edge upwelling of the northern Mozambique was investigated. In this chapter the findings of Chapter 3 are used to assess the possible driving mechanisms of the northern Mozambique shelf edge upwelling. In particular, the role of the sea surface wind field and eddies will be investigated. The study domain, the subdomain, and the period of the study are the same as in Chapter 3. This Chapter addresses three key questions (questions 5, 6 and 7 as first raised in chapter 1):

- What are favourable wind conditions for upwelling in northern Mozambique? Are these related to the monsoon seasons?
- Is the periodicity of upwelling events related to the passage of eddies?
- Is upwelling in northern Mozambique always associated with a cyclonic eddy or can it occur independently?

4.2 Data and methods

Multiple satellite blended sea surface wind data

Sea surface wind traditionally has been measured from *in situ* meteorological stations (coastal, ships and buoys). These traditional, often single location, *in situ* observations provide very limited spatial coverage of the ocean surface and this leads us to explore alternative ways to observe sea surface wind with wide spatial coverage. Wind blowing over the ocean surface creates ripples and small amplitude waves on the ocean surface. This surface roughness is highly correlated with the surface wind speed and direction. Using this feature, sea surface wind has been operationally observed from satellite scatterometer instruments since the 1980s (Zhang et al. 2006b,a). Today a range of satellite scatterometers (Table 4.1) processed by Remote Sensing Systems Inc. (RSS) are used to observe the world ocean's sea surface wind speed and direction for a range of atmospheric and oceanic applications. *In situ* observations still play a fundamental role in calibrating and validating these satellite data.

Satellite scatterometers are active microwave radars operating at a Ku-band (13.4 GHz) frequency, which transmits pulses to the ocean surface and measures the electromagnetic power backscattered to the instrument from the wind roughened ocean surface. These satellites are often placed at a low altitude ($\sim$ 800 km), circular polar-orbit and cross the equator at the same locale twice each day (table 4.1) on an ascending (from south to north) and a descending (from north to south) overpass (Zhang et al. 2006b,a). The instruments sweep a circular pattern with a trace of approximately 1800 km width on the ocean, twice a day in the ascending and descending overpasses. For example, QuikScat uses a dish antenna rotating at 18 rpm with dual polarized spot beams at two fixed incidence angles, at 46^o for the horizontal beam and at 54.1^o for the vertical beam (source `http://www.remss.com/`, last visited March 2010).

Table 4.1: Equatorial crossing time in Local Solar Time of January 2005 (adapted from `http://www.remss.com/` and Zhang et al. 2006a)

Satellite/Instrument	Ascending	Descending	Observations
Advanced Microwave Scanning Radiometer - Earth Observation System (AMSR-E)	13:30	01:30	not operational since Nov 2009
Spatial Sensor Microwave Image (SSMI) F15	21:05	09:05	
Quick Scatterometer (QuikSCAT)	05:54	17:54	not operational since Nov 2009
Tropical Microwave Image (TMI)	15:54	03:54	
Spatial Sensor Microwave Image (SSMI) F14	19:08	07:08	
Spatial Sensor Microwave Image (SSMI) F13	18:33	06:33	

This study used high resolution gridded and blended data for sea surface wind speed (W, m s^{-1}) and wind velocity vectors (U, zonal (m s^{-1}) and V, meridional (m s^{-1})) derived from multiple (six) satellite observations at a reference height of 10 meters above the sea surface. Level 3 data products are obtained on a daily time resolution and global ocean cover at 0.25^o spatial resolution (720 bytes latitude x 1440 bytes longitude). Data were retrieved for the study domain ($12-20^o$S and $35-45^o$E, 32 latitude x 40 longitude pixels) for the period January 2003 to September 2007 (five years). Data were supplied in NetCDF format by the Marine Remote Sensing Unit at the University of Cape Town. Data are distributed by NOAA/NCDC and are available as bytemaps from the website: `http://www.ncdc.noaa.gov/oa/rsad/seawinds.html`, last visited March 2010.

The blended products are the best to use because of the increase in the temporal and spatial

resolution of the individual satellite products obtained by filling in the gaps, and reducing the sub-sampling and random errors. These blended wind products were produced using both ascending and descending 0.25^o grid continuous data observations from the multiple satellites (Table 4.1). Wind direction comes from NCEP Reanalysis-2. For the blending process, 12-hourly gridded and blended products are generated for standard 0.25^o grid resolution using an Objective Analysis (OA) method, i.e. a spatio (62.5 km)-temporally (6 hours) weighted interpolation (Zhang et al. 2006b,a). This interpolation weight function has a normal distribution. A gap-free 12-hourly global product is produced by filling in the few remaining gaps of the 12-hourly products with more recursive weighted interpolations in space from 60^oS to 60^oN, using nearest blended data points. The daily products were produced by averaging the two 12-hourly products for each day (Zhang et al. 2006b,a). Data close ($\sim$ 25 km) to the coast are also available. No "data cleaning" has been done over land along the coast ($\sim 0.25^o$) (read me file available at website: `http://www.ncdc.noaa.gov/oa/rsad/seawinds.html`, last visited March 2010). Scatterometer data are affected by rain. Satellite microwave radiometer measurements are used to flag rain occurring at the location of the observations in such a way that the data are reliable (source `http://www.remss.com/`, last visited March 2010).

Wind directions follow the oceanographic convention, for example, winds blowing towards the North have direction 0 or 360^o. Positive U values indicate that the wind is blowing towards the east and negative U indicates wind blowing westward (landward). Positive V values indicate wind blowing towards the north and negative V indicates wind blowing southward (poleward) (source`http://www.remss.com/`, last visited March 2010).

Blended sea surface wind data processing and presentation

Daily blended sea surface wind speed and velocity vector fields were extracted for the whole study domain from the original daily global 0.25^o grid blended data set between 2003$-$2007. Horizontal maps for daily blended sea surface wind speed (color shading) and wind velocity vectors (arrows) were produced for the whole domain using *Matlab* software.

Time series data of blended sea surface wind speed (m s^{-1}) and zonal (U) and meridional (V) wind velocity vectors (m s^{-1}) were extracted for all three selected areas (Figure 4.1, as first

raised in Chapter 3) within the domain: the UTR site (1 latitude x 1 longitude pixels); the shelf site (4 latitude x 2 longitude pixels); and the slope site (3 latitude x 3 longitude pixels) for the period 2003−2007 (five years). For the shelf and slope areas each day of the time series consists of wind data spatially averaged over all valid pixels lying inside the area. Because of computer limitations (low memory capacity to deal with large data sets) the original five year data set for each selected area was split into months (60 subsets of data), then recombined as a unique data-set for the entire period.

The U and V wind velocity vectors data were used to produce time series of wind direction and speed vector displayed as a feather plot for all three sites.

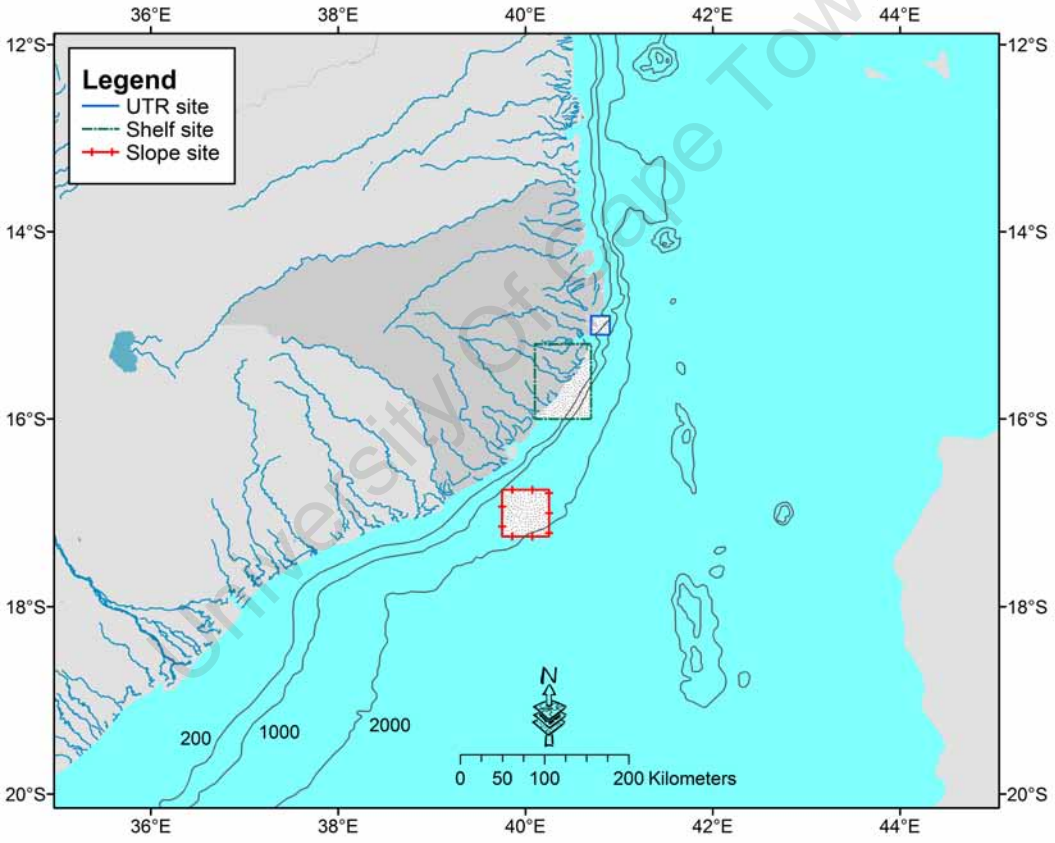

Figure 4.1: The study area showing the sub-domains: the UTR site (blue); the shelf site (green) and the slope site (red).

Multi-satellite altimetry data

Satellite altimetry data has been increasingly used for estimating ocean circulation and its variability in the world's oceans since the first satellite launched in late 1970s. For example,

in the Mozambique Channel altimetry data have been used to observe flow (de Ruijter et al. 2002), to observe eddy variability (Schouten et al. 2003), to comprehend the foraging strategies of a tropical top predator (Weimerskirch et al. 2004) and to calibrate/validate models (Halo 2008; Backeberg et al. 2009).

Satellite altimeters are essentially down-looking radars which determine the range from the satellite to the target ocean surface. An altimeter operates by continually transmitting short radar pulses ($>$ 1700 per second) down to the Earth's surface and measuring the return time of the echo that is backscattered to the satellite from the sea surface at high accuracy by averaging the measurements over a second (AVISO/Altimetry 1996, 2005). The altitude, period, inclination and repeat cycle of the satellite orbit are some of the parameters which play a fundamental role in satellite altimetry. For example, TOPEX/Poseidon was launched at an orbital altitude of 1330 km, at a fixed incidence angle of 66^{o}S to the polar axis of the Earth (not sun-synchoronous) and over-flew the same position (repeat cycle) every ten days at 7.2 km s^{-1} (AVISO/Altimetry 1996). Jason-1 also had a repeat cycle of ten days in a similar, but parallel orbit, obtaining data beginning at latitude 66^o S and ending at 66^{o}N (ascending overpass) (AVISO/Altimetry 2005).

Radar altimeters on board satellites operate at several different frequency bands. The most used band is the Ku-band (13.6 GHz) frequency, which is sensitive to atmospheric changes and the presence of ionospheric electrons. The C-band (5.3 GHz) is better than the Ku-band for ionospheric perturbation, and is used in combination with the Ku-band (Dual-frequency Ku-/C-band) for ionospheric delay corrections and to estimate rain rates (AVISO/Altimetry 1996). The S-band (3.2 GHz) is also used in combination with the Ku-band for ionospheric delay corrections and the Ka-band (35 GHz) is used for observations over ice, land masses and coastal zones and for improving resolution near the coast (however, there are no AVISO data products very close to the coast) (source AVISO web site `http://www.aviso.oceanobs.com`, last visited March 2010).

This study uses homogeneous altimetry data combined from a multi-satellite altimeter mission: TOPEX/Poseidon, Jason-1, GFO, ERS-1, ERS-2 and ENVISAT. These merged data were generated by the Data Unification and Altimeter Combination System (DUACS), part of the

Centre National d'Etudes Spatiales (CNES) multi-mission ground segment SSALTO, using two distinct cross-calibration algorithms: a global multi-mission crossover minimization for orbit error reduction (OER), and Optimal Interpolation (OI) for Long Wavelength Errors (LWE) (AVISO/Altimetry 2009). Satellite altimeters are affected by rain (no AVISO data products when the rain is > 1.5 mm h^{-1}) and are also influenced by the ocean sea state, tides and atmospheric pressure. Data for use in determining ocean circulation are distributed by AVISO and are available in NetCDF format at `http://www.aviso.oceanobs.com`.

A data set consisting of sea level anomalies (SLA, cm) and geostrophic velocity vectors (U and V, cm s^{-1}) was selected for the study domain from a global $1/3^o$ Mercator projection Level 2 data product (merged, homogeneous, atmospherically and geophysically corrected, and validated for quality). SSALTO/DUACS data were retrieved in two components: Delayed Time (DT) reference (ref) product (historically homogeneous data set) provided a weekly composite basis for the period 2002−2007 (five year time series) and Near Real Time (NRT) product provided daily data for the period December 2008 (during the ASCLME cruise 2008) and 10−16 August 2009 (during the ASCLME cruise 2009).

Altimetry data processing and presentation

The merged daily NRT and weekly DT ref data products for sea level anomaly and geostrophic velocities (U and V) from 2003−2007 were used to produce horizontal maps of sea level anomaly (cm) and geostrophic velocity vectors (cm s^{-1}) for the study area using *Matlab* software.

Time series data of sea level anomaly were extracted from the original weekly DT ref data set for the period 2003−2007 in all three selected areas: the UTR site area (1 latitude x 1 longitude pixels); the shelf site (4 latitude x 2 longitude pixels); and the slope site (3 latitude x 3 longitude pixels). For the shelf and slope areas each time of the time series constituted a spatial average of all valid pixels lying inside the area. A five year time series of weekly SLA was produced for each of those three areas for the period in study.

Time series analysis

A wavelet model developed by Torrence and Compo (1998) (described in chapter 3), using a Morlet wavelet as the mother wavelet, is used here to investigate variability in the time series of blended sea surface wind speed for the UTR, shelf and slope sites. The input parameters are as in table 4.2.

Table 4.2: Input variables/parameters for the Torrence and Compo (1998) wavelet model for blended wind speed.

Variables/parameters	Symbol	Units	Value	Comment
Sampling time	δt	days	1	constant for time series
Plotting time	N	days	1460	4-years period from 2003 - 2006
Pad	Pad		1	add zeros on the edge of time series
Spacing scales	δj		0.25	smaller values take computer time
Smallest scale	s_0	day	2	highest detectable frequency resolvable for any variability
Significance level	α		0.95	

This wavelet model was not applied to wind velocities, SLA and geostrophic velocities because this model normalizes the input variables (by subtracting the mean and dividing by the standard deviation), making the mean zero. For these variables, this zero is artificial and confounds the interpretation. For example, negative and positive SLA values no longer always mean anti-cyclonic and cyclonic eddies, and positive U and V values no longer mean northward and eastward wind and/or geostrophic current directions.

Sea surface wind direction and temperature anomaly, and also sea level anomaly and temperature anomaly are expected to be related because of upwelling. The time series of UTR and blended sea surface wind velocity vectors (feather plot) at the UTR site for the period January 2003−August 2007 are examined together and also UTR and SLA. This approach was taken to examine whether there is a consistent relationship between various parts or all of these time series. (The UTR data set was described in detail in Chapter 3.)

4.3 Results

Spatial distribution of blended sea surface wind field

The five years (2003−2007) time series of daily gridded and blended sea surface wind speed and velocity vectors shows that wind fields in the Angoche region fluctuate in both speed and direction. Examples of snapshots for parts of this time series are given in Figure4.2a−e. Figure 4.2g and h were depicted because they correspond with two recent cruise surveys, ASCLME 2008 and 2009, respectively. Two basic distinct wind regimes are noteworthy: wind blowing to the north-east (a south-westerly−SW wind), which prevails during austral autumn−mid winter (Figure 4.2a, c and e), and the wind blowing to the south-west (a north-easterly−NE wind), which dominates between austral spring−summer (Figure 4.2b, d, and f). Note the austral season is defined here as: summer for January−March, autumn for April−June, winter for July−September and spring for October−December.

Both wind regimes exhibit strong winds on the west side of the Mozambique Channel, with the SW wind regime (Figure 4.2a, c and e) strong to the north of 16^{o}S (although on 05 June 2006 they were strong along the whole west coast to the north of 16^{o}S, Figure 4.2g) and the NE wind regime generally strong to the south of 16^{o}S (Figure 4.2b, d, f and h). The regions south of 18^{o}S are influenced by the SE trade winds. The SW and NE winds sometimes do not extend to 20^{o}S, shifting to become more westward (Figure 4.2d and g). East of 42^{o}E (off the coast of Madagascar) the zonal component of the wind velocities becomes weak−shifting to more southward (Figure 4.2b, f and g) or northward (Figure 4.2c).

Importantly, the NE wind propagating poleward alongshore, parallel to the coast of Angoche with offshore Ekman transport is the upwelling favourable wind (for example Figure 4.2b, d, f, g and h). For example, on 04 September 2004 (Figure 4.2d) the NE winds corresponded with an upwelling event (enhanced Chl-a−Figure 3.4 and cool water−Figure 3.5) between 15 August and 23 September 2004. In another example, NE winds on 4 October 2006 (Figure 4.2h) corresponded with the highest enhanced Chl-a event observed during the study period, from 6 to 8 October 2006 (Figure 3.8).

The two recent ASCLME cruises in December 2008 and in August 2009 coincided with the NE wind season (Figure 4.2g and h, respectively). On 5 December 2008 NE winds were observed alongshore off the Angoche coast between 15−17^{o}S whereas to the south of 18^{o}S easterly winds are found (Figure 4.2g). Figure 4.2h for 13 August 2009 exhibits a NE wind along the whole northern coast of Mozambique, which was strong to the south of 16^{o}S and weak to the north.

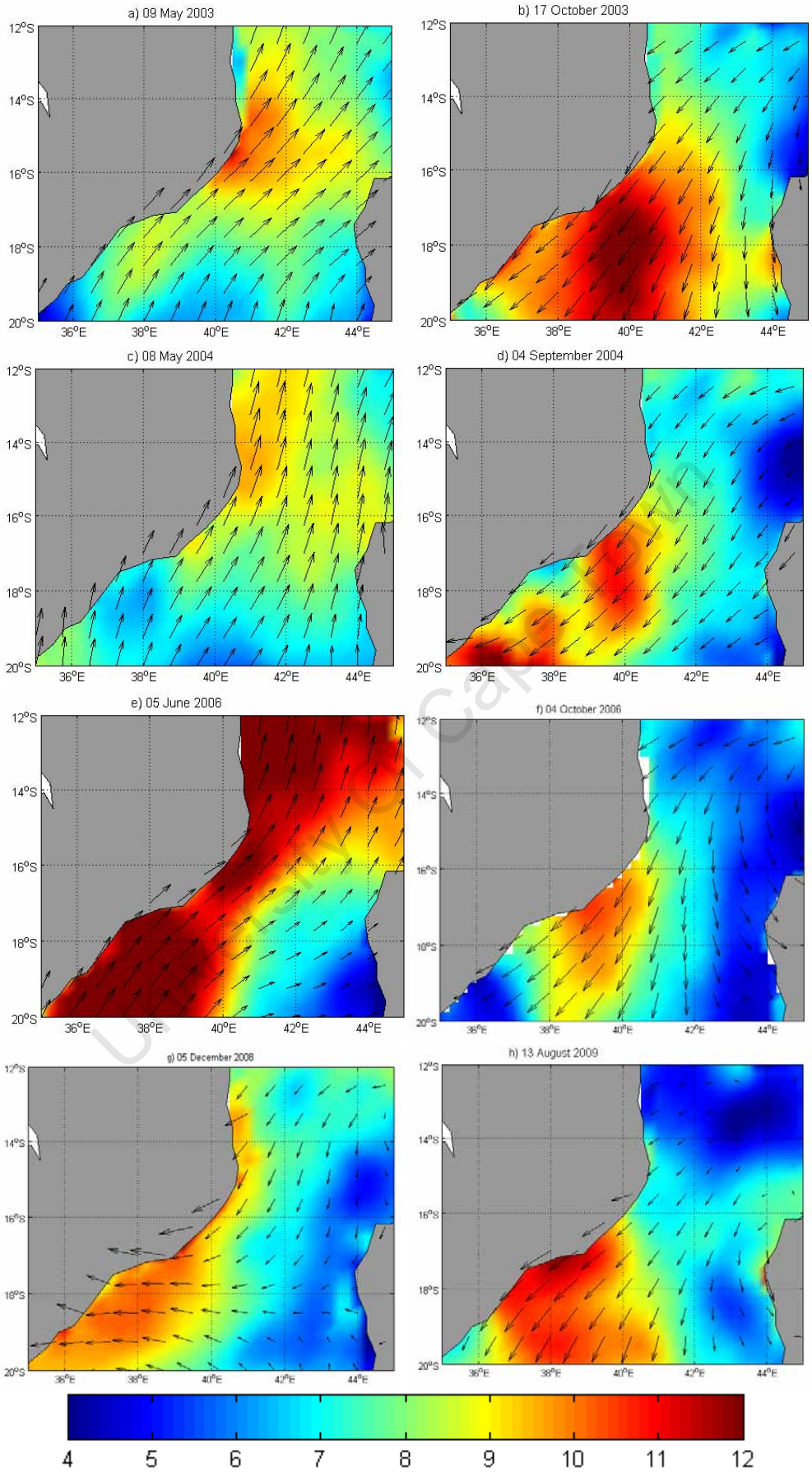

Figure 4.2: Examples of daily blended sea surface wind speed (m s^{-1}) and velocity vectors (m s^{-1}) derived from multi-satellite 0.25^o grid data product for the S wind regime (a) 09 May 2003, (c) 08 May 2004, and (e) 05 June 2006, and for the N wind regime (b) 17 October 2003, (d) 04 September 2004, and (f) 04 October 2006. (g) 05 December 2008 during the 2008 cruise and (h) 13 August 2009 during 2009 cruise.

Time series of blended sea surface wind

Examination of the whole five year time series for the three selected sites of daily blended sea surface wind speed and velocity vectors (Figures 4.3, 4.4 and 4.5) indicates that the winds are rarely steady, oscillating in speed and direction. Note that wind direction in Figures 4.3−4.7 is not truly represented. The function *axes equal* in *matlab*, which gives the same scale for both x and y axis and thus the correct direction, cannot be performed successfully with a long time series.

Wind velocity vectors (Figures 4.3a, 4.4a and 4.5a) exhibit a strong seasonal oscillation between south−westerly (SW) and the north-easterly (NE) wind direction at the three selected areas (an example of wind fields is depicted in Figure 4.2). Persistent SW winds dominate between April−July (austral autumn−winter). The NE winds dominate between August−March (spring−summer), however, occasional fluctuations in wind direction are observed in this regime. No interannual variability was observed in wind direction but the period of observation (∼five-year) is short.

Sea surface wind shows high variability in speed in intraseasonal periods (Figure 4.3b, 4.4b and 4.5b). The corresponding 30 day running means smooth some of the short period variability (Figure 4.3b, 4.4b, and 4.5b). The Morlet wavelet of the normalized daily blended sea surface wind speed (Figure 4.3c and d, 4.4c and d, and 4.5c and d) shows significant highest power between 2 and 16 day periods representing short periods of wind acceleration and deceleration, which was consistent over the whole time series. The amplitudes of the short period oscillations vary a lot over the time series with an average range of 2−8 m s^{-1} at all three selected sites.

Sea surface wind speed shows a seasonal oscillation, particularly at the UTR and shelf sites (Figure 4.3b and 4.4b). The amplitude range was short ∼5 m s^{-1} with high speed (∼10 m s^{-1}) during the austral autumn-winter corresponding with the SW wind regime whereas low speed (∼5 m s^{-1}) during the spring−summer corresponded to the NE wind regime. Fast wind speeds of over 20 m s^{-1} were observed. For example, in late January 2004 at the shelf (Figure 4.4 b) and slope (Figure 4.5b) sites, and also on April 2007 at the UTR (Figure 4.3a and b) and shelf (Figure 4.4a and b) sites.

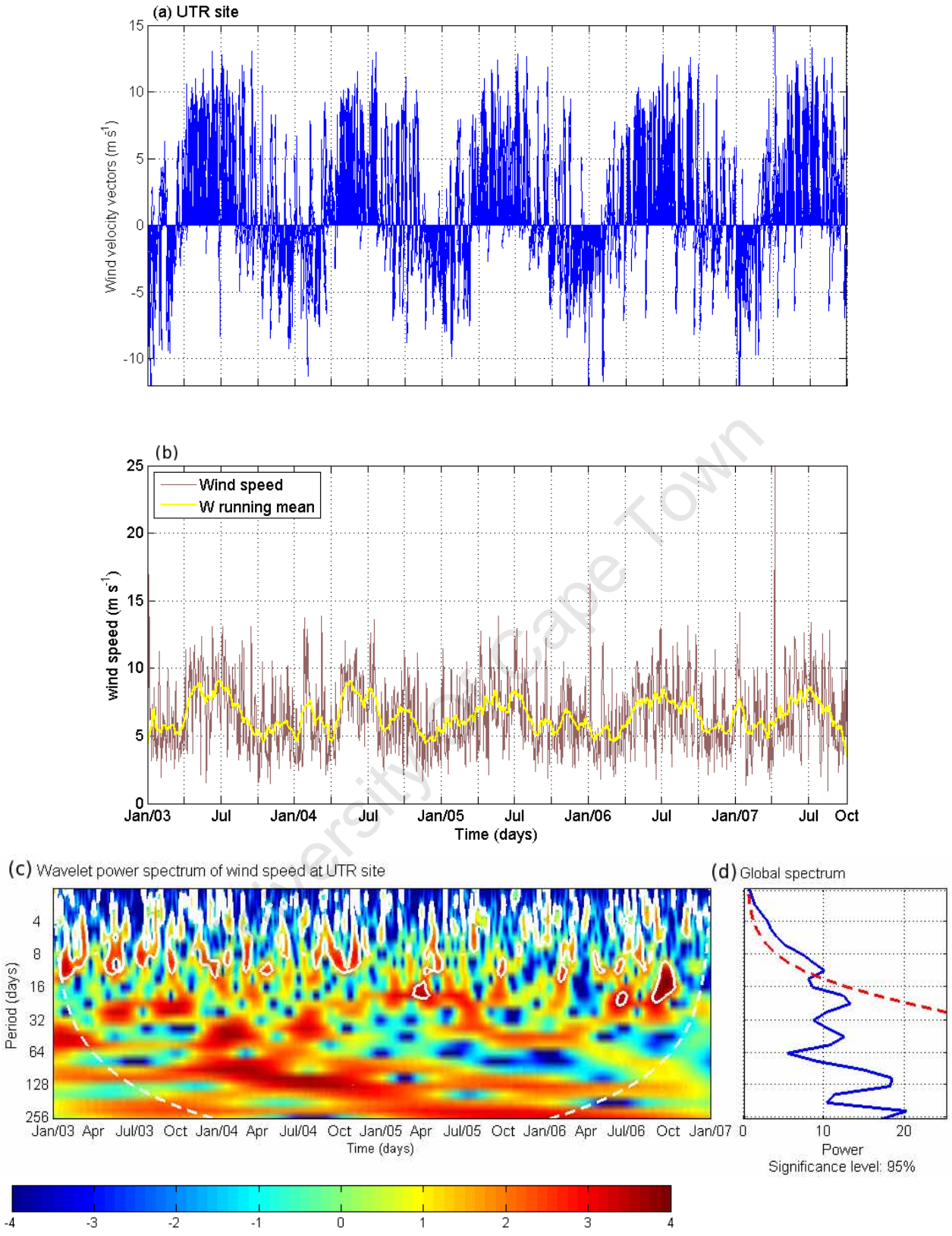

Figure 4.3: Time series of daily blended sea surface wind (a) velocity vectors (m s^{-1}) and (b) speeds (m s^{-1}) with the corresponding 30 day running mean (wide line) derived from multi-satellite observation (NOAA/NCDC) global 0.25^o grid data product over the UTR site for the period January 2003 to September 2007. (c) Morlet wavelet power spectrum for normalized daily blended wind speed (m s^{-1}) for the period January 2003 to December 2006 at UTR and (d) the corresponding global power spectrum. White and red dashed line indicate the 95% significant level.

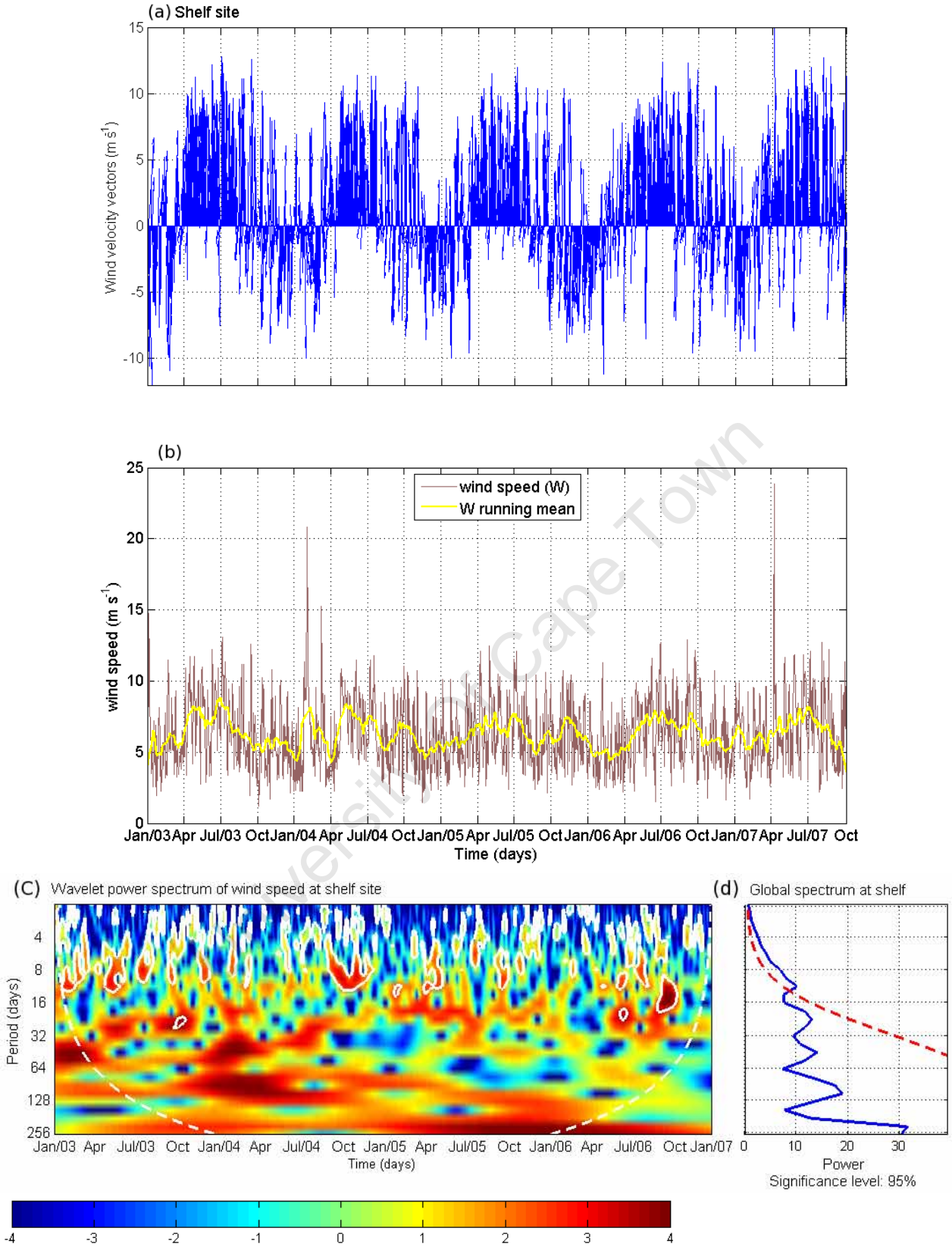

Figure 4.4: Time series of daily blended sea surface wind (a) velocity vectors (m s^{-1}) and (b) speeds (m s^{-1}) with the corresponding 30 day running mean (wide line) derived from multi-satellite observation (NOAA/NCDC) global 0.25^o grid data product over the shelf site for the period January 2003 to September 2007. (c) Morlet wavelet power spectrum for normalized daily wind speed (m s^{-1}) for the period January 2003 to December 2006 at shelf and (d) the corresponding global power spectrum. White and red dashed line indicate the 95% significant level.

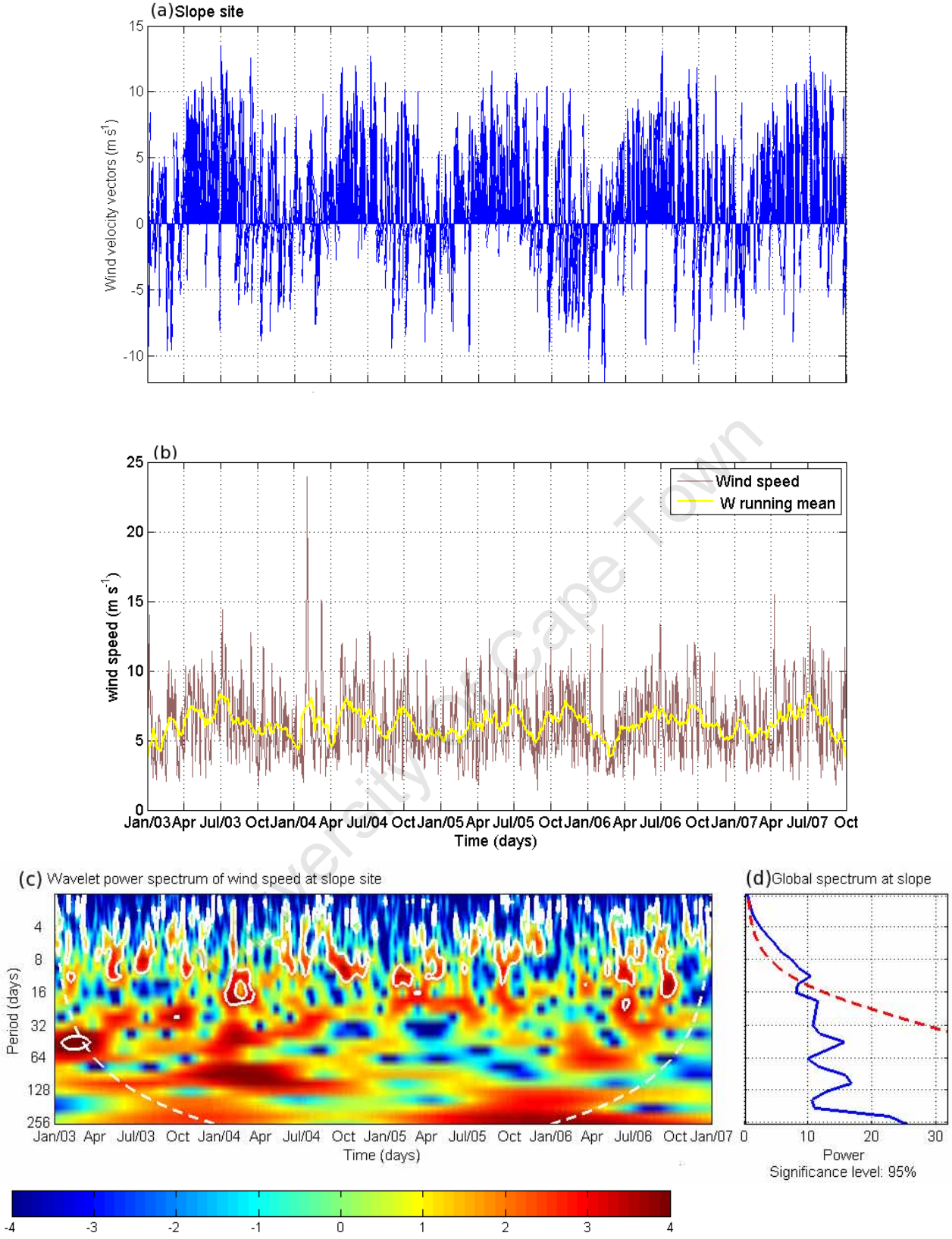

Figure 4.5: Time series of daily blended sea surface wind (a) velocity vectors (m s^{-1}) and (b) speeds (m s^{-1}) with the corresponding 30 day running mean (wide line) derived from multi-satellite observation (NOAA/NCDC) global 0.25^o grid data product over the slope site for the period January 2003 to September 2007. (c) Morlet wavelet power spectrum for normalized daily wind speed (m s^{-1}) for the period January 2003 to December 2006 at slope and (d) the corresponding global power spectrum. White and red dashed line indicate the 95% significant level.

Comparison of time series for blended sea surface wind and UTR

The time series of daily temperature anomaly (by subtracting the mean) measured at a depth of 18 m with the underwater temperature recorder (UTR) at the UTR site for the period January 2003 to September 2007 was compared with time series of daily blended sea surface wind velocity vectors at the UTR site (Figure 4.6 and 4.7). Figure 4.6 and 4.7 exhibit coherent variations between the cool water events ($>2^oC$ decrease) and the NE winds (between August−March). There were no cool water events during the SW wind regime (April−July). This variation is consistent for the whole time series (Figure 4.6a). There was no situation where a cool water event was observed without a NE wind. There were situations where NE winds were present but no cool water event was observed: for example, on 06 September 2004 (E on Figure 4.7d).

The relationship between the magnitude of the wind velocity vectors and the magnitude of cool water events is not very strong (Figure 4.6 and 4.7). For example, on 19 October 2003 a cool event of -5^{o}C of amplitude was observed in response to a NE wind with -7 m s^{-1} (A in Figure 4.7a) whereas on 08 November 2003 a cool event of 2^{o}C of amplitude range was observed in response to a -7 m s^{-1} NE wind (B, Figure 4.7a). Note the second cool water event had smaller amplitude but it was induced by a stronger NE wind (B, Figure 4.6b). Another example was observed on 27 August 2004 when a cool (3^{o}C of amplitude) event was observed in response to wind vectors with -3 m s^{-1} (C, Figure 4.7a) whereas on 08 October 2004 a cool ($<$ 2^{o}C of amplitude) water event was observed in response to wind vectors with U=-5 m s^{-1}and V=-9 m s^{-1} (D, Figure 4.7a). Again the strong wind induced the short amplitude cool water event.

Figures 4.6 and 4.7 also show that there were time lags of about 2 days between the NE wind and the surface cool water responses. For example, the cool water (peak) on 19 October 2003 occurred after a NE wind on 17 October 2003 (A, Figure 4.7a) and the cool water event observed on 27 August 2004 occurred after a NE wind on 25 August 2004 (C, Figure 4.7b).

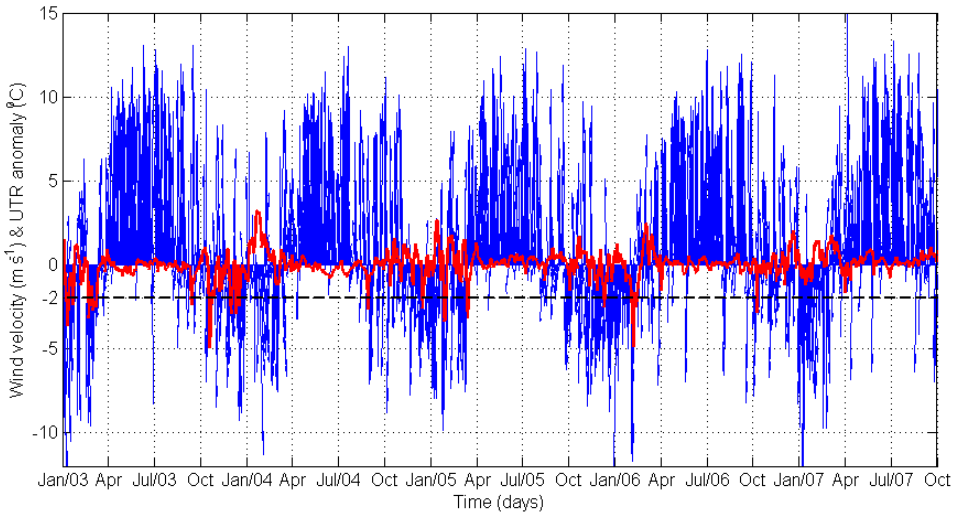

(a)

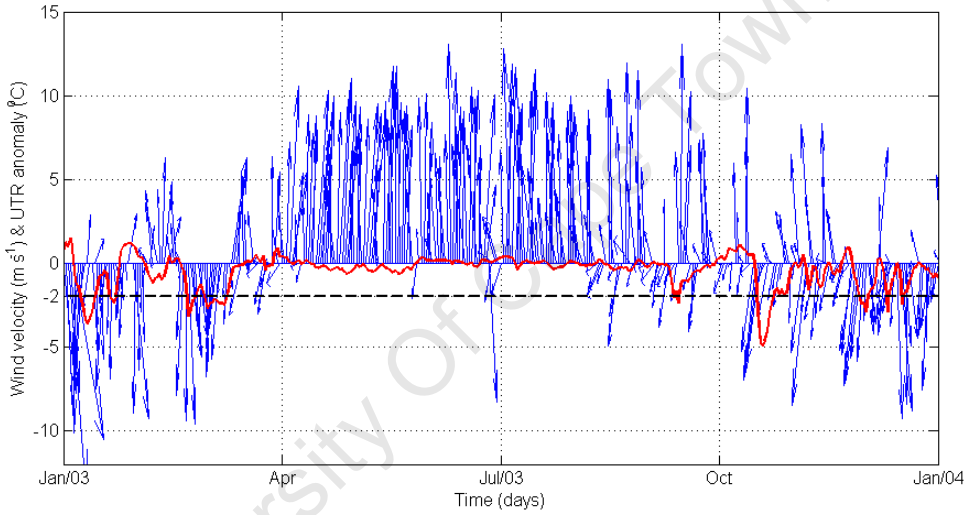

(b)

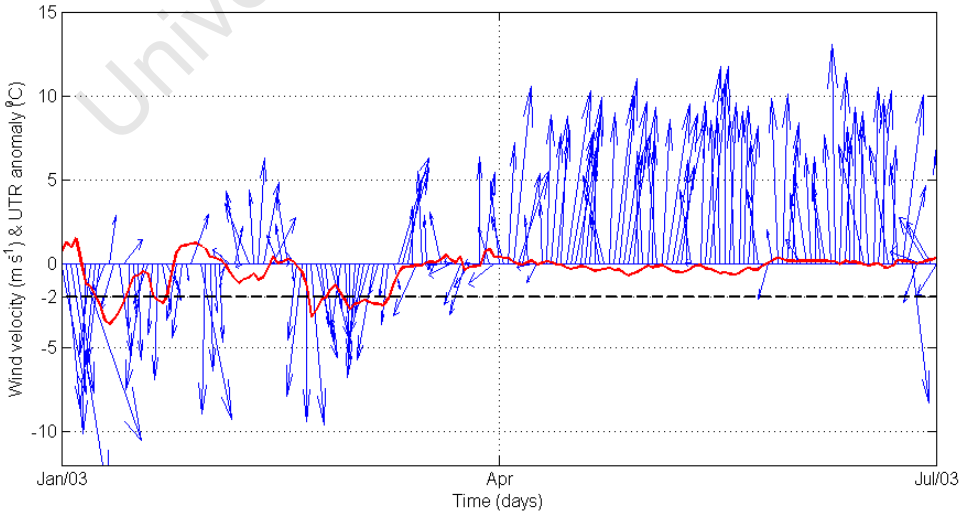

(c)

Figure 4.6: Time series for daily UTR anomaly (^{o}C; wide red solid line) measured at 18 m depth and daily blended wind velocity vectors (m s^{-1}) extracted at the UTR site for the period (a) of whole time series January 2003−September 2007, (b) year 2003 and (c) January−June 2003. Horizontal dashed line corresponds with UTR anomaly of -2^oC.

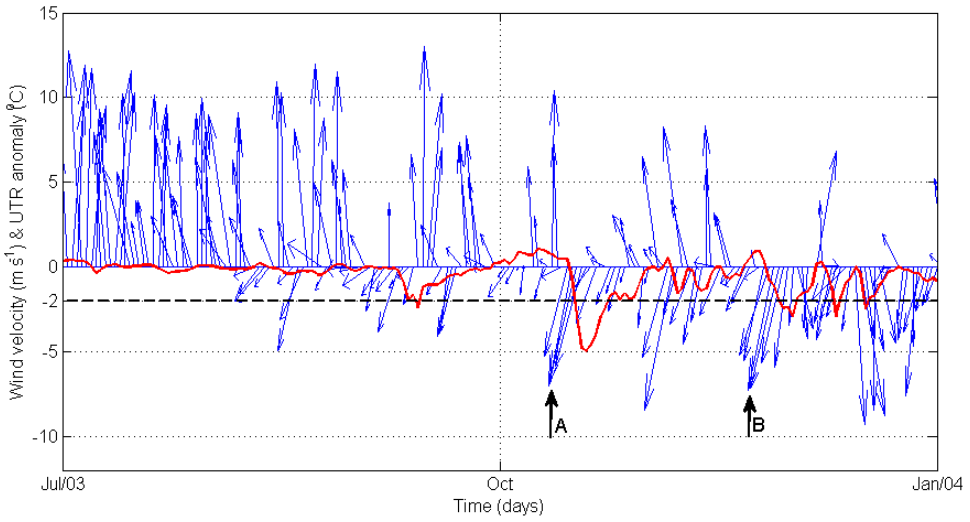

(a)

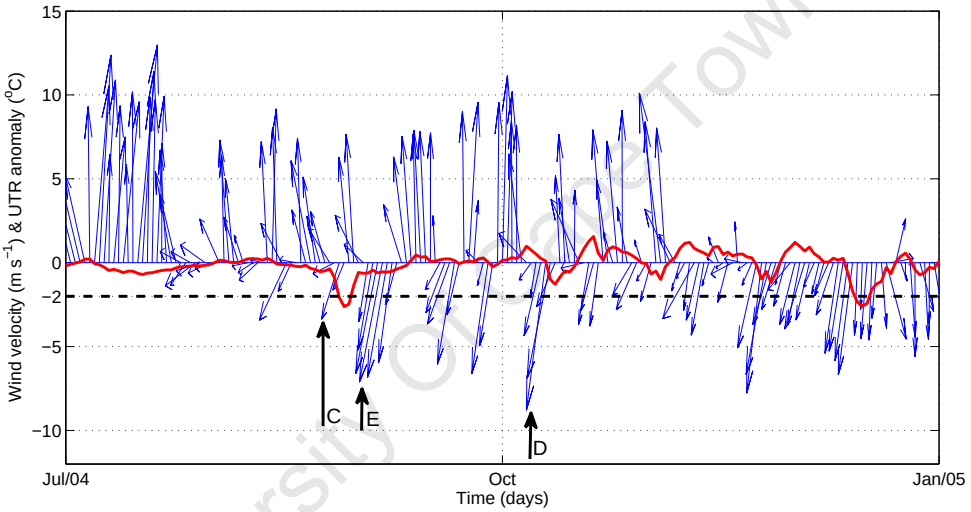

(b)

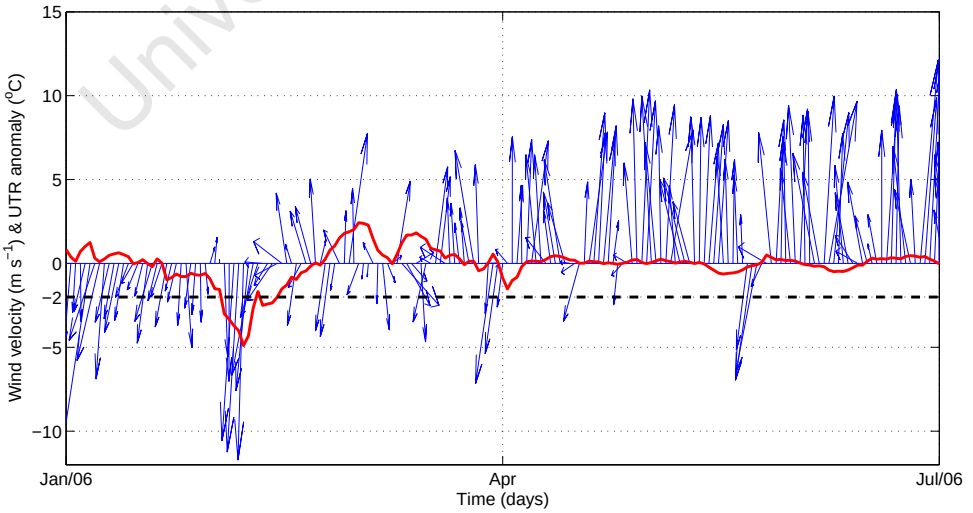

(c)

Figure 4.7: Parts of time series for daily UTR anomaly (^{o}C; wide red solid line) and blended wind velocity vectors (m s^{-1}) extracted at UTR site for the period (a) July−December 2003, (b) July−December 2004 and (c) January−June 2006. Horizontal dashed line corresponds with UTR anomaly of -2^oC. Black arrows show and alphabetical letters show example of relationship between magnitude of NE winds and cool events.

Spatial distribution of eddies (altimeter data)

Parts of the time series for merged sea level anomaly (cm, shading) and geostrophic velocity vectors (m s^{-1}, arrows) of global $1/3^o$ grid data product derived from multi-satellite altimeter mission (AVISO) at the study area are shown for the weekly delayed time between the period January 2003 to August 2007 (Figure 4.8a−f) and for daily near real time during the ASCLME cruse survey in December 2008 (Figure 4.8g) and in August 2009 (Figure 4.8h). Figures 4.8a and b correspond with an upwelling event between 15 August and 23 September 2004, apparent by enhanced Chl-*a* (Figure 3.4) and cool water (Figure 3.5) and also a NE wind regime (Figure 4.2d). There is strong eddy variability (in both space and time) within the domain. This variability is characterized by several anti-cyclonic and cyclonic eddies propagating southward.

On 18 August 2004 (Figure 4.8a) three cyclonic features are found at different latitudes. One cyclonic feature (unlikely to be a cyclonic eddy) is found to have low SLA of −10 cm along the Angoche coast between 15 and 17^oS, which is consistent with shelf upwelling. Two cyclonic eddies appear centred at 17^oS (slope site) and 19^oS, respectively. Weak anti-cyclonic features are observed adjacent to these cyclonic features, in particular, a relatively strong anti-cyclonic eddy is observed entering at the north of the Mozambique Channel.

On 8 September 2004, 6 April 2005 and 21 December 2005 (Figure 4.8b, d and f, respectively) a large anti-cyclonic feature was found across the entire narrow section of the Mozambique Channel (16−18^oS). The one on 6 April 2005 was relatively small and weak with low positive SLA of about 15 cm. Two cyclonic features were also observed, one to the north of the large anti-cyclone and the other to the south. On 8 September 2004 (Figure 4.8b) the cyclonic feature in the north was weak (~ -5 cm), possibly representing the early stage of a cyclonic eddy formation. The cyclone to the south on 6 April 2005 and 21 December 2005 was large and strong with depression of SLA of ∼30 cm.

On 5 January 2005 (4.8e) two cyclonic features were found off Angoche, one weak (almost zero cm) centred in the shelf at 15^oS and the other relatively strong ($\sim$ 12 cm) centred in the slope at 18^oS, which is found with depression of SLA of ∼30 cm. These two cyclonic features are separated with one anti-cyclonic feature found at 17^oS on the eastern side of the channel

(Madagascar coast, 4.8e). A (weak) anti-cyclonic feature was found to the north and another to the south. Figure 4.8e for 09 November 2005 shows a small, perfect, circular, strong anti-cyclonic eddy in the middle of the channel (17^oS) surrounded by three cyclonic features. Two other anti-cyclone features are found, one is observed entering to the north of the channel and the other is elongated across the channel to the south.

During the 2008 ASCLME cruise, on 05 December a large, strong($\sim$ 30 cm), anti-cyclonic eddy is found centred around 17^oS surrounded by three cyclonic features, one to the north-west, another to the south-west and the other south-east of the central large anti-cyclone (Figure 4.8g). The one to the south-east was large and strong ($\sim$ 30 cm). For the 2009 ASCLME cruise on 13 August, an anti-cyclonic eddy is found on the slope around $16^o30'S$ propagating southward and connecting with another anti-cyclonic feature to the south. A large cyclonic feature is observed entering the channel to the north. Another cyclonic feature is found leaving the channel to the south and another small cyclonic feature is found in the inshore on the west side adjacent to the two anti-cyclones.

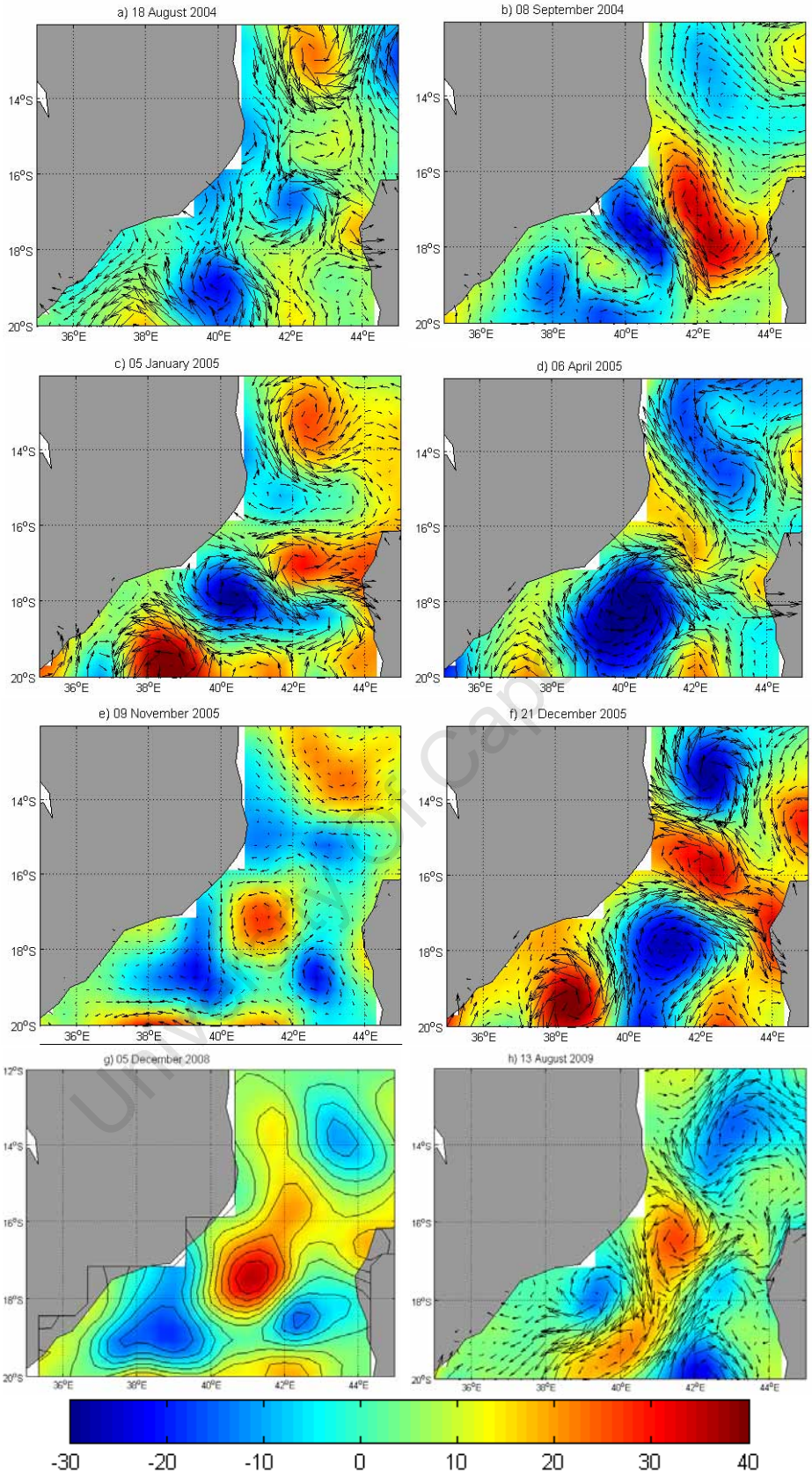

Figure 4.8: Examples of merged weekly sea surface anomaly (cm) and geostrophic velocity vectors (cm s^{-1}) derived from AVISO altimetry global $1/3^o$ grid data product on (a) 18 August 2004, (b) 08 September 2004, (c) 05 January 2005, (d) 06 April 2005 (e) 09 November 2005 and (f) 21 December 2005. Note a and b correspond with the upwelling (enhanced Chl-a Figure 3.4; cool water Figure 3.5; and NE wind Figure 4.2d) event from 15 August to 23 September 2004. (g) 05 December 2008 during the 2008 cruise and (h) 13 August 2009 during 2009 cruise.

Time series of altimetry data

In order to better understand the likely impact of passing eddies on the coastal ocean dynamics, the SLA is presented as a time series for the three specific locations selected in figure 4.1. The time series for SLA (cm) from January 2003 to August 2007 is shown in figure 4.9. The alphabetical letters refers to snapshots of the SLA field depicted in Figure 4.8. The alphabetical letters show that positive SLAs indicate anti-cyclonic features (b, d and f on Figure 4.9a−b; and also b, c and e on Figure 4.9c) and negative SLAs indicate cyclonic features (a, c and e in Figure 4.9a−b; and also a, d and f on Figure 4.9c). Figure 4.9 shows strong variability at intraseasonal periods throughout the time series. Eddies passed through all three selected areas irregularly and no seasonal signal was found. Five to eight eddies (events) were observed per year, which gives a period of about 52 to 73 days per event.

In the UTR and slope sites three time periods were remarkable: (1) January 2003 to July 2005, during which anti-cyclonic (positive SLA) features are dominant and only a few cyclonic (negative SLA) features were found. (2) August 2005 and December 2007 had variability characterized by a sequence of anti-cyclonic and cyclonic features (positive peak to negative peak fluctuations, Figure 4.9a and c). At the slope site this regime started early (October 2004, Figure 4.9c). (3) January to August 2007 was characterized by dominance of anti-cyclonic features. In the shelf site the whole time series was characterized by dominance of anti-cyclonic features and a few ($\sim$4) cyclonic features (Figure 4.9b).

The magnitude of the variability was generally low in all three areas. The maximum anti-cyclonic feature ($\sim$ 30 cm) was observed at the slope site in January 2004 (Figure 4.9c). The maximum cyclonic features ($\sim$-20 cm) were observed at the shelf site in August 2005 (Figure 4.9b) and at the slope site in September 2004 and December 2006 (Figure 4.9c). The UTR site (Figure 4.9a) had very low magnitudes of SLA, ranging from -10 to 20 cm and with no large ($>$ -10 cm) cyclonic features observed.

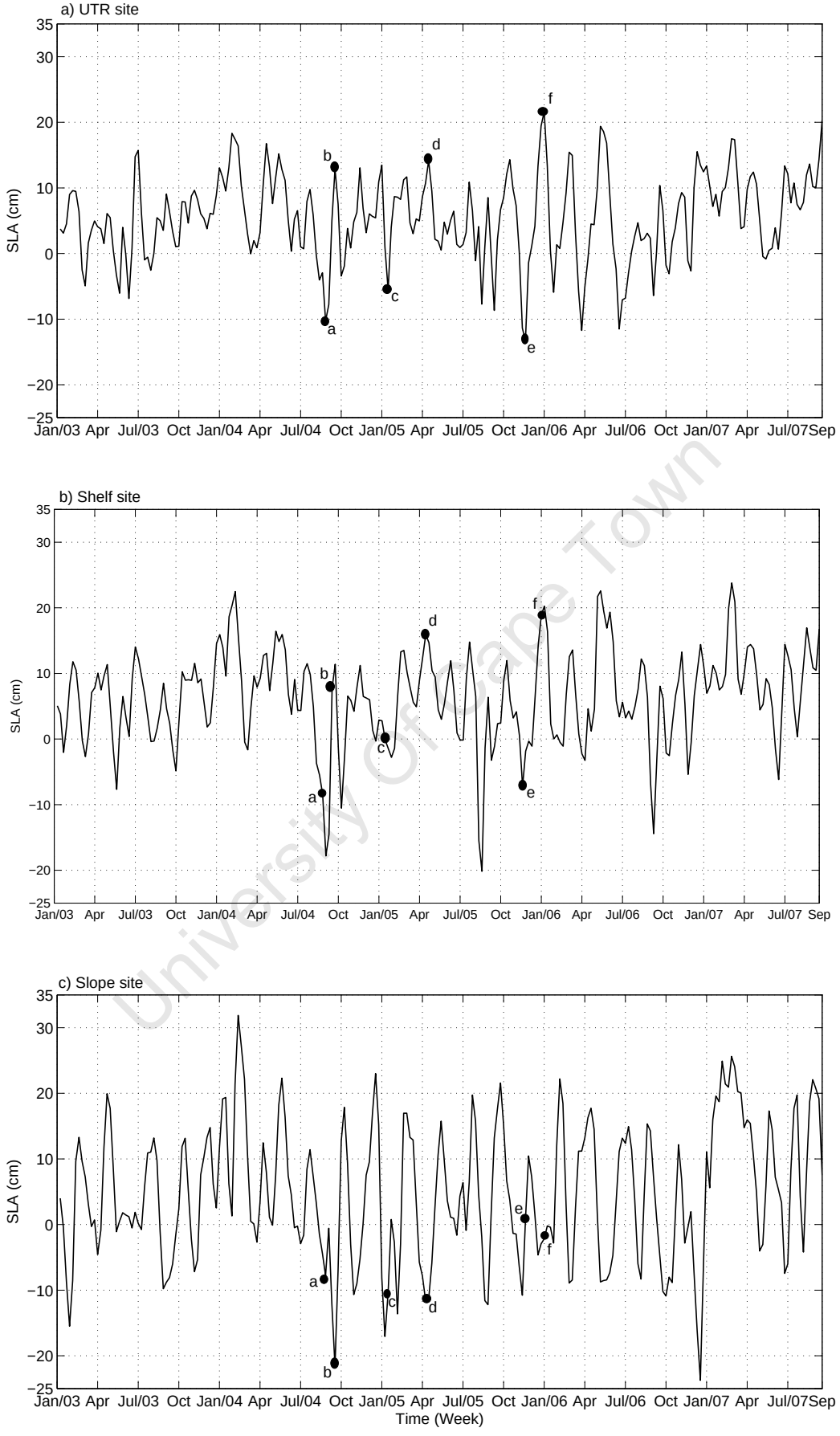

Figure 4.9: Time series of SLA (cm) derived from AVISO altimetry global $1/3^o$ grid data product over (a) the UTR site, (b) the shelf and (c) the slope site for the period January 2003 to August 2007. Alphabetical letters refer to the SLA maps depicted in Figure 4.8.

Comparison of time series for SLA and UTR

The time series of daily UTR anomaly (18 m depth) for the period January 2003 to September 2007 was compared to time series of weekly merged sea surface anomalies derived from multi-satellite altimetry (AVISO) at the UTR site. Figure 4.10 and 4.11 show parts of these comparisons. No relationship between cool water events ($> 2^oC$ change) and eddy variability was found. Cool water events were observed in all phases of the eddy variability: associated with anti-cyclonic eddies, for example, in January 2003, in October to December 2003, and in February 2006, associated with cyclonic eddies (in middle February 2003), during the passage of anti-cyclonic eddies (March 2006), and during the passage of cyclonic eddies (late August 2004). Some cool events were observed associated with very weak (< 5 cm) SLAs.

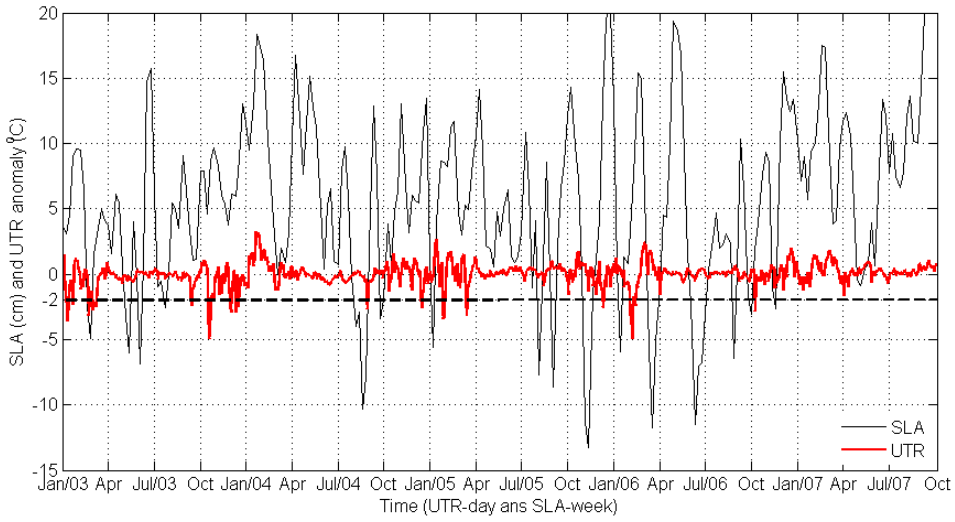

(a)

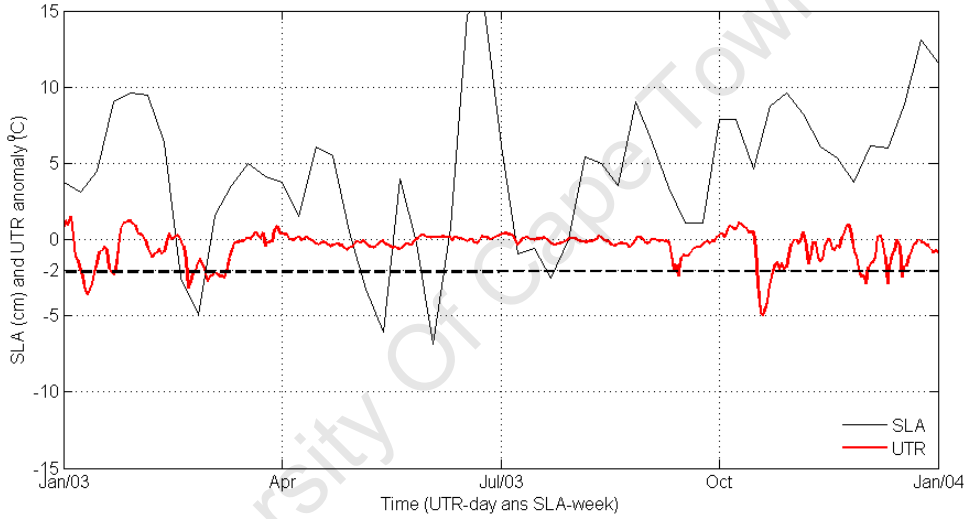

(b)

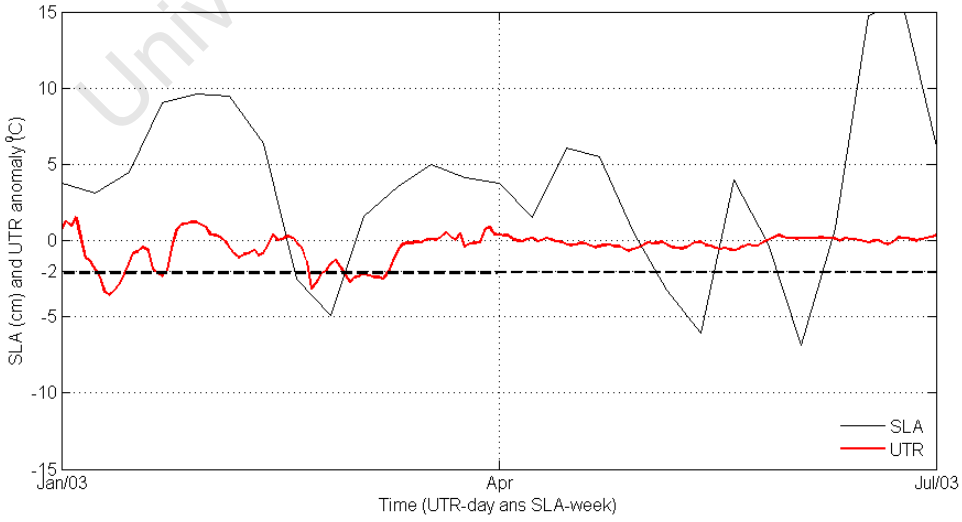

(c)

Figure 4.10: Time series for daily UTR anomaly (^{o}C; wide red solid line) measured at 18 m depth and weekly merged SLA (cm s^{-1}, black line) extracted at the UTR site for the period (a) of whole time series January 2003−September 2007, (b) year 2003 and (c) January−June 2003. Horizontal dashed line corresponds with UTR anomaly of -2^oC.

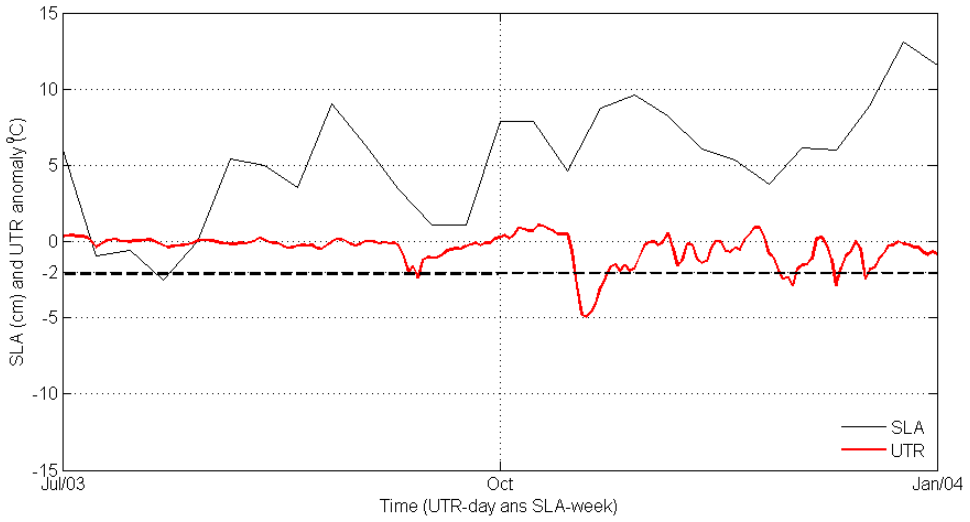

(a)

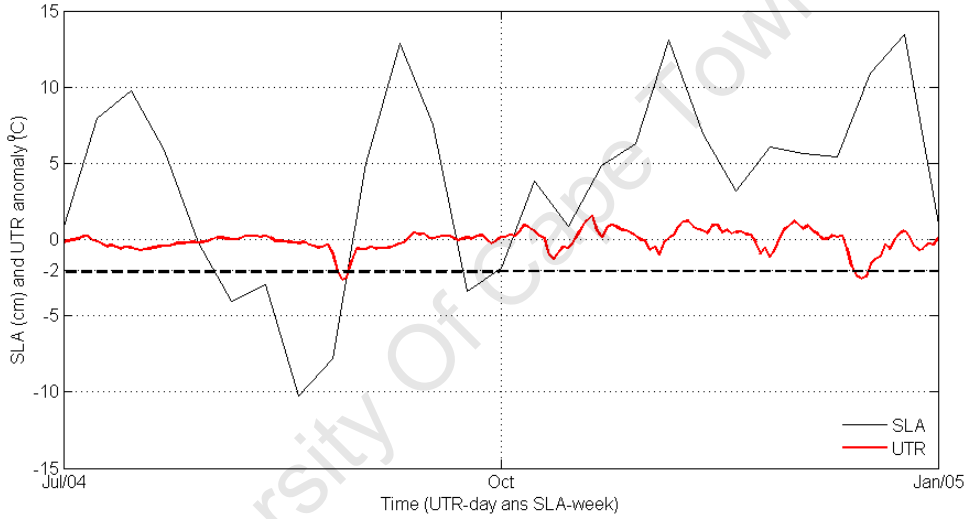

(b)

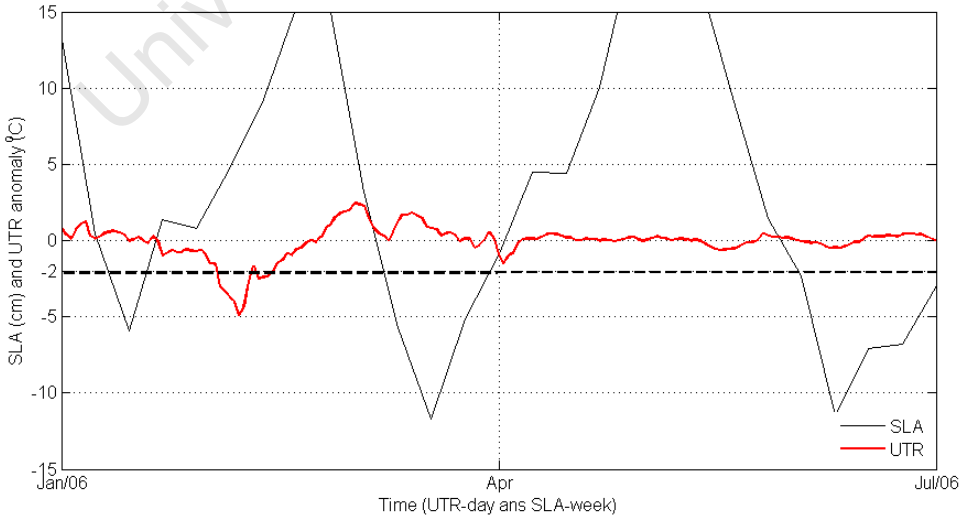

(c)

Figure 4.11: Parts of time series for daily UTR anomaly (^{o}C; wide red solid line) and weekly merged SLA (cm s^{-1}, black line) extracted at UTR site for the period (a) July−December 2003, (b) July−December 2004 and (c) January−June 2006. Horizontal dashed line corresponds with UTR anomaly of -2^oC.

4.4 Discussion

Wind-driven upwelling

The blended sea surface wind (10 m) data derived from multi-satellite observations reveal two distinct wind regimes (Figure 4.2-4.5). One is the south-westerly (SW) wind regime between April−July (austral autumn−winter). The other is the north-easterly (NE) wind regime between August−March (austral spring−summer). These two wind regimes correspond to the southern extension of the East African monsoon, which was also noted by Sætre and da Silva (1982). These monsoon seasons were consistent at all three selected sites with SW winds being stronger and more persistent than the NE wind (Figure 4.3-4.5). To the south of 18^{o}S, the influence of south-east (SE) trade winds is apparent, suggesting that this latitude is the southern limit of the East African monsoon system. This finding is not in agreement with that of Sætre and da Silva (1982) who suggested that monsoon winds do not reach 16^{o}S. However their study was based on two meteorological stations located along the coast (one in Pemba and other in Quelimane near Nicoadala, Figure 2.1) with limited spatial coverage. The present study, in contrasty used 0.25^o grid resolution data, giving greater spatial coverage and resolving the wind field reasonably well.

A good degree of correspondence between upwelling and sea surface wind (monsoon) seasons is apparent in the whole time series (Figure 4.6 and 4.7). Cool water (i.e. upwelling) events appear to be mostly connected to the low-velocity, alongshore NE monsoon wind between August−March (austral spring−summer). In contrast, the long period, without cool water (i.e. downwelling), events appear to be associated with high-velocity, SW monsoon winds between April−July. These facts strongly suggest that NE monsoon weak-winds are the favourable wind conditions for the upwelling near Angoche, and that the SW monsoon strong-winds favour downwelling. SW winds during the NE monsoon season (August−March) cause relaxation of upwelling (leading to numerous upwelling events in the intraseasonal period). Monsoon-driven upwelling, particularly in summer has been observed in other parts of the world ocean by Udarbe-Walker and Villanoy (2001) in the western Philippines Sea, by Liu et al. (2002) in the South China Sea, by Habeebrehman et al. (2008) in the India-Arabian Sea and by Hong et al.

(2009) in the Taiwan Strait.

Although clear evidence of wind-driven upwelling is apparent, the strength of the wind and the amplitude of upwelling events does not match well. This implies that there are other forces (factors) contributing to the shelf edge upwelling in northern Mozambique, i.e., wind alone cannot bring deep (>300 m), cold, water to the surface.

Meandering current-driven upwelling

Multi-satellite altimeter data (2003−2007) showed strong eddy variability near Angoche (Figure 4.8 and 4.9). This is consistent with previous studies by Ridderinkhof and de Ruijter (2003); Lutjeharms (2006); Backeberg et al. (2009); Backeberg and Reason (2010) and de Ruijter et al. (2002). In this dissertation upwelling is shown to be associated with both anti-cyclonic and/or cyclonic eddies.

A comparison of the weekly sea surface anomaly (SLA) and daily water temperature at a depth of 18 m showed no direct correlation between upwelling and the presence of eddies (Figure 4.10 and 4.11). Eddies therefore contribute little to the occurrence of upwelling off northern Mozambique (i.e. the role of eddies is limited compared to the role of wind induced upwelling). Omta et al. (2009) also found that temporal variability of Chl-a in the Mozambique Channel was not necessarily associated with eddies. Moreover, there is no apparent seasonal variation in the SLA time series (Figure 4.9), thus observed upwelling events with a seasonal cycle are unlikely to be induced by eddies without a seasonal cycle.

This first analysis suggests that the role of eddies in driving upwelling is non existent. However, this statement requires a more detailed study to confirm this. One potential problem in this present study is that altimeter data are not reliable very close to the coast (source AVISO wed site `http://www.aviso.oceanobs.com`, last visited March 2010) and hence could explain the lack of correlation with the UTR data.

Chapter 5

Summary and conclusion

For the first time, the upwelling cell suggested by Nehring et al. (1987) has been studied for its spatial-temporal variability and associated driving mechanism. The present study confirmed that upwelling, apparent by cool water and enhanced Chl-a, occurs on the northern Mozambique coast near Angoche. However, the results revealed that upwelling is not strongly manifested at the surface. This finding, together with the fact that the region is strongly influenced by cloud cover implies that satellite observations, particularly those for ocean colour, are not useful on their own for detecting upwelling in the Mozambique Channel.

The results showed that shelf edge upwelling in northern Mozambique (near Angoche) is found between $15-18^{o}$S and the coast-41^{o}E. It covers a total area of approximated 68 000 km^2, with a north-south extent of $\sim$437 km and a west-east extent of $\sim$412 km. Two upwelling core regions were identified within this area: (1) the shelf core region and (2) the slope core region. Upwelling observed at the shelf core region was more persistent than that at the slope core region. Most upwelling events begin at the shelf core region and propagate southwards.

Shelf edge upwelling off the northern Mozambique coast has a strong seasonality. The downwelling season, a period characterized by absence of upwelling, occurs between April$-$July. The upwelling season occurs between August$-$March (austral spring$-$summer) every year. The upwelling season is characterized by numerous cool water events of varying duration (8$-$65 days). The dominant period for the upwelling events was 2 months.

Shelf edge upwelling in northern Mozambique is in part a wind-driven in response to seasonal north-easterly monsoon weak-velocity winds (austral spring−summer). Upwelling favourable wind results in decreases in the temperature at a depth of 18 m by more than 4^{o}C, which is larger than the amplitude of the observed seasonal variation.

Shelf edge upwelling off northern Mozambique is apparent as an intermittent feature in intraseasonal (8−65 days) periods during the NE monsoon season (August−March). The intermittent behavior of upwelling (cool water) events is in part due to fluctuations in the wind direction during the NE monsoon winds.

Although it has been found that wind (NE monsoon) plays an important role in upwelling, it must be acknowledged that other remote forcing may be involved in to raising the thermocline next to the shelf so that deep water is readily available to the favourable wind to induce upwelling at the surface. A good correlation between upwelling (cool water events) and the presence of eddies (SLA data) was not apparent in this study. This implies that eddies do play a limited role in driving coastal upwelling in northern Mozambique. Further investigation concerning the role of eddies is required. Further investigation is also necessary in order to clarify the role of other possible forcing factors.

It should be mentioned that a strong upwelling event was evident in early October 2006, particularly at the shelf and slope site as evidenced by anomalously high Chl-a values, but this was not coincident with a cool water event. Such an event coincided with a minimum peak of SST seasonal variation (late winter) and this may be the reason why the cooling was not visible. There was no obvious wind event or eddy structure that could account for these high Chl-a values.

Mozambique is located at the western boundary of the Indian Ocean and is thus not favourably situated for the occurrence of conventional poleward wind-driven upwelling (e.g. common in many eastern ocean boundary areas). The upwelling near Angoche seems to be unique in the northern region of Mozambique. Thus, the importance of the upwelling cannot be underestimated. The area around Angoche seems to be the most productive on the Mozambique coast (Nehring et al. 1987) and has great value for shallow water shrimps (family PENAEIDAE),

the main component of Mozambique's export fisheries ($\sim$ 4034 tons and amounts to 40 million USD per year).

References

Anderson, T. R. and Lucas, M. I. (2008). *Upwelling Ecosystems*, volume 5 of Encyclopedia of Ecology, pages 3651–3661. Elsevier, Oxford.

AVISO/Altimetry (1996). AVISO user handbook for Merged TOPEX/POSEIDON products. *AVI-NT-02-101*, Edition 3:200pp.

AVISO/Altimetry (2005). DT CorSSH and DT SLA product handbook. *CLS-DOS-NT*, 05-097(V1 rev 1):24pp.

AVISO/Altimetry (2009). SSALTO/DUACS user handbook: (M)SLA and (M)ADT Near-Real time and delayed time product. *CLS-DOS-NT*, 06.034(1 rev 10):47pp.

Backeberg, B. C., Bertino, L., and Johannessen, J. A. (2009). Evaluating two numerical advection schemes in HYCOM for eddy-resolving modelling of the Agulhas Current. *Ocean Science*, 5(2):173–190.

Backeberg, B. C., Johannessen, J. A., Bertino, L., and Reason, C. J. C. (2008). The greater Agulhas Current system: An integrated study of its mesoscale variability. *Journal of Operational Oceanography*, 1(1):29–44.

Backeberg, B. C. and Reason, C. J. C. (2010). A connection between the South Equatorial Current north of Madagscar and Mozambique Channel Eddies. *Geophysical Research Letters*, 37:1–6.

Berger, W. H. and Wefer, G. (2002). On the reconstruction of upwelling history: Namibia upwelling in context. *Marine Geology*, 180:3–28.

Biastoch, A. and Krauss, W. (1999). The role of mesoscale eddies in the source regions of the Agulhas Current. *Journal of Physical Oceanography*, 29:2303–2317.

Campos, E. J. D., Velhote, D., and da Silveira, I. C. A. (2000). Shelf break upwelling driven by Brazil Current cyclonic meanders. *Geophysical Research Letters*, 27(6):751–754.

de Ruijter, W. P. M., Ridderinkhof, H., Lutjeharms, J. R. E., Schouten, M. W., and Veth, C. (2002). Observations of the flow in the Mozambique Channel. *Geophysical Research Letters*, 29(10):1502–1504.

de Sousa, L. P., Brito, A., Abdula, S., Penn, J., and Howell, D. (2008). O Camarao do Banco de Sofala 2008. Technical report, Instituto Nacional de Investigacao Pesqueira, Maputo.

Duxbury, A. C. and Duxbury, A. B. (1997). *An introduction to the World's Ocean*. Boston: McGraw-Hill., fifth edition.

Emery, W. J. and Thomson, R. E. (2001). *Data analysis methods in physical oceanography*. Elsevier, Amsterdam, 2nd rev edition.

Gill, A. E. (1982). *Atmospheric-Ocean Dynamics*, page 662 pp. Academic Press.

Gill, A. E. and Schumann, E. H. (1979). Topographically induced changes in the structure of an inertial coastal jet. *Journal of Physical Oceanography*, 9:975–991.

Habeebrehman, H., Prabhakaran, M. P., Jacob, B., Sabu, J., Jayalakshmi, K. J., Achuthankutty, C. T., and Revichandran, C. (2008). Variability in biological responses influenced by upwelling events in the Eastern Arabian Sea. *Journal of Marine Systems*, 74:545–560.

Halo, I. F. M. (2008). The influence of ocean ridges on the circilation to the south of Mozambique Channel and Madagascar. Master's thesis, Department of oceanography - University of Cape Town, South Africa.

Ho, C. R., Zheng, Q., and Kuo, N. J. (2004). SeaWiFs observations of upwelling south of Madagascar: long-term variability and interaction with East Madagascar Current. *Deep-Sea Research II*, 51:59–67.

Hong, H., Zhang, C., Shang, S., Huang, B., Li, X., Li, Y., and Zhang, S. (2009). Interannual variability of summer coastal upwelling in the Taiwan Strait. *Continental Shelf Research*, 29:479–484.

Johnesen, E., Krakstad, J. O., Ostrowski, M., Serigstad, B., Stromme, T., Alvheim, O., Olsen, M., Zaera, D., Andre, E. R., Dias, N., de Sousa, L., de Sousa, B., Malauene, B. S., and Abdula, S. (2008). Survey of the living marine resources of Mozambique. Ecosystem survey and special studies. Cruise reports "Dr. Fridtjof Nansen". Technical Report FAO-NORAD PROJECTNO: GCP/INT/003/NOR, Institute of Marine Research (IMR), Bergen.

Liu, K. K., Chao, S. Y., Shaw, P. T., Gong, G. C., Chen, C. C., and Tang, T. Y. (2002). Monsoon-forced chlorophyll distribution and primary production in the South China Sea: observations and numerical study. *Deep-Sea Research I*, 49:1387–1412.

Lund-Hansen, L. C. and Vang, T. (2003). Development of a coastal upwelling front driven by advection and topographic effects in the North Sea-Baltic Sea transition. *Oceanologica Acta*, 26:577–584.

Lutjeharms, J. R. E. (2006). *The Agulhas Current*. Springer-Praxis Books.

Lutjeharms, J. R. E. and da Silva, A. J. (1988). The Delagoa bight eddy. *Deep-Sea Research I*, 35(4):619–634.

Lutjeharms, J. R. E. and Machu, E. (2000). An upwelling cell inshore of the East Madagascar Current. *Deep-Sea Research I*, 47:2405–2411.

McCreary, J. P., Kundu, P., and Chao, S. (1987). On the dynamic of the California Current system. *Journal of Marine Research*, 45:1–32.

Nehama, F. P. J. (2008). Dynamics of the Zambezi River Plume. Master's thesis, School of Ocean Sciences, Bangor University, United Kingdom.

Nehring, D., Hagen, E., da Silva, J. A., Schemainda, R., Wolf, G., Michelchen, N., Kaiser, W., Postel, L., Gosselck, F., Brenning, U., Kuhner, E., Arlt, G., Siegel, H., Gohs, L., and Bublitz, G. (1987). Results of oceanological stuies in the Mozambique Channel in February-March 1980. *Beitrage Zur Meereskunded*, 56:51–63.

Oliveira, P. B., Nolasco, R., Dubert, J., Miota, T., and Peliz, A. (2009). Surface temperature, chlorophyll and advection patterns during a summer upwelling event off central Portugal. *Continental Shelf Research*, 29:759–774.

Omta, A. W., Llido, J., Garc-on, V., Kooijman, S. A. L. M., and Dijkstra, H. A. (2009). The interpretation of satellite chlorophyll observations: the case of the Mozambique Channel. *Deep-Sea Research I*, 56:974–988.

Palma, E. D. and Matano, R. P. (2009). Disentangling the upwelling mechanisms of the south Brazil Bight. *Continental Shelf Research*, 29:1525–1534.

Patti, B., Guisande, C., Vergara, A. R., Riveiro, I., Maneiro, I., Barreiro, A., Buscaino, G., Cuttitta, A., Basilone, G., and Mazzola, S. (2008). Factors responsible for the differences in satellite-based chlorophyll-a concentration between the major global upwelling areas. *Estuarine, Coastal and Shelf Science*, 76:775–786.

Pickard, G. L. and Emery, W. J. (1990). *Descriptive physical oceanography an introduction*. Pergamon press, Oxford, 5th edition.

Quartly, G. D. and Srokosz, M. A. (2004). Eddies in the southern Mozambique Channel. *Deep-Sea Research II*, 51(1-3):69–83.

Ridderinkhof, H. and de Ruijter, W. P. M. (2003). Moored current observations in the Mozambique Channel. *Deep-Sea Research II*, 50:1933–1955.

Roughan, M. and Middleton, J. H. (2002). A comparison of observed upwelling mechanisms off the east coast of Australia. *Continental Shelf Research*, 22:2551–2572.

Sætre, R. and da Silva, A. J. (1982). Water mass and circulation of the Mozambique Channel. Revista de investigacao pesqueira. Technical Report 3, Instituto de Desenvolvimanto Pesqueiro, Maputo.

Sætre, R. and da Silva, A. J. (1984). The circulation of the Mozambique Channel. *Deep-Sea Research I*, 31:485–508.

Sarhan, T., Lafuente, J. G., Vargas, M. J., and PLaza, F. (2000). Upwelling mechanisms in the northwestern Alboran Sea. *Journal of Marine Systems*, 23:317–331.

Schemainda, R. and Hagen, E. (1983). On the steady state intermediate vertical current induced by the Mozambique Current. *Oceanography Topography*, 18:18–88.

Schouten, M. W., de Ruijter, W. P. M., and van Leeuwen, P. J. (2002). Upstream control of Agulhas Ring shedding. *Journal of Geophysical Research*, 107(C8):3109–3120.

Schouten, M. W., de Ruijter, W. P. M., van Leeuwen, P. J., and Ridderinkhof, H. (2003). Eddies and variability in the Mozambique Channel. *Deep-Sea Research II*, 50:1987–2003.

Song, Y. T. and Chao, Y. (2004). A theoretical study of topographic effects on coastal upwelling and cross-shore exchange. *Ocean Modelling*, (6):151–176.

Tew-Kai, E. and Marsac, F. (2009). Patterns of variability of sea surface chlorophyll in Mozambique Channel: A quantitative approach. *Journal of Marine Systems*, (77):77–88.

Thompson, K. R. and Demirov, E. (2006). Skewness of sea level variability of the world's oceans. *Journal of Geophysical Research*, 111(C05005).

Tomczak, M. and Godfrey, J. S. (1994). *Regional oceanography: an introduction*. Elsevier, New York, first edition.

Torrence, C. and Compo, G. P. (1998). A practical guide to wavelet analysis. *Bulletin of the American Meteorological Society*, 79:61–78.

Trauth, M. H. (2006). *Matlab recipes for earth science*. Springer-Verslag, Berlin.

Udarbe-Walker, M. J. B. and Villanoy, C. L. (2001). Structure of potantial upwelling areas in the Philippines. *Deep-Sea Research I*, 48:1499–1518.

Weimerskirch, H., Le Corre, M., Jaquemet, S., Potier, M., and Marsac, F. (2004). Foraging strategy of a top predator in tropical water: great frigatebirds in the Mozambique Channel. *Marine Ecology Progress Series*, 275:297–308.

Zhang, H. M., Bates, J. J., and Reynolds, R. W. (2006a). Assessment of composite global sampling: Sea surface wind speed. *Geophysical Research Letters*, 33(L17714):1–5.

Zhang, H. M., Reynolds, R. W., and Bates, J. J. (2006b). Blended and gridded high resolution global sea surface wind speed and climatology from multiple satellite: 1987 - present. *American Meteorologicall Society*, Annual meeting:p2.23.